2018

Flow Behavior And Instabilities In Viscoelastic Fluids: Physical And Biological Systems

Boyang Qin
University of Pennsylvania, kokaqin@gmail.com

Recommended Citation

Qin, Boyang, "Flow Behavior And Instabilities In Viscoelastic Fluids: Physical And Biological Systems" (2018). *Publicly Accessible Penn Dissertations*. 3174.
https://repository.upenn.edu/edissertations/3174

Flow Behavior And Instabilities In Viscoelastic Fluids: Physical And Biological Systems

Abstract

The flow of complex fluids, especially those containing polymers, is ubiquitous in nature and industry. From blood, plastic melts, to airway mucus, the presence of microstructures such as particles, proteins, and polymers, can impart nonlinear material properties not found in simple fluids like water. These rheological behaviors, in particular viscoelasticity, can give rise to flow anomalies found in industrial settings and intriguing transport dynamics in biological systems.

The first part of my work focuses on the flow of viscoelastic fluids in physical systems. Here, I investigate the flow instabilities of viscoelastic fluids in three different geometries and configurations. Realized in microfluidic channels, these experiments mimic flows encountered in technology spanning the oil extraction, pharmaceutical, and chemical industries. In particular, by conducting high-speed velocimetry on the flow of polymeric fluid in a micro-channel, we report evidence of elastic turbulence in a parallel shear flow where the streamline is without curvature. These turbulent-like characteristics include activation of the flow at many time scales, anomalous increase in flow resistance, and enhanced mixing associated with the polymeric flow. Moreover, the spectral characteristics and spatial structures of the velocity fluctuations are different from that in a curved geometry. Measured using novel holographic particle tracking, Lagrangian trajectories show spanwise dispersion and modulations, akin to the traveling waves in the turbulent pipe flow of Newtonian fluids. These curvature perturbations far downstream can generate sufficient hoop stresses to sustain the flow instabilities in the parallel shear flow.

The second part of the thesis focuses on the motility and transport of active swimmers in viscoelastic fluids that are relevant to biological systems and human health. In particular, by analyzing the swimming of the bi-flagellated green algae {\it Chlamydomonas reinhardtii} in viscoelastic fluid, we show that fluid elasticity enhances the flagellar beating frequency and the wave speed. Yet the net swimming speed of the alga is hindered for fluids that are sufficiently elastic. The origin of this complex response lies in the non-trivial change in flagellar gait due to elasticity. Numerical simulations show that such change in gait reduces elastic stress build up in the fluid and increases efficiency. These results further illustrate the complex coupling between fluid rheology and swimming gait in the motility of micro-organisms and other biological processes such as mucociliary clearance in mammalian airways.

Degree Type

Dissertation

Degree Name

Doctor of Philosophy (PhD)

Graduate Group

Mechanical Engineering & Applied Mechanics

First Advisor

Arratia E. Paulo

Keywords
Complex fluids, Flow instability, Low Re Swimming, Polymer fluid, Rheology, Viscoelasticity

Subject Categories
Mechanical Engineering

FLOW BEHAVIOR AND INSTABILITIES IN VISCOELASTIC FLUIDS: PHYSICAL AND BIOLOGICAL SYSTEMS

Boyang Qin

A DISSERTATION

in

Mechanical Engineering and Applied Mechanics

Presented to the Faculties of the University of Pennsylvania

in

Partial Fulfillment of the Requirements for the

Degree of Doctor of Philosophy

2018

Supervisor of Dissertation

Paulo E. Arratia, Professor, Mechanical Engineering and Applied Mechanics

Graduate Group Chairperson

Kevin T. Turner, Professor, Mechanical Engineering and Applied Mechanics

Dissertation Committee

Paulo E. Arratia, Professor, Mechanical Engineering and Applied Mechanics

Howard H. Hu, Professor, Mechanical Engineering and Applied Mechanics

Douglas J. Jerolmack, Associate Professor, Earth and Environmental Science

Steven D. Hudson, Physical Scientist, Materials Science and Engineering Division,
National Institute of Standards and Technology

Flow behavior and instabilities in viscoelastic fluids: physical and biological systems

ACKNOWLEDGEMENT

I am truly grateful to many individuals whose support, encouragement, and wisdom have made the completion of this dissertation possible. I am deeply indebted to my advisor, Professor Paulo E. Arratia, for being an incredible mentor, for his passion and curiosity in research, and for showing me the importance of resilience in science. I'd like to also thank the entire faculty, students, and staff of the department of Mechanical Engineering and Applied Mechanics, particularly Professor Prashant Purohit for his wonderful lectures and generous advices, Peter Szczesniak for his help with many hours of parts machining, and Eric Johnston for his assistance and training on cleanroom micro-fabrication.

My special acknowledgement extends to all the former and current group members for their supportive discussions and collaborative spirit. In particular, I'd like to thank Dr. Arvind Gopinath, Dr. Alison E. Koser, and Dr. David A. Gagnon for the many intellectual and philosophical discussions, many of which I deeply enjoyed. They and many other friends here at Penn have made my time as a doctoral student so much more rewarding, colorful, and endearing.

I'd like to thank Dr. Paul Salipante and Dr. Steven Hudson for their generous help with holographic particle tracking techniques and the many insightful discussions on the flow of complex fluids. I'd like to also thank my collaborators Dr. Chuanbin Li, Dr. Becca Thomases, and Dr. Robert Guy for the many wonderful discussions, both face-to-face and remotely, on the study of flagellar kinematics in viscoelastic fluid. My work is generously supported by NSF-CBET-1336171 and NSF-DMR-1104705.

Finally, I believe a fraction of my every minute of existence is connected to and shared with my parents. I cannot thank them enough for the lifetime of love, support, and guidance they generously offered me that continue to inspire and shape who I am today.

ABSTRACT

FLOW BEHAVIOR AND INSTABILITIES IN VISCOELASTIC FLUIDS: PHYSICAL AND BIOLOGICAL SYSTEMS

Boyang Qin

Paulo E. Arratia

The flow of complex fluids, especially those containing polymers, is ubiquitous in nature and industry. From blood, plastic melts, to airway mucus, the presence of microstructures such as particles, proteins, and polymers, can impart nonlinear material properties not found in simple fluids like water. These rheological behaviors, in particular viscoelasticity, can give rise to flow anomalies found in industrial settings and intriguing transport dynamics in biological systems.

The first part of my work focuses on the flow of viscoelastic fluids in physical systems. Here, I investigate the flow instabilities of viscoelastic fluids in three different geometries and configurations. Realized in microfluidic channels, these experiments mimic flows encountered in technology spanning the oil extraction, pharmaceutical, and chemical industries. In particular, by conducting high-speed velocimetry on the flow of polymeric fluid in a micro-channel, we report evidence of elastic turbulence in a parallel shear flow where the streamline is without curvature. These turbulent-like characteristics include activation of the flow at many time scales, anomalous increase in flow resistance, and enhanced mixing associated with the polymeric flow. Moreover, the spectral characteristics and spatial structures of the velocity fluctuations are different from that in a curved geometry. Measured using novel holographic particle tracking, Lagrangian trajectories show spanwise dispersion and modulations, akin to the traveling waves in the turbulent pipe flow of Newtonian fluids. These curvature perturbations far downstream can generate sufficient hoop stresses to sustain the flow instabilities in the parallel shear flow.

The second part of the thesis focuses on the motility and transport of active swimmers in viscoelastic fluids that are relevant to biological systems and human health. In particular, by analyzing the swimming of the bi-flagellated green algae *Chlamydomonas reinhardtii* in viscoelastic fluid, we show that fluid elasticity enhances the flagellar beating frequency and the wave speed. Yet the net swimming speed of the alga is hindered for fluids that are sufficiently elastic. The origin of this complex response lies in the non-trivial change in flagellar gait due to elasticity. Numerical simulations show that such change in gait reduces elastic stress build up in the fluid and increases efficiency. These results further illustrate the complex coupling between fluid rheology and swimming gait in the motility of micro-organisms and other biological processes such as mucociliary clearance in mammalian airways.

TABLE OF CONTENTS

LIST OF ILLUSTRATIONS

CHAPTER 1 : Introduction

1.1. Motivation

Complex fluids are a broad class of material that are homogeneous at the macroscopic scale, disordered at the microscopic scale, yet structured at the intermediate mesoscale. The presence of these microstructures, such as particles, proteins and polymers in an otherwise simple fluid, is the norm rather than exception in nature, industry, and everyday life. Examples include milk, chocolate, cosmetics, paints, polymeric solutions, plastic melts, biofilms, blood, and mucus. An absolutely beautiful illustration of the rich complexity of this class of material is provided by McKinley [1] and reproduced in Fig. 1.1.

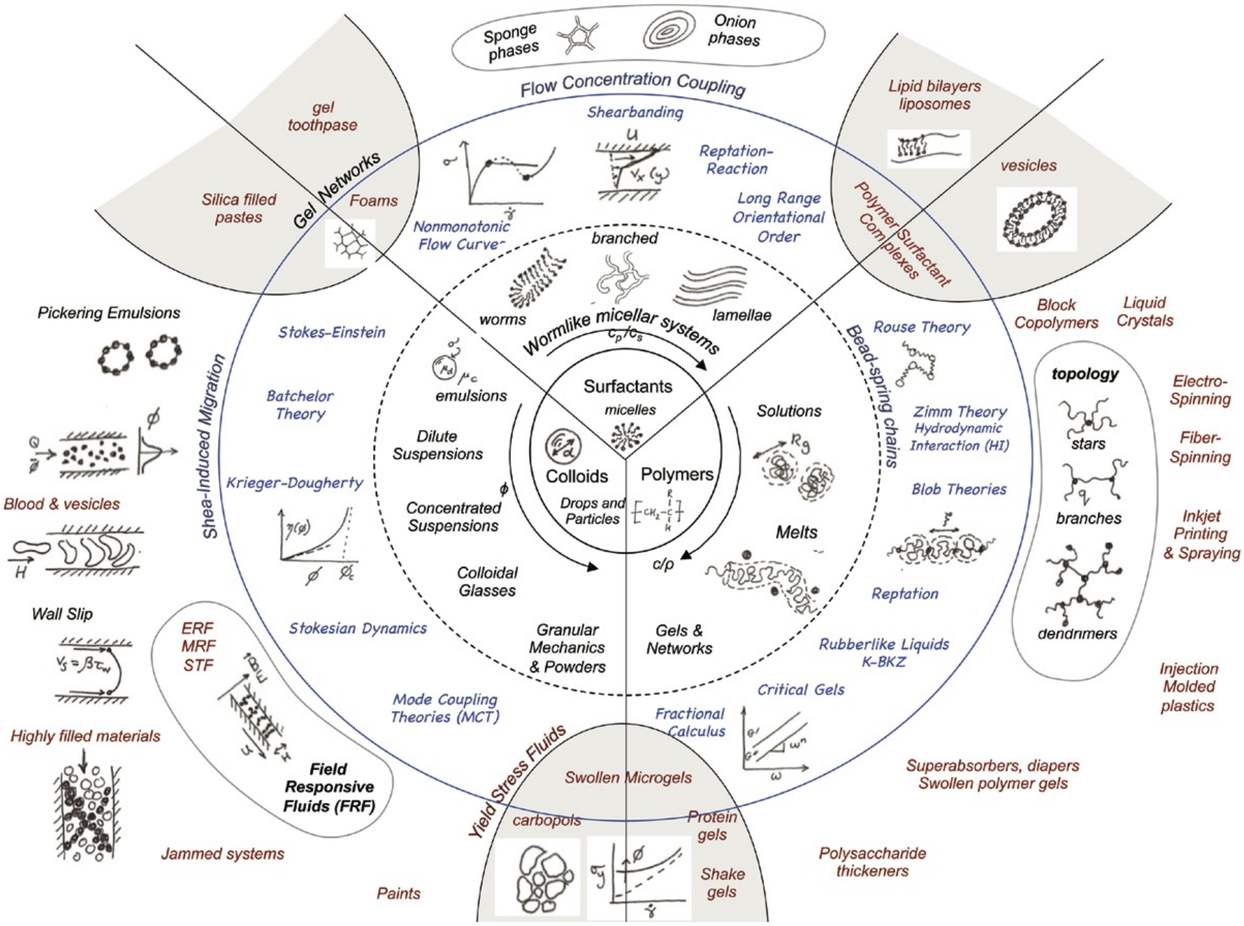

Figure 1.1: The hitchhiker guide to the universe of complex fluids by Gareth McKinley [1]. The subclass of polymeric fluids resides in the lower right sector.

More importantly, the structural organization and temporal dynamics at the intermediate scale strongly determine the macroscopic rheology and bulk flow behavior. In particular, fluids that contain long-chain flexible polymers, which can align with the flow, stretch under flow gradients, and relax in time, can possess a highly nonlinear rheological behavior called viscoelasticity. Depending on the time scale of the external flow, the material can behave either solid-like or liquid-like; depending on the velocity gradients of the flow, there can be an elastic stress in addition to the usual viscous stress. This link between material structure and aggregate behavior can have profound impact on how engineers operate these fluids in technology settings, such as 3-D printing, oil extraction and fiber extrusion. On the other hand, it critically affects how micro-organisms and organelles operate within these fluids in biological settings, such as the spreading of bacteria in the human gut and the mucociliary clearance in airways.

In this work, I will focus on two aspects of fluid elasticity that are relevant to industrial applications and human health. First I investigate the flow instabilities and anomalous transport associated with the nonlinear polymeric stresses that are both history-dependent and anisotropic. Three types of flow geometries and configurations are studied under high shear and strong extension flow conditions. In particular, I focus on the sequence of flow transitions, irregular flow structures, spectral characteristics, and the dynamical consequence on flow resistance. The flow conditions studied here are particularly relevant in industrial processes such as 3-D prototyping, oil extraction in shale layers, melt extrusions, and microfluidic mixing.

Second, I investigate the effect of fluid elasticity on the locomotion and transport of active swimmers. In particular, I focus on the swimming of the bi-flagellated alga *Chlamydomonas reinhardtii* in a viscoelastic fluid. The flagella of this green alga share the same "9+2" microtubule structure as respiratory cilia, and the effect of fluid elasticity on the swimming kinematics may act as a proxy for similar biological fluids, such as epithelial mucus in the airways. Although the flagella kinematics in Newtonian fluids have been well studied, the effect of fluid elasticity remains poorly understood. The impact of shear-dependent elastic stresses on the beating of cilia and flagella can have a profound influence on important biological processes such as fertility, mucus clearance, and respiratory health.

1.2. Thesis Overview and Synopsis

After the background information detailed in Chapter 2, the thesis will be divided into two main parts, namely physical systems and biological systems. The first part addresses the flow behaviors and instabilities of viscoelastic fluid in physical flow conditions, realized in microfluidic devices. The second part addresses biological systems, in particular, the locomotion and transport of active swimmers in viscoelastic fluids.

We begin with Chapter 3, the study of viscoelastic fluid in straight channel flows at low Reynolds number. Flow disturbances are introduced to the parallel shear flow by placing a variable number of cylinders upstream near the entrance. Following the onset of nonlinear subcritical instability, velocimetry measurements show non-periodic fluctuations over a broad range of frequencies, consistent with the main features of elastic turbulence. Within the same experimental setup, we compare these features to those in the flow around cylinders, located upstream of the parallel shear region; we find significant differences in power spectrum scaling, intermittency statistics, and flow structures. Further, using pressure measurements and high resolution holographic tracking, we establish the law of flow resistance via viscous friction factor f_η versus flow rate. Two regimes are found: a transitional regime marked by rapid increase in drag, and a turbulent-like regime characterized by a sudden decrease in drag and a weak dependence on flow rate. Lagrangian trajectories show finite transverse modulations not seen in Newtonian fluids. These curvature perturbations far downstream are found to generate sufficient hoop stresses to sustain the flow instabilities in the parallel shear flow.

In Chapter 4, we employ the same viscoelastic fluid and microchannel setup, but instead of probing the parallel shear region downstream, we look upstream and investigate the propagation of flow disturbances and the development of vortices upstream of a single cylinder. Using holographic velocimetry, we report the transitions of vortices upstream of the cylinder. First, we observe the emergence of two recirculation vortices in front of the cylinder that grows in length with Weissenberg number. As Weissenberg number further increases, the steady vortices become unsteady and ultimately fluctuate between two bi-stable states. Moreover, the flow disturbance travels upstream of the cylinder in the form of an elastic wave, whose wave speed increases with shear rate. On the other hand, the velocity fluctuations upstream are found to be uncorrelated with the flow immediately downstream of the cylinder, suggesting two distinct mechanisms of instability.

The discussion of purely elastic instabilities continues in Chapter 5 for the cross-slot channel, an extensional flow system. Using holographic particle-tracking and pressure measurements, we report a new symmetry-breaking instability that occurs *normal* to the extensional plane, in addition to the well studied symmetry breaking within the plane. It is marked by bi-stable flow switching and apparent “buckling” of the separatrix between the impinging streams. The disturbances propagate upstream with periods of synchronization and desynchronization. These complex flow structures may be present in other extensional geometries.

In Chapter 6, we turn over to biological system and study the swimming of bi-flagellated alga *Chlamydomonas reinhardtii* in viscoelastic fluids. We show that fluid elasticity strongly influences the flagellar beating kinematics in various aspects. First, the beating frequency and wave speed are increased compared to Newtonian fluid at similar viscosity. Despite the increase, however, fluid elasticity is found to adversely hinder net swimming speeds of the alga. Closer inspection of the flagellar beating pattern reveals strong modifications of the gait caused by fluid elasticity. To isolate the effect of elastic polymeric stress, we conduct numerical simulations of the stress and flow field around the swimmer using swimming kinematics obtained from experiments. We find that in viscoelastic fluids, cells employing the Newtonian strokes swim faster but generate larger stresses, use more power, and is less efficient compared to those using the viscoelastic strokes. Taken together, fluid elasticity couples with swimming gait in a complex and non-linear fashion that is not captured using viscous fluid theory alone.

Finally, Chapter 8 concludes the dissertation by summarizing the major contributions of this work. In addition, future prospects and potential directions on the subject of flow behavior of complex fluids and the impact of fluid property on the motility of micro-swimmers will be discussed.

CHAPTER 2 : Background

2.1. Lab-on-Chip and Microfluidics

Analogous to the revolution in computation power brought by integrated circuits, the advent of microfluidic technology has enabled vast miniaturization and parallelization of fluidic experiments in a wealth of applications. These include health diagnostics [23, 24], molecular biology [25, 26], cell level biomedical systems [27, 28], cell motility [29–33], organ on a chip [34–37], microliter or nanoliter scale rheology [17, 38–42], investigations of single polymer dynamics [43,44], elastic flow instabilities [17,22,45–50] and mimicking flows in porous media [51–54]. Figure 2.1 (a-c) illustrate a few examples among the broad spectrum of applications, namely biological protein reactions [2], chaotic mixing at the microscale [3], and perfusion systems capable of generating combinatorial concentration profiles for multiple species [4].

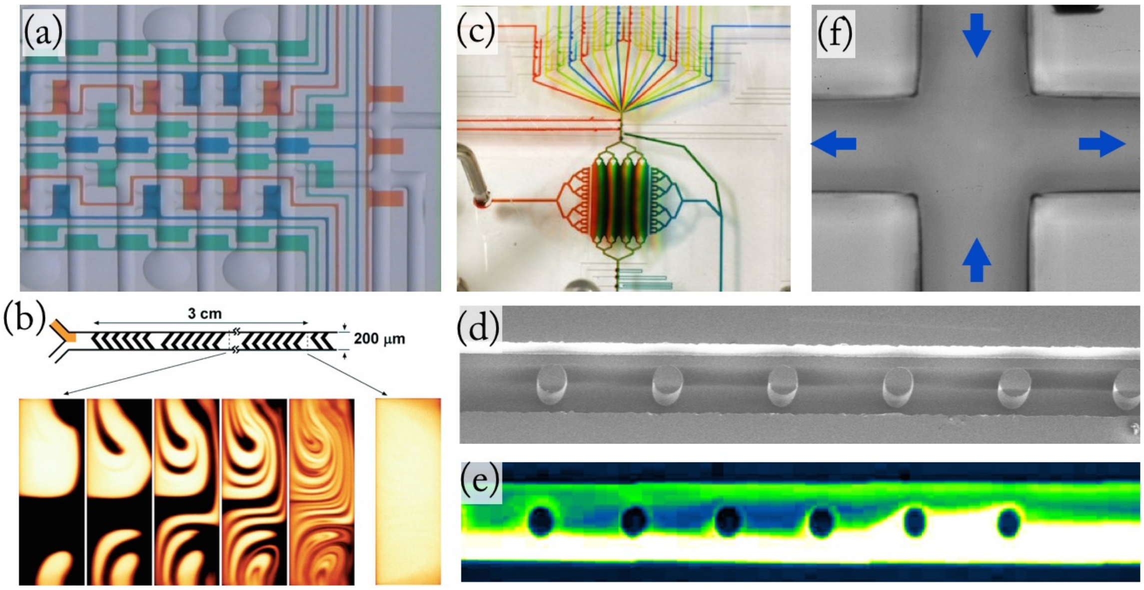

Figure 2.1: (a) Integrated fluidic chip measuring protein interactions, with scalable automation and parallelization [2] (circular chambers 250 μm in diameter). (b) Staggered Herringbone fluidic mixer to induce chaotic mixing at low Reynolds number [3]. (c) Combinatorial gradient generator in a microfluidic perfusion device [4]. (d-e) Straight microchannel and the linear array of cylinders used in the current study of elastic instability and turbulence (channel width 100 μm). (f) cross-slot micro-channel in the current study of elastic instability (channel width 100 μm).

The defining characteristic of microfluidics, namely the micro- to nanometer length scale L, provides many attractive advantages. The small sample volume required is particularly appealing to biomedical applications where the samples are usually expensive and rare. Furthermore, the portability, fast reaction time, low cost, and low power consumption makes the miniaturized system a potential candidate for massive parallelization and high throughput.

The length-scale found in microfluidic systems has another fluid dynamic implication: it allows the study of material and flow behaviors in the high shear and strong extension regime, without the plague of nonlinear inertial effects. Since the deformation rate scales with the length scale cubed $\dot{\gamma} \sim Q/L^3$ for a given flow rate Q, microfluidic channel easily access high extensional and shear rates. On the other hand, the ratio of inertial to viscous forces, as characterized by the Reynolds number (Re), scales only with $Re \sim Q/L$ and can be made less than unity. As viscous dissipation dominates, the flow inertia that leads to hydrodynamic instabilities and turbulence vanishes. Hence for simple Newtonian fluids, microfluidic system is the preferred platform to eliminate inertia. Hence for fluids with complex rheological properties, particularly viscoelasticity, microfluidics offers a unique window to isolate nonlinear flow behaviors that originate purely from the material properties.

In this work, we investigate the flow instabilities of viscoelastic fluids at low Re using microfluidic device. The straight micro-channel with the linear array of cylinders is shown in Fig. 2.1 (d,e) where the channel width is 100 μm. The cross-slot channel is shown in Fig. 2.1 (f). These microfluidic devices are made of polydimethylsiloxane (PDMS, Dow Corning Sylgard 184) using standard soft-lithography methods [55].

2.2. Flow Velocimetry Techniques

In this section, we introduce important flow velocimetry techniques suitable for the study of elastic flow instabilities in Part I and at the scale relevant to microfluidic systems. Three techniques are discussed, namely the micro-particle image velocimetry, particle tracking velocimetry, and holographic particle tracking velocimetry.

μPIV Technique – Traditionally, to resolve the velocity fields in macroscopic flow geometries, particle image velocimetry (PIV) with laser sheet illumination is often used [56, 57]. In this method, the motions of individual tracer particles are not resolved. Instead, image of densely seeded flow is partitioned into interrogation windows much larger than the particle. The windows are then cross-correlated between consecutive time frames to determine the most probable local displacement. For micron scale channel flows, micron-resolution particle image velocimetry(μPIV) inherits the method of conventional PIV yet tackles the unique challenges optical and mechanical constraints such as tracer size, illumination, and particle-image interrogation/post-processing algorithms [58]. Although high accuracy Eulerian velocity fields can be obtained using techniques such as ensemble averaging, the spatial resolution of the velocity field is heavily limited by the size of the interrogation window. The in-plane spatial resolution is around 1 micron (or above) for channels of dimension ∼100 micron in most advanced applications of this technique [58, 59].

PTV Technique – As an alternative, particle tracking velocimetry (PTV) technique can be used to potentially increase the spatial resolution at the particle-level [17, 47, 60, 61]. In this technique, developed by Crocker and Grier [60], particle centroids are directly estimated and then connected between frames to form a Lagrangian trajectory. Spatial resolution of the particle centroids for standard calibration systems that are two-dimensional with non-overlapping particles, can reach 0.02 pixels (or 10 nm for 100×) [60]. In 3-dimensional flow systems and epifluorescent microscopy, however, the out-of-plane heterogeneity and noise from particles outside the focal plane and reduce the actual spatial resolution and produce challenges in connecting centroids across frames. On the other hand, increasing optical magnification sacrifices precious field of view require to visualize the micro-channel setup. In our PTV setup, we use particles of 0.6 μm and 1 μm diameter imaged using conventional epifluorescent microscopy. A Zeiss Z1 inverted microscope with 63× N.A. 1.0 oil immersion objective. The objective's depth of focus is ± 2 μm, comparable to the particle diameter to minimize the out-of-plane contributions. A high-speed camera (up to 10^4 frames/s, Photron SA1.1) is used to resolve the fast varying temporal dynamics of the flow. In-house image processing, band pass filter, and particle search algorithms are used to connect consecutive particle centroids and discriminate spurious trajectories. The resultant spatial accuracy for this method is around 200 nm with velocity grid resolution of 1 μm.

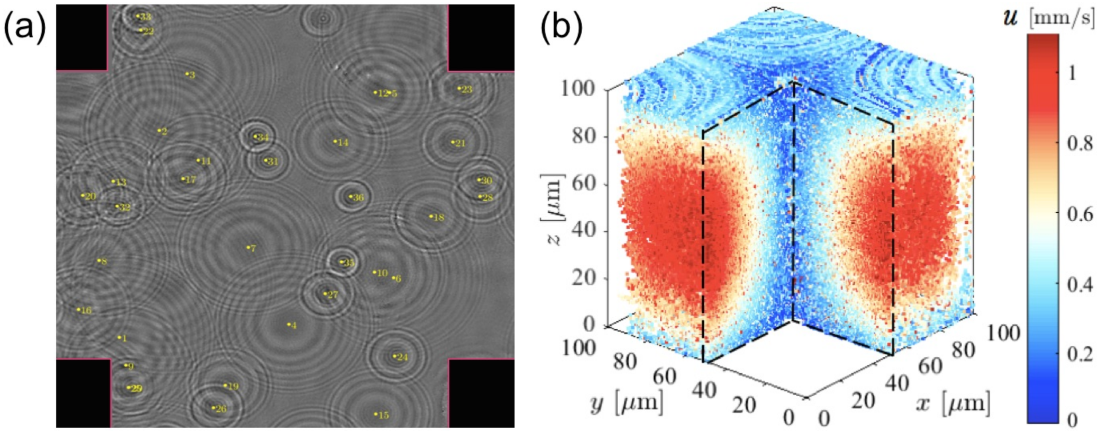

Figure 2.2: The holographic particle tracking technique, applied in the cross-slot channel geometry of the current study. (a) Typical particle scattering fields. (b) Ensemble of 3-dimensional particle trajectories obtained from the holographs.

Holographic PTV Technique – In order to obtain 3-dimensional Lagrangian particle trajectories at high spatial and temporal resolution, we use a holographic particle tracking scheme adapted from [62, 63]. The flow is seeded with tracers (1 μm diameter) which are imaged using an inverted microscope and a CMOS camera (5000 fps). Under a coherent light source (DPSS 532 nm Laser), tracer particles induce a light scattering field which is projected onto the imaging plane. This scattering image, after application of background subtract algorithm, is shown in Fig. 2.2(a) where identified particles are indexed in the order of their separation from the image plane. The out-of-plane (z) positions of tracer particles are reconstructed by finding the local maxima of the 3-d convolution field between the scattering image and the Rayleigh-Sommerfeld kernel. Standard particle tracking methods are then used to connect the centroids to form Lagrangian particle trajectories. To estimate the uncertainty at actual experimental conditions, we compute the standard deviation of the particle trajectories measured within the microchannel at experimental flow rates for a viscous Newtonian fluid where particle diffusion is negligible. The uncertainty of the particle centroid for actual microchannel conditions and seeding density (10^{-5} volume fraction), is around 30 nm for the in-plane (x, y) components and 0.6 μm for the out-of-plane z.

Finally, one can characterize the flow tracer fidelity with the particle Stokes number [64], which in the case of Stokes flow, amounts to $St = \rho_0 d_0 U/18\eta$, where ρ_0 is particle density, d_0 is particle diameter, U is the velocity of the flow, and η is the fluid viscosity. For the tracer particles and the viscosity of the working fluids used in the study of elastic flow instabilities, the Stokes number is small, $St \lesssim 10^{-6}$. This means particles will follow flow streamlines almost perfectly. The fractional error in tracer displacements due to Brownian noise can be estimated by $\varepsilon_B = \langle s^2 \rangle^{1/2}/\Delta x$, where $\langle s^2 \rangle$ is the mean square displacement of the tracer and Δx is the displacement due to advection [59]. Invoking the Einstein's relations, we find that even for the lowest flow rates in our experiments, $\varepsilon_B \lesssim 0.06\%$. Hence Brownian motion is negligible relative to the convective transport. Lastly, we note that the concentration of the tracer particles are dilute ($\lesssim 10^{-3}$ by volume in PTV and $\lesssim 10^{-5}$ in holographic PTV) and do not noticeably alter the properties of the fluid.

2.3. Constitutive Equations

The relationship between stress response and material deformation for many complex fluids, in particular viscoelastic fluids, is neither well understood nor perfectly captured by even the most sophisticated models. Yet the many advances in theoretical and numerical studies, based on constitutive modeling, are often times necessary to gain insights into the underlying physics. In this section, I will briefly discuss a well-known yet relatively simple constitutive model for viscoelastic fluids, the Oldroyd-B model.

Oldroyd-B fluid model has been a popular constitutive model for the study of flow of viscoelastic fluids, due to its formal simplicity, reasonable agreement of normal stresses with experiments in shear flows, and separate contributions of the solvent and polymer to the viscosity [65, 66]. These properties made Oldroyd-B model particularly appropriate for Boger fluids, which are highly elastic with minimal shear-thinning. The appeal of this model also lies on the fact that it can be derived from first principals by modeling polymer molecule as spherical beads joined together by linear Hookean spring [67].

In the Oldroyd-B model, the total stress $\boldsymbol{\tau}$ is written as the sum of the solvent stress contribution $\boldsymbol{\tau}_s$ and the polymer stress contribution $\boldsymbol{\tau}_p$ [65, 66], given by:

$$\boldsymbol{\tau} = \boldsymbol{\tau}_s + \boldsymbol{\tau}_p. \tag{2.1}$$

The solvent contribution, usually assumed to be Newtonian (e.g. water, glycerol), follows the usual Newton's law of viscosity and can be expressed as:

$$\boldsymbol{\tau}_s = \eta_s \big[\nabla \boldsymbol{u} + (\nabla \boldsymbol{u})^{\mathrm{T}}\big], \tag{2.2}$$

where η_s is the solvent viscosity, and $\nabla \boldsymbol{u}$ is the velocity gradient. The polymer stress contribution to the total stress, however, can be modeled by considering the elastic spring force that joins the beads, the drag force exerted by the solvent, and Brownian motion. The result can be described by the following evolution equation for polymeric stress:

$$\boldsymbol{\tau}_p + \lambda \overset{\triangledown}{\boldsymbol{\tau}}_p = \eta_p \big[\nabla \boldsymbol{u} + (\nabla \boldsymbol{u})^{\mathrm{T}}\big], \tag{2.3}$$

where λ is the fluid relaxation time, η_p is the polymer viscosity contribution, and $\overset{\triangledown}{\boldsymbol{\tau}}_p$ denotes the upper-convected derivative defined as:

$$\overset{\triangledown}{\boldsymbol{\tau}}_p = \frac{\partial \boldsymbol{\tau}_p}{\partial t} + \boldsymbol{u} \cdot \nabla \boldsymbol{\tau}_p - (\nabla \boldsymbol{u})^{\mathrm{T}} \cdot \boldsymbol{\tau}_p - \boldsymbol{\tau}_p \cdot \nabla \boldsymbol{u}. \tag{2.4}$$

Note that the first two terms are the usual material acceleration due to unsteadiness and advection, while $-(\nabla \boldsymbol{u})^{\mathrm{T}} \cdot \boldsymbol{\tau}_p - \boldsymbol{\tau}_p \cdot \nabla \boldsymbol{u}$ is the rate of change of stress as observed while translating and deforming with the fluid. Such coupling of polymeric stress and deformation brings nonlinearities to the constitutive equation and is the root of many flow anomalies, even when the inertia is absent.

For steady simple shear, Oldroyd-B model predicts that the shear stress is:

$$\tau_{xy} = (\eta_s + \eta_p)\dot{\gamma}_{xy}, \tag{2.5}$$

which suggests the viscosity is the sum of the solvent and polymeric viscosity contributions. The 1st normal stress difference, in steady shear, is quadratic in shear rate:

$$N_1 = 2\eta_p \lambda \dot{\gamma}_{yx}^2, \tag{2.6}$$

which agrees well with the rheology of Boger fluids.

The Oldroyd-B model is one of many possible constitutive models for viscoelastic liquids and suffers several limitations. For example, it does not capture the shear thinning behavior present in most polymeric fluid. More importantly, this model does not impose a limit on the extension of the linear springs, which can grow unbounded in extensional flows and lead to infinite stress [68], which is apparently unphysical. Due to these limitations, other models have been developed including the Finite Extensibility Nonlinear Elastic (FENE) model and its variations (e.g. FENE-P, FENE-PM, for detailed comparison see [69]). For example, FENE-P model accounts for the finite extensibility of polymer molecules and exhibits shear-thinning behavior [70–72]. In steady shear, FENE-P predicts

$$N_1 \propto \left\{ \sinh\left[\frac{1}{3}\,\mathrm{arcsinh}\,(\alpha\lambda\dot{\gamma})\right]\right\}^2 \tag{2.7}$$

which approaches $\dot{\gamma}^{2/3}$ for large shear rates and $\dot{\gamma}^2$ at low shear rates. Despite these improvements, FENE-P model is not able to describe the broad distribution of relaxation times in most polymeric fluids.

In general, all such models have strengths and limitations and the true test of validity for any constitutive models is whether it predicts the primary rheological responses of the viscoelastic fluid as measured in laboratory rheometric tests, which we describe below.

2.4. Rheology of Viscoelastic Fluids

The addition of long chain polymers to a Newtonian fluid can strongly modify its rheology, imparting solid-like behavior known as viscoelasticity. The most pronounced features of these fluids, as measured by carefully designed rheological tests, are a non-zero normal stress difference and a memory of past deformation within a time frame known as the relaxation time. In the previous section, we discussed the constitutive models that attempt to captures these features. Here, I will briefly discuss the rheometry – i.e. the measurement and quantification of the flow of fluids – that is essential to the study of the flow behavior and transport of any complex fluid, in particular polymeric solution.

In a gross sense, a rheometer is a device that measures the material response, usually stress or deformation, to an imposed perturbation, large or small, steady or unsteady, shearing or elongational. Common geometries used in macroscopic rheometers include capillary tube, cone-and-bob, parallel plate, and cone-and-plate geometries. However, the cone-plate geometry, shown in Fig. 2.3(a), stands out for the uniform flow shear rates within the gap and has been the most commonly used geometry for characterizing fluid properties of non-Newtonian fluids.

In cone-and-plate rheometers, The test fluid is placed between the bottom horizontal plate and an upper cone with a shallow angle ($\beta < 6^{\circ}$). The shear rate within the gap is uniform and given by:

$$\dot{\gamma} \approx \frac{\omega}{\beta}, \tag{2.8}$$

where ω is the rotational speed of the cone. The first normal stress difference N_1 can be obtained by measuring the vertical thrust force F_z and is given by:

$$N_1 = \frac{2F_z}{\pi R^2}, \tag{2.9}$$

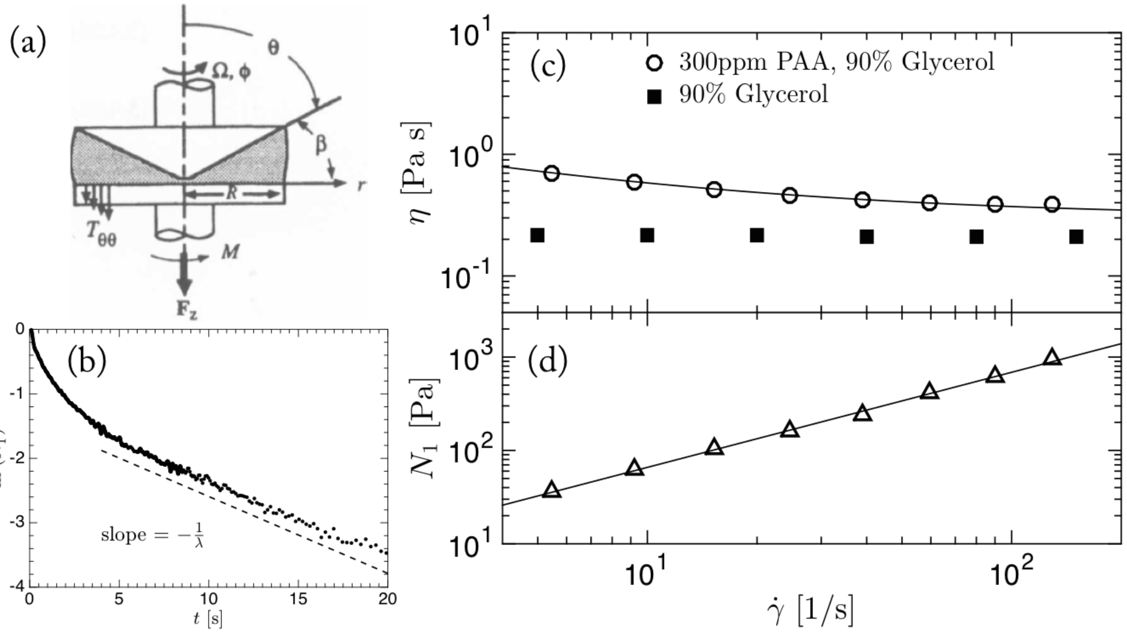

Figure 2.3: (a) Schematic of the cone-and-plate rheometer, adapted from the classic book by Macosko [5]. (b) Stress relaxation in the cessation of shear test for 300 ppm polyacrylamide (PAA, 18×10^6 MW) solution in 90% glycerol using cone-and-plate rheometer. The shear rate applied is 10 s^{-1}. (c) Steady shear viscosity and (d) first normal stress difference for 300 ppm PAA solution in 90% glycerol obtained using cone-and-plate rheometer at 21 °C.

where R is the radius of the cone.

Once the geometry has been chosen, various steady and unsteady dynamical tests can be conducted to probe the rheological response of the viscoelastic fluids. For instance, in small amplitude oscillatory shear (SAOS), one can observe the presence of a stress component that is in-phase with strain [73], contrary to Newtonian fluids where stress is purely in-phase with strain rate. In capillary filament thinning tests, where the diameter of the filament decreases linearly in time for Newtonian fluids, an elastic fluid, in contrast, thins exponentially with characteristic time of $3\lambda_c$ [74] (valid after the initial viscous regime but before the late-time finite extension regime). Here λ_c is closely related to the longest relaxation time of the fluid and sets the crossover time scale between solid-like behavior versus liquid-like behavior. In step shear strain and steady shear cessation tests, the stress also relaxes with characteristic time λ [73]. Figure 2.3(b) shows the stress relaxation after cessation of steady shear for the particular fluid we will be using to study elastic instabilities. We see that after a rapid initial decay in the inertial regime, the stress decays with a fairly constant time scale λ. Yet we note that the fluid in fact has a spectrum of relaxation times and the λ here is the dominant one. In steady shear, one can clearly observe a non-zero normal stress difference for viscoelastic fluids. These elastic stresses are due to the stretching of the polymers and in general, grow with increasing shear rate prior to the finite extensibility regime. Also, a shear-thinning viscosity is often present when the solvent viscosity is significantly lower than the polymer contribution. Figure 2.3 (c,d) illustrates these two behaviors for the same polymeric solution shown in (b). These complex material responses of viscoelastic fluids give rise to a range of applications as well as challenges in both physical flow systems and biological processes, whose context we introduce next.

2.5. Part I: Flow Anomalies of Viscoelastic Fluids

2.5.1. Inspirations from Newtonian Pipe Turbulence

In this section, we review several aspects of the pipe turbulence of Newtonian fluids, in particular the transition from laminar to turbulent, the coherent structures, and the key features of turbulence. The phenomenology is deeply intriguing and the insights gained serve as a roadmap where many analogies can be made for our study of elastic instability in channel flows.

Hydrodynamic instabilities and turbulence have long attracted the attention of engineers and scientists. In 1883, Osborne Reynolds presented the seminal experimental study of turbulence transition in pipe flow [6]. He found that: (i) when the velocity of water is low, layers of fluid flow smoothly in parallel without mixing, i.e. laminar, as shown in Fig. 2.4(a); (ii) at intermediate flow rate, a certain amplitude of perturbation is needed to drive the dye stream to curl and penetrate into the surrounding water at a considerable distance from the inlet (Fig. 2.4 b); (iii) when the velocity is sufficiently high, the steady laminar flow breaks down and the dye stream quickly disperses into the surrounding water showing

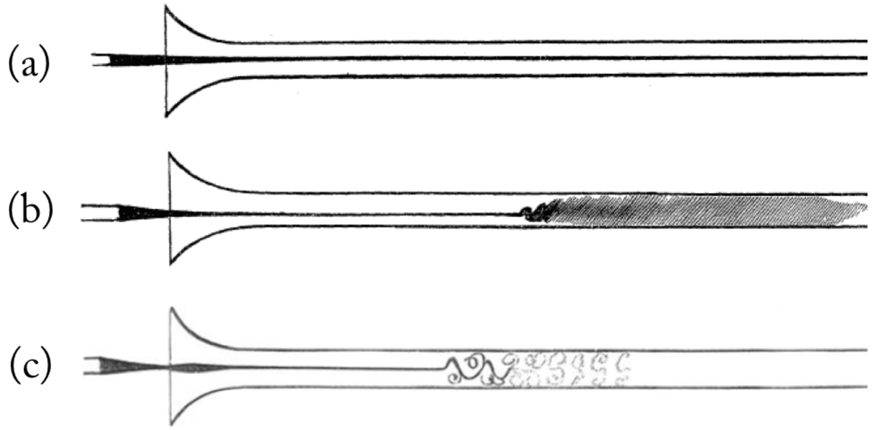

Figure 2.4: Experimental results of the flow of water in pipes by Osborne Reynolds [6]. (a) Direct flow where the dye stream is smooth and straight. (b) Sinuous flow where the dye stream mixes and penetrates the surrounding fluid far from the inlet. (c) At sufficiently high flow rate, the dye stream quickly disperses into the surrounding fluid in eddies and curls.

distinct eddies (Fig. 2.4 c). Reynolds also showed for the first time the transition from a laminar and steady flow state to a sinuous and irregular one is controlled by a dimensionless parameter, later called the Reynolds number (Re). This dimensionless number characterizes the level of nonlinear inertial forces relative to viscous damping forces in the flow.

More than a century after Reynolds' experiments, the mechanism governing the transition in pipe flow is still an unsolved mystery. In contrast to other laminar-turbulence transitions where the base flow is linearly unstable and a sequence of flow instabilities provide possible routes to turbulence, the transition in pipe flow occurs suddenly and fully [9]. The Poiseuille base flow is linearly stable, yet transitions can be subcritical and patches of turbulence can emerge in the form of localized "puffs" surrounded by laminar flow at moderate Re ($1800 < Re < 2500$) [75].

The discovery of transient traveling waves marks a major advance in pipe turbulence. First found numerically, these traveling waves, or coherent structures moving at constant wave speed, are the unstable solutions to the Navier-Stokes equation [76]. In their multitude, they form a chaotic repellor in phase space [77], which gives rise to long-lived turbulent transients. The experimental evidence of these transient flow states is later reported by Hof

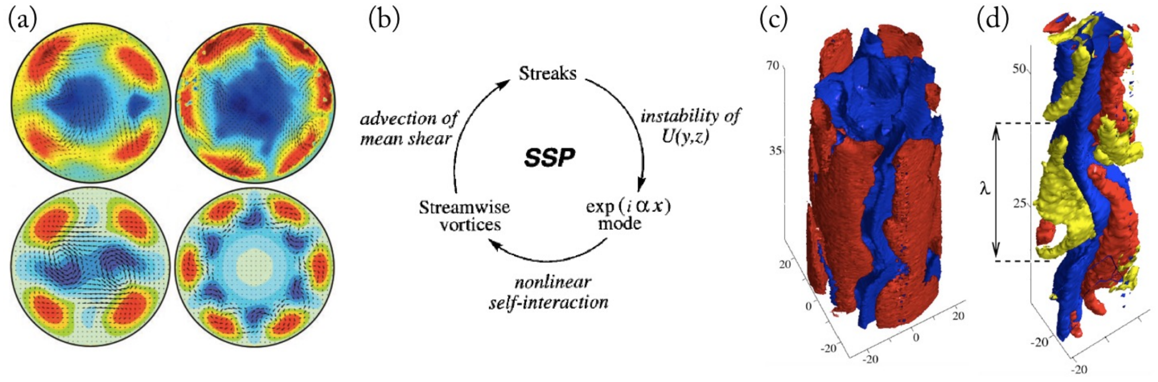

Figure 2.5: Coherent traveling wave structures and the self-sustaining process. (a) Comparison of experimentally (top) and numerically (bottom) observed streak patterns on a cross-section of turbulent pipe flow [7]. Arrows indicate in plane components while color indicates deviation from the parabolic profile. Left column shows traveling waves with C_2 symmetry mode and right shows C_6. (b) the self-sustaining process proposed by Waleffe [8]. (c,d) Experimental evidence of the regeneration process [9]. (c) Three-dimensional reconstruction of the low-speed (blue) and high-speed (red) streaks. (d) The formal appearance of wavy streaks (blue) sandwiched by counter-rotating streamwise vortices (yellow and red). The periodicity λ is shared by both the wavy streak as well as from the vortices.

et al [7]. Figure 2.5(a) top row shows the experimentally observed high speed streaks and low speed streaks of the streamwise velocity within a cross section of the pipe, showing the presence of traveling waves. Excellent agreement with the numerical prediction (bottom row) [77, 78] are found for both the C_2 and C_4 symmetry modes (first and second column). This discovery forms an important piece to the self-sustaining process proposed by Waleffe [8, 79], shown in 2.5(b). In this conjecture, streamwise vortices that redistribute the mean shear create streaks, which become inflexionally unstable. Nonlinear self-interaction of the unstable modes then regenerates the streamwise vortices, closing the self-sustained loop [7, 8]. Again, the experimental evidence of such regeneration cycle is reported by Hof *et al* [9] and Fig. 2.5(c) shows that the low-speed streak (blue) undergoes a wavy instability while (d) shows counter-rotating streamwise vortices (yellow and red) surrounding the wavy streak (blue). Taken together, we conclude that the traveling wave coherent states are indeed crucial in organizing turbulence pipe flows.

Although the transition to turbulence is highly individualistic to the flow geometry, once the

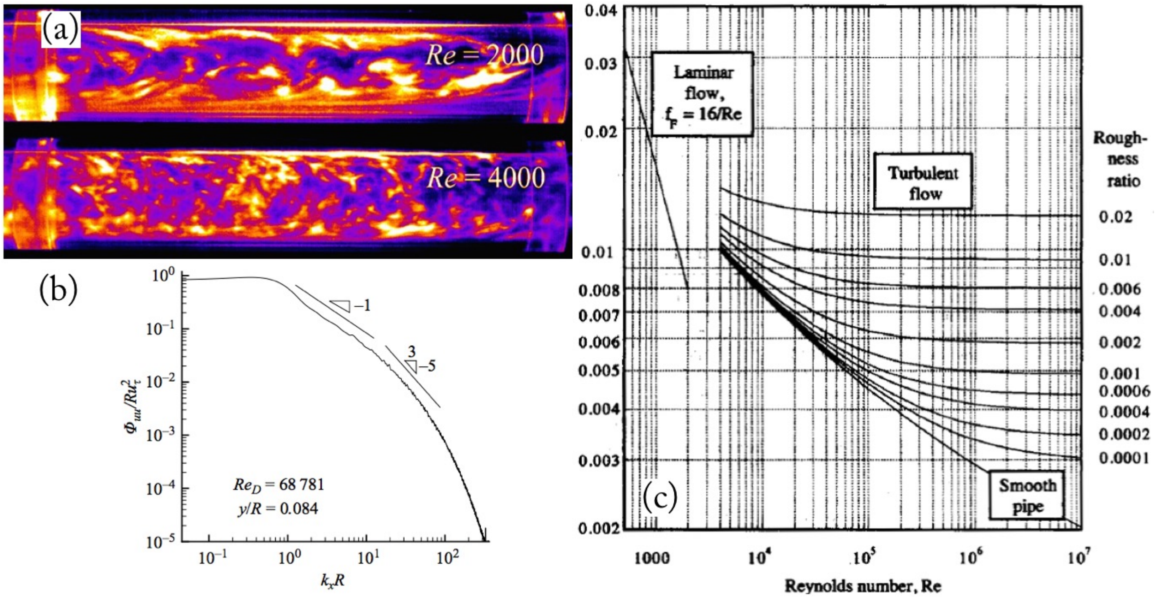

Figure 2.6: Features of turbulence in pipes. (a) Highly irregular flow structures and enhanced mixing [Courtesy J. Peixinho and T. Mullin]. (b) Flow is activated at many time scales and length scales; velocity spectra follow power-law decays [10]. (c) Strong increase in flow resistance compared to the laminar base flow, depicted by the Moody diagram [11].

flow becomes fully turbulent, however, many universal features emerge. These includes: (i) highly irregular flow structures and enhanced mixing, see Fig. 2.6(a), where the length-scales of the structures become progressive finer as *Re* increases; (ii) flow is activated at many time-scales and length-scales and velocity spectra follows the almost universal 5/3 power-law decay [10], as shown in Fig. 2.6(b); (iii) strong increase in flow resistance compared to the laminar base flow due to turbulent structures and enhanced momentum transport. The friction factor versus *Re* is shown by the Moody diagram, reproduced here in Fig. 2.6(c) [11]. Although the singular driving force of nonlinearity is inertia, these flow characteristics of Newtonian pipe turbulence will be particularly relevant for our study of elastic turbulence at low Reynolds number.

2.5.2. Elastic Instabilities and Elastic Turbulence in Curved Geometries

Fluids containing polymers are found in everyday life, from food, paint, to cosmetics, and in technologies spanning the oil, pharmaceutical, and chemical industries. As the polymers stretch and align with the flow, they develop elastic stresses that are history-dependent, anisotropic, and relaxes with time scale λ. These extra stresses are nonlinear under shear and can dramatically alter the flow behavior. At low Reynolds numbers where inertia is negligible, elastic stresses can lead to a new class of flow instabilities not found in ordinary fluids like water. They can also exhibit a new type of disordered flow called elastic turbulence – a turbulent-like regime existing far below the dissipation scale [13, 22, 80].

A wealth of the studies of elastic instabilities and elastic turbulence are conducted in systems where the mean flow is strongly curved, such as the flow between rotating disk [13, 81, 82], between concentric cylinders [12, 80, 83, 84], serpentine channels [22], cross-slot channels [47,48,85], and around cylinders [86,87]. In these systems, high velocity gradients stretch the polymer and the curved streamlines induce a so-called “hoop stress” which has a component normal to the streamlines and can amplify secondary flow perturbations.

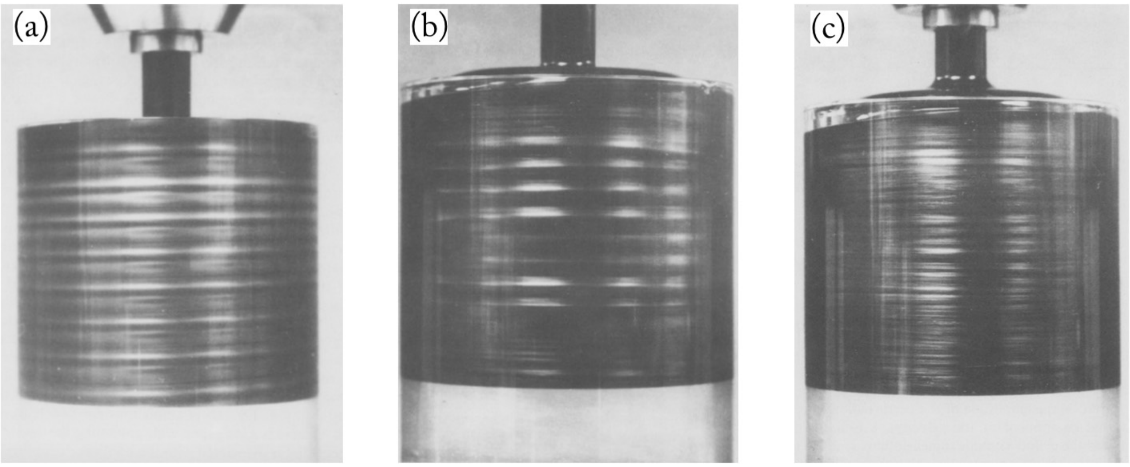

Figure 2.7: Photographs of purely elastic instability in Taylor-Couette flow by Muller, Larson and Shaqfeh [12]. The flow structures are made visible by adding mica flakes. (a) Taylor cell instability of a Newtonian fluid (glycerol solution). (b) The onset of elastic instability at low inertia and Taylor number. (c) The irregular multi-wavelength structure at late times.

For example, in a classic experiment done by Larson, Shaqfeh, and Muller, a secondary cellular instability was observed in Taylor-Couette flow of of polymer solutions at vanishing Taylor number [12, 83]. The polymeric fluid used is a 1000 ppm polyisobutylene (PIB) solution dissolved in a highly viscous polybutene (PB) Newtonian solvent. Such dilute solution of high molecular weight polymers (e.g. PIB, PAA) dissolved in a low molecular weight viscous solvent (e.g. PB, glycerol) are known as Boger fluid which is highly elastic with minimal shear thinning viscosity [66, 88]. For Newtonian fluids at high enough Taylor number ($\sim 10^3$), a series of toroidal vortices, known as Taylor vortices emerges along the circumference, shown in Fig. 2.7 (a). Strikingly, when the Newtonian fluid is replaced with Boger fluid, they find that even without inertia (vanishing Taylor number), the onset of toroidal vortices still occurred, (Fig. 2.7 b). At short times, this banded vortex structure is comparable to the inertia-driven Taylor vortices with approximately the same wavelength. At long times (more than 1000 s), however, the banded vortex structure becomes highly irregular with multiple wavelengths (Fig. 2.7 c).

Groisman and Steinberg continued to study other geometries with curved streamlines and showed that following the onset of elastic instabilities, viscoelastic fluids at high shear rates can display many flow features that resemble those found in Newtonian turbulence [13, 22, 89]. In particular, for the parallel plate system shown in Fig. 2.8 (a), they found highly irregular flow structures and mixing patterns (Fig. 2.8 b), similar to that reported by Muller, Larson and Shaqfeh in the Taylor-Couette flow. Moreover, the flow is activated at many times scales and velocity spectra follow a steep -3.5 decay law shown in Fig. 2.8 (d). By mounting the system on a commercial rheometer, they also measured both the torque needed to drive the flow and the flow resistance. Compared to the predicted laminar flow, the viscoelastic drag is seen to increase by a factor of twenty following the transition to irregular flow. Despite the arbitrarily low Reynolds number, these observations match the main features of developed turbulence [90].

The origin of these flow anomalies of viscoelastic fluids lies in the extra elastic stress that develops due to the mechanical response of the polymers to external flow. At high velocity gradients, the polymer molecules can be stretched to an elongated state from a “coiled” state [73] [43]. The level of stretching experienced by the polymers can be quantified by

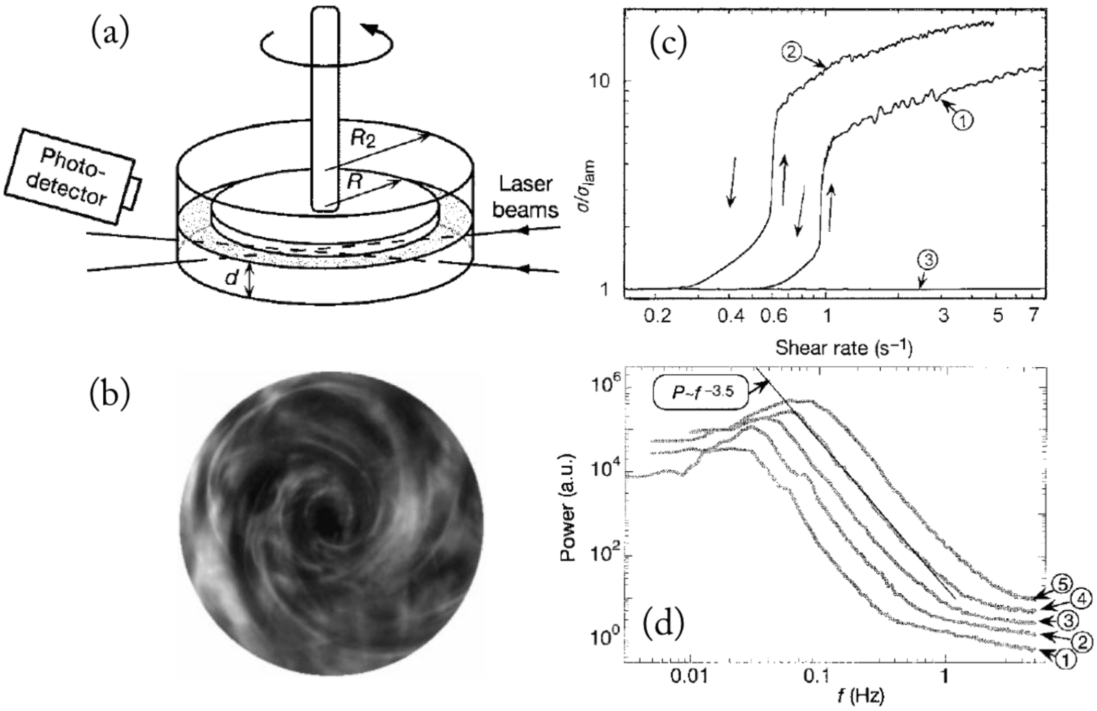

Figure 2.8: The study of elastic instabilities in parallel plates by Groisman and Steinberg, leading to the so-called "elastic turbulence" [13]. (a) The system is mounted on a commercial rheometer for torque measurements in addition to the laser Doppler velocimetry measurements. The fluid used is 80ppm polyacrylamide (PAA) in 65% saccharose and 1% NaCl in water. (b) Bottom view of the flow pattern visualized using Kalliroscope flakes. (c) Stress ratio relative to a computed laminar value shows a clear transition in flow resistance. Curve 1,2 are for two different plate diameters. Curve 3 is for Newtonian solvent. (d) Power spectra of velocity fluctuations for various shear rates in the unstable regime.

the Weissenberg number, defined as $Wi = \lambda\dot{\gamma}$ where $\dot{\gamma}$ is the flow shear rate and λ is the fluid relaxation time [91]. When Wi is increased beyond a critical value (around unity), polymer molecules unravel and become increasingly stretched until the nonlinear elasticity limits further extension. This "coil-stretch" transition is first seen in extensional flows and is later found to be strongly hysteretic [43, 92–94]. In shear flows, however, the average polymer extension does not display a sharp coil-stretch transition. Instead, they undergo large and frequent excursions in extension, and unstable "tumbling" events [95].

A classic example of flow phenomenon due to the stretching of flexible molecules is the so-called "rod-climbing" effect, where a viscoelastic fluid creeps up a rotating rod [14],

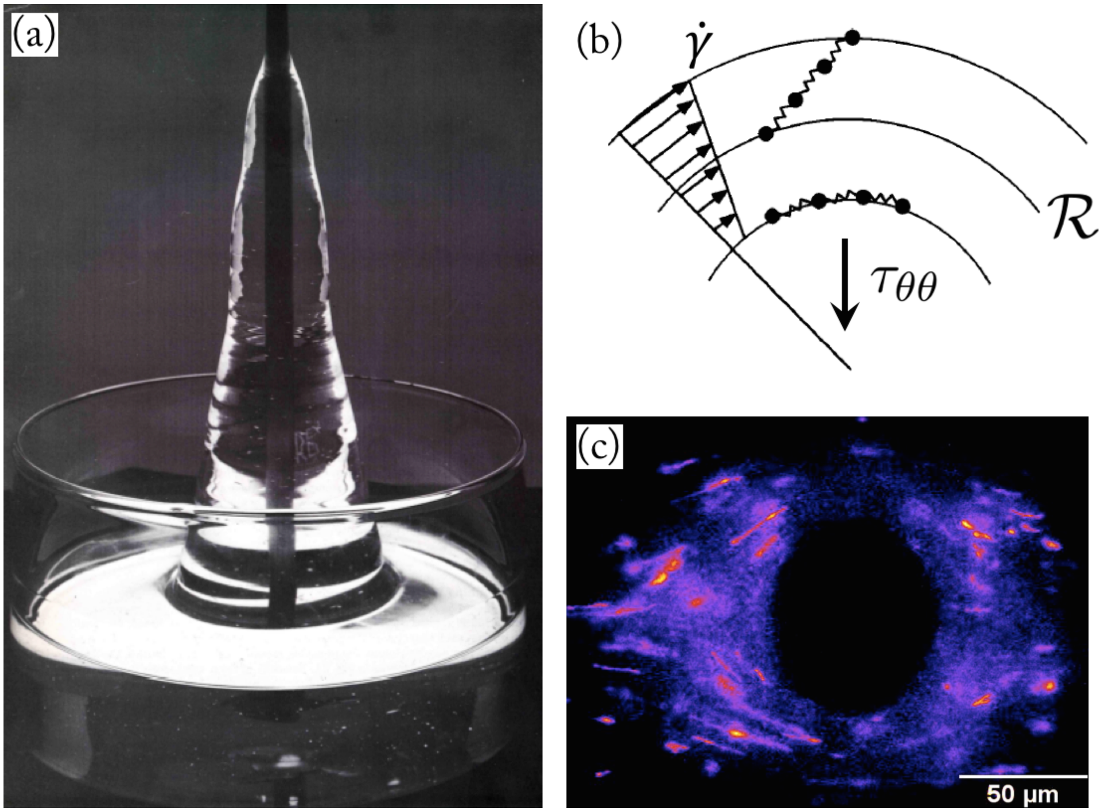

Figure 2.9: Macroscopic "rod-climbing" and its microscopic origin. (a) Rod-climbing (Weissenberg) effect of a viscoelastic fluid around a rotating rod [14]. (b) The radial component associated with the "hoop stress" generated by polymer stretching in flow with curved streamlines. (c) Flow of polymeric solution around a cylinder, visualized by fluorescently labeled lambda-DNA tracer molecules, Arratia lab.

shown in Fig. 2.9 (a). The force responsible for this effect lies in the centripetal stress component associated with the "hoop stress" generated by the shear-induced stretching of polymer molecules in the flow, shown schematically in Fig. 2.9 (b). The $\tau_{\theta\theta}$ component, which for Newtonian fluid points outward, is instead directed inward along the radius of curvature $\mathcal{R}$ for viscoelastic fluids and can generate a centripetal body force that pushes the fluid inward and up. Figure 2.9(c) shows the microscopic view of this picture in a slightly different condition. Here, a fluid with fluorescently labelled long-chain DNA molecules is flown around a cylinder from left to right. As they travel near the obstacle, the DNA molecules are seen to align with the streamlines and stretch to their extended states.

The heuristic principal sketched here can be generalized and made rigorous in many systems with streamline curvature. In fact, it has been argued that curved streamlines are a necessary condition for infinitesimal perturbations to be amplified by the normal stress imbalances in viscoelastic flows. The Pakdel-McKinley criterion, proposed from linear stability arguments, can be written as [83, 96, 97]:

$$\left[\frac{\lambda U}{\mathcal{R}} \frac{N_1}{\tau_{p,s}(\dot{\gamma})}\right]^{1/2} \geq M, \tag{2.10}$$

where M is a constant that depends on the type of flow geometry, U is a typical velocity along the streamlines, $\mathcal{R}$ is the radius of curvature, and $\tau_{p,s}(\dot{\gamma})$ is the polymeric shear stress. According to this criterion, purely elastic linear instabilities are not possible in parallel shear flow such as plane Poiseuille flow and pipe flow, and infinitesimal perturbations decay at a rate proportional to $1/\lambda$ [96, 98].

2.5.3. Nonlinear Subcritical Instability in Parallel Shear Flows

Yet linear stability of the base flow does not imply a global stability. Indeed, there has been mounting evidence that the flow of viscoelastic fluids in pipes and straight channels are nonlinearly unstable and undergo a subcritical instability at sufficiently high flow rates even at low Re [15–17, 99–101]. A possible route to unstable flows gradually emerges following a series of theoretical investigations demonstrating the possibility of a subcritical bifurcation from the linearly stable base states [15, 16, 99]. The basic argument is that following a sufficiently strong perturbation to the streamline, such as the one shown in Fig. 2.10(a), the locally generated curvature can then drive the flow unstable via same instability mechanism in curved systems at high enough Weissenberg number Wi. The leads to the subcritical bifurcation shown in Fig. 2.10(b), where flow perturbations below the critical threshold (dashed line) will decay while those above it will survive and drive the flow unstable. Moreover, this threshold is lowered for increasing control parameter Wi. Using nonlinear stability analysis on the plane Couette flow of the Upper-Convected Maxwell fluid, Morozov and von Saarloos identified such threshold amplitude of the perturbation [15], as

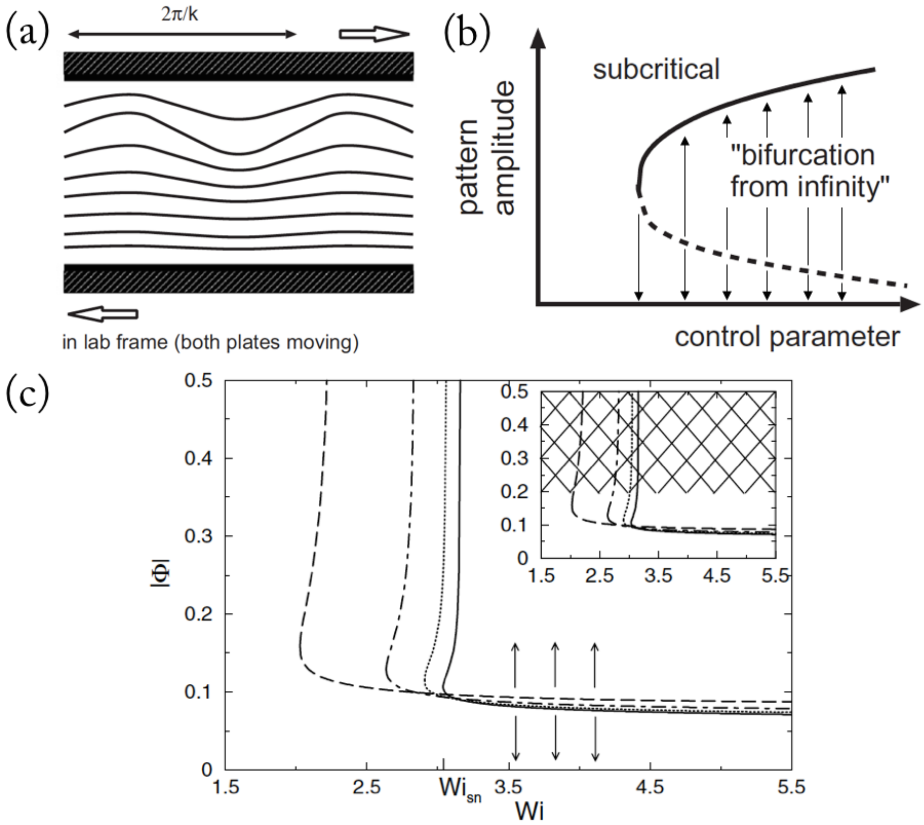

Figure 2.10: Theoretical evidence of a possible subcritical instability in plane Couette flow [15, 16]. (a) Finite amplitude perturbation on the streamline generates local curvature, from [16]. (b) "Bifurcation from infinity", or the subcritical instability where the base flow is linearly stable for all values of control parameter, may characterize the transition in parallel shear flows [16]. (c) Stability phase diagram obtained from nonlinear stability analysis of plane Couette flow for the Upper-Convected Maxwell fluid [15].

shown in Fig. 2.10(c).

Other theoretical investigations using non-modal analysis predict the transient growth of perturbation [102, 103]. Their results show that streamwise velocity fluctuations can be significantly amplified for viscoelastic fluids in the absence of inertia. Subsequent experiments in small pipes found unusually large velocity fluctuations that are activated at many time scales [101] and experiments on polymer melt extrusion found hysteretic behavior in the melt fracture instability [100].

More recently, experiments in a straight long microchannel using a linear array of cylin-

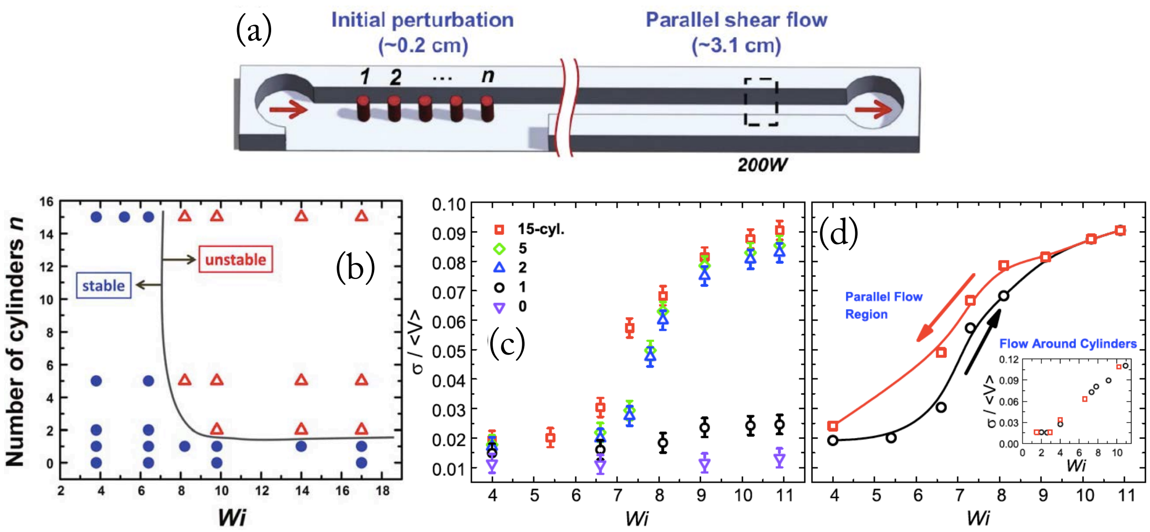

Figure 2.11: Experiment in microchannel with flow perturbation generated by a linear array of cylinders demonstrates the nonlinear subcritical instability of a viscoelastic fluid in parallel shear flow [17]. (a) Device schematic. (b) Stability phase diagram consisting of the degree of nonlinear elastic stresses (Wi) and the level of perturbation (n). (c) Normalized velocity fluctuation showing the bifurcation depends on both the perturbation by the cylinders as well as Wi. (d) Hysteretic loop of velocity fluctuations between ramping up and down.

ders as flow perturbation found strong evidence of a nonlinear subcritical transition to an unstable state of sustained flow fluctuations [17]. The schematic of the setup is shown in Fig. 2.11(a) where the channel length is about 300 times the channel width ($W = 100$ μm). The region of initial flow perturbation by the cylinders lasts about 6% of the channel length, and the number of cylinders is adjusted to varying the level of flow perturbation. The flow of a Boger-like fluid, a 300ppm PAA dissolved in 90% glycerol by weight solution, is monitored far downstream in the parallel shear region at $x = 200W$. They find that, above a critical level of perturbation and flow rate, a sudden onset of sustained velocity fluctuations is observed. In contrast, the flow at lower Wi or when the number of cylinders is less than 2, has minimal fluctuation, on par with the level of instrument noise. This behavior is quantified in Fig. 2.11(c) where the normalized velocity fluctuation is shown for various Wi and the number of cylinders n. For $n \leq 1$, the flow shows minimal fluctuation at all Wi investigated. For $n \geq 2$, however, a sudden transition to sustained high levels of fluctuations is observed beyond a critical Wi. The stability phase diagram can be plotted (Fig. 2.11b) which reflects such dependency of the transition on the perturbation level. Note the striking agreement here with the theoretical analysis shown in Fig. 2.10(c). Further, a flow hysteresis between ramping up and ramping down in flow rate is identified in the parallel flow region (Fig. 2.10d) which occurs due to the inflection of the stability curve, typical for a subcritical transition.

Taken together, the above features strongly suggest the existence of a nonlinear finite amplitude transition in the parallel shear flow of a viscoelastic fluid. The instability is subcritical – a sudden onset of sustained velocity fluctuations above a perturbation threshold and a critical flow rate. This scenario is akin to the transition from laminar to turbulent flow of Newtonian fluids in pipe flows [6,104], except the driving force is elastic stresses rather than inertia.

Yet many questions remain unanswered. Unlike the Newtonian pipe turbulence, however, little is known about the basic structures organizing the instability and the law of resistance (i.e. pressure loss due to friction) as the flow transitions from a stable to an unstable state. Further, is there characteristics of elastic turbulence? What are the phenomenological distinctions between polymeric flow in parallel shear flows compared to that in curved geometries, given that the transition mechanisms are markedly different? Lastly, can we find direct experimental evidence for the "instability upon an instability" picture for subcritical transition?

2.6. Part II: Locomotion and Transport in Viscoelastic Fluids

In this section, we first introduce some well established results and previous work on the locomotion of active swimmers at the microscale. Then we shift our focus to the swimming in viscoelastic fluids.

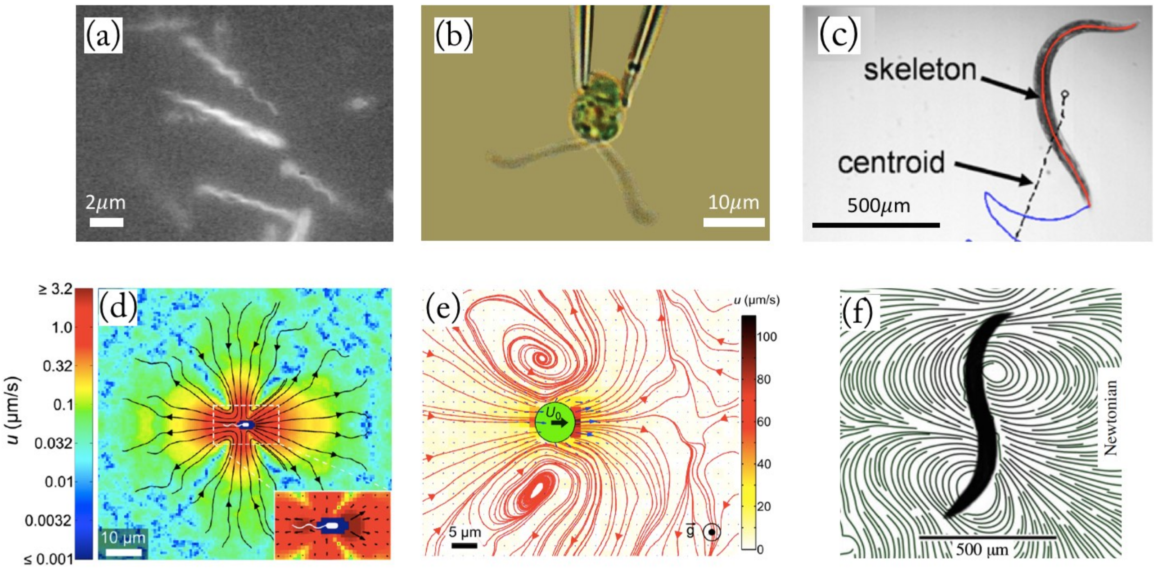

Figure 2.12: Micro-swimmers and the flow fields that they generate. (a) Bacteria *Escherichia coli* with helical flagella, courtesy Howard Berg, and (d) the positive force dipole field generated. (b) Bi-flagellated green alga *Chlamydomonas reinhardtii* [18] and (e) the flow streamlines around it, resemble those generated by a negative force dipole [19]. (c) Millimeter-scale roundworm *Caenorhabditis elegans* [20] and (f) the streamlines around the swimmer [21].

2.6.1. Swimming at Low Reynolds Number

The swimming of micro-organisms at low Reynolds number is a classic fluid dynamics problem motivated by important biological processes found in nature. Here we define the Reynolds number as $Re = U\ell/\nu$, where U is the velocity of the swimmer, ℓ is the length scale of the swimmer, and ν is the fluid kinematic viscosity. For micrometer-size swimmers, such as bacteria, algae, and spermatozoa, the Reynolds number is usually far less than unity and linear viscous drag dominates over nonlinear inertia. The lack of inertia has many consequences in the fluid dynamics of the swimming. The equations of motion become time-reversible and any reciprocal motion brings the swimmer back to its original location, a curse known as the "Scallop theorem" [105]. Moreover, without inertia all forward motion comes to a halt once the swimmer stops its action and coasting is impossible. To achieve locomotion at low Reynolds number therefore, micro-swimmers device a wide range of swimming strategies. These include: (i) pushers such as the bacteria *Escherichia coli* with rotating helical propellers or flagella located on the trailing side of the swimming direction, (ii) pullers such as the green algae *Chlamydomonas reinhardtii* with a pair of flexible oars located on the leading side of the swimming direction [18], and (iii) undulatory swimmers such as *Caenorhabditis elegans* with body deformations resembling traveling waves. Figure 2.12(a-c) illustrate these three types of swimmers. Of course, the crude classification here does not address the rich complexity of swimming methods such as squirmers with surface tangential waves and metachronal waves (alga *Volvox carteri*) [106] and swimming dynamics such as the run-and-tumble or run-reverse-flick behavior of bacteria [107].

Understanding the locomotion of these micro-organisms at low Reynolds number can led to profound insights and practical control on how they feed, spread, and proliferate. A classic example is the chemotaxis of *E. coli* towards regions with higher nutrient concentration, where swimming bias is generated by suppressed run-and-tumble reorientation when swimming up the chemical gradient [108]. With the advent of medical robotics, the development of micro-scale artificial swimmers has gain tremendous popularity, driven by applications such as targeted drug delivery and robotic surgery. One of the leading avenues of such research is the use of magnetic fields to actuate micro-fabricated bio-inspired helical structures in fluids [109] and catalytic artificial swimmers for drug delivery [110] among others.

Extensive progress has been made to understand the underlying physics of swimming at low Reynolds number in Newtonian fluids. Early theoretical works use geometric abstractions of the swimming motion and resolve the full flow fields around the swimmer. Sir Geoffrey Taylor developed the infinite waving sheet [111] and filament [112] models with small beating amplitude and established the basic relationship between propulsion and swimming kinematics such as wave speed and amplitude for undulatory swimmers. For large deformation of thin filaments, useful approximations such as resistive force theory and slender body theory are developed. The former relies on anisotropic drag coefficients that are assumed to be *local* to each segment (i.e. no interaction between distant segments). Such theory is accurate in the limit of *exponentially* thin filaments. The slender body theory, however, removes this constraint and requires only thin filaments [113]. The idea is to approximate the flow induced by the filament surface with that induced by a distribution of stokeslets along its centerline [106, 113].

A feature common to these theoretical studies is that the swimming gait is assumed to be fixed and independent of the fluid properties. Yet even in Newtonian fluids, the swimming gait and speed of actual micro-swimmers can by altered by viscosity [114]. The ability to study the effect of fluid rheology on the swimming *gait* of micro-organism has been enabled by advances in modern microscopy. Experiments that directly visualize the contours of the swimming apparatus and the flow field generated by the swimmer become available. For example, the flow streamlines generated by the three representative swimmers are shown in Fig. 2.12(d-f). These experimental methods greatly facilitate the study the effect of fluid rheology on the swimming dynamics of micro-organisms.

In reality, however, biological fluids such as airway mucus, often contain proteins and polymers. These fluids possess rheological properties much more complex than simple Newtonian fluids like water. The next section reviews studies of locomotion in viscoelastic fluids.

2.6.2. Swimming in Viscoelastic Fluids

Understanding the locomotion of micro-swimmers in viscoelastic fluids is motivated by the fact that many fluids encountered in biological processes contain polymers and proteins. Examples include the swimming of spermatozoa in the cervical mucus [115], the mucociliary clearance by the airway epithelial cilia [116, 117], and the penetration of stomach mucus lining of the ulcer-causing bacteria *Helicobacter pylori* [118].

The presence of polymers can profoundly alter swimming at Low Reynolds number. The first example is the breakdown of the scallop theorem due to the history-dependent nonlinear fluid rheology. Even in the limit of a periodic motion executed at the same rate back and forth, the strain-dependent elastic stresses can generate propulsion [119, 120]. The waving sheet model for Oldroyd-B and FENE-P fluids has been derived by Lauga who showed that elasticity consistently hinders motility relative to a Newtonian fluid [121]. This result is consistent with perturbation analysis of infinitely long cylinders using Upper Convected Maxwell model. Numerical simulations with spherical squirmers in Giesekus fluid [122] and experiments with *C. elegans* in long-chain carboxymethyl cellulose polymer into water [123] have also showed that swimming speed is reduced compared to Newtonian counterparts. On the other hand, simulations of finite sized moving filaments [124] and large tail undulations [125] suggest that fluid elasticity can increase the propulsion speed – consistent this time with experiments on rotating mechanical helices [126]. Recently, experimental work on *E. coli* find that the presence of polymers can dramatically increase swimming speed, attributed to suppressed tumbling by viscosity and speed boost by elasticity [114]. Taken together, it becomes clear that there is no universal answer to whether motility is enhanced or hindered by viscoelasticity. Instead, the fluid rheology is strongly coupled to the swimming gait and propulsion strategy of the micro-organism in a complex manner.

Part I

Physical Systems: Flow Instability of Viscoelastic Fluids

CHAPTER 3 : Elastic Turbulence in Channel Flows at Low Reynolds Number

3.1. Introduction: Flow Instabilities of Viscoelastic Fluids

Unlike water, the flow of viscoelastic fluids such as polymeric and surfactant solutions can exhibit flow instabilities even in the absence of inertia, i.e. low Reynolds number (Re) [12, 17, 47, 83–86, 127]. At high flow rates, flows of viscoelastic fluids exhibit a completely new type of chaotic behavior – elastic turbulence – that exists below the dissipation length scale and has no analogues in Newtonian liquids [13, 22, 80, 89]. This elastic flow anomaly has been proposed as a method for efficient mixing in curved pipes at low Re (Fig. 3.1) [22]. Purely elastic instabilities are found in many practical flows and understanding these instabilities is fundamental to our knowledge of the flow in biological fluids (e.g. blood, vesicles, mucus) [128–131], in chemical and polymer industries where flow instabilities have long been plaguing processing [14, 100], and in micro- and nano-fluidics where purely elastic instabilities are proposed as a way of effective mixing at small length scales [22, 132–134].

These flow instabilities result from the development of polymeric elastic stresses in the fluid due to flow-induced changes in polymer conformation in solution. These stresses are strain-dependent, anisotropic, and depend on the nature of the flow [73]. Elastic instabilities are often observed in systems where the mean flow has sufficient curvature, such as the flow between rotating disk [13, 81, 82], between concentric cylinders [12, 80, 83, 84], curved channels [22], and around obstacles [86, 87]. In these systems, high velocity gradients can stretch the polymer molecules and the curved streamlines can generate hoop stresses that destabilize the flow [73]. In fact, it has been argued that curvature is a necessary condition for infinitesimal perturbations to be amplified by the normal stress imbalances in viscoelastic flows [96, 97, 135]. The Pakdel-McKinley criterion for linear instability of viscoelastic fluids states that $\left[\frac{\lambda U}{\mathcal{R}} \frac{N_1}{\tau_{p,s}(\dot{\gamma})}\right]^{1/2} \geq M$, where M is a constant that only depends on the type of flow geometry, U is a typical velocity along the streamlines, $\mathcal{R}$ is the radius of curvature,

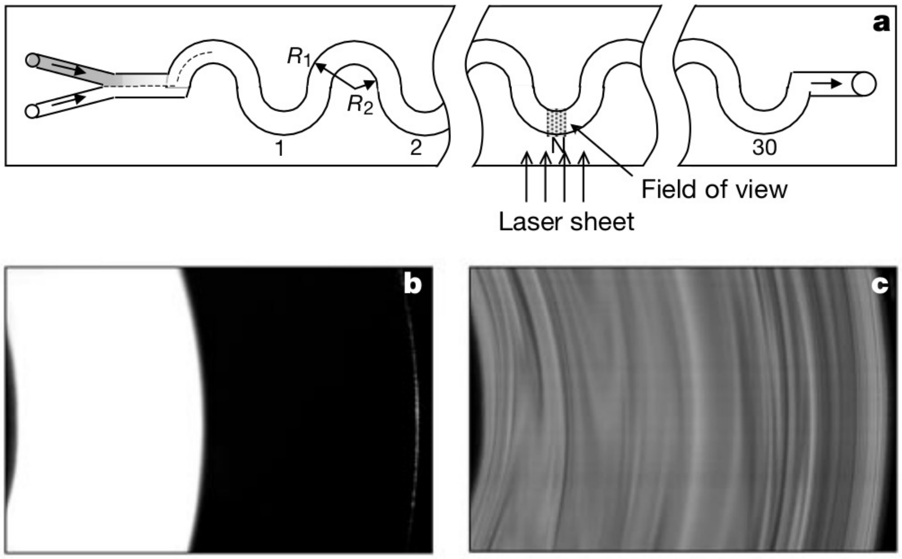

Figure 3.1: Chaotic mixing in curved pipes at low Reynolds number using dilute polymer solutions [22]. (a) Experimental setup and location of the dye visualization, taken at the 29$^{\text{th}}$ bent. Fluorescent dye snapshots showing the mixing structures for (b) Newtonian fluid and (c) polymeric solution in at identical flow rates.

and $\tau_{p,s}(\dot{\gamma})$ is the polymeric shear stress. According to this criterion, purely elastic linear instabilities are not possible in parallel shear flow such as plane Poiseuille flow and pipe flow, and infinitesimal perturbations decay at a rate proportional to $1/\lambda$ [96, 98]. For this reason, much of the work on elastic instabilities and elastic turbulence has been devoted to geometries with curvature [87, 89].

Recent theoretical investigations, however, have shown that viscoelastic flows can be nonlinearly unstable even in parallel shear flows such as in straight pipes and channels at low Re [15, 16, 99, 102, 103]. For example, nonlinear perturbation analysis [15, 16, 99] predicts a subcritical bifurcation from stable base states, while non-modal stability analysis predicts transient growth of perturbation [102, 103]. Subsequent experiments in small pipes [101] found unusually large velocity fluctuations that are activated at many time scales, but the subcritical nature of the instability was not established and no hysteretic behavior (a characteristic of subcritical instabilities) was reported. More recently, the existence of a nonlinear subcritical instability of viscoelastic fluid in a (micro)channel flow was reported in experiments [17]. It is shown that, in the absence of inertia (i.e. low Reynolds number), a finite level of perturbation is required to destabilize the flow and the resultant flow fluctuation is hysteretic [17]. This subcritical transition in viscoelastic channel flows is hence akin to the transition from laminar to turbulent flows of simple Newtonian fluids (e.g. water) in pipes, except that the governing parameter is the Weissenberg number (Wi).

However, the main features of the resulting unstable flow have yet to be well characterized. In particular, is there evidence of "turbulent-like" behavior, namely the presence of irregular flow structures activated at many times scales and a decay law in the flow power spectra in parallel channel flow? If so, how do these features compare with those in geometries with curved streamlines? Moreover, how do the flow resistance and drag evolve following the emergence of such chaotic flow? Finally, is there evidence for the so-called "instability on top an instability" mechanism proposed for the finite amplitude transition of viscoelastic fluids in parallel flows [15, 16]? We will address these questions in this chapter.

3.2. Experimental Setup and Methods

3.2.1. Channel Apparatus

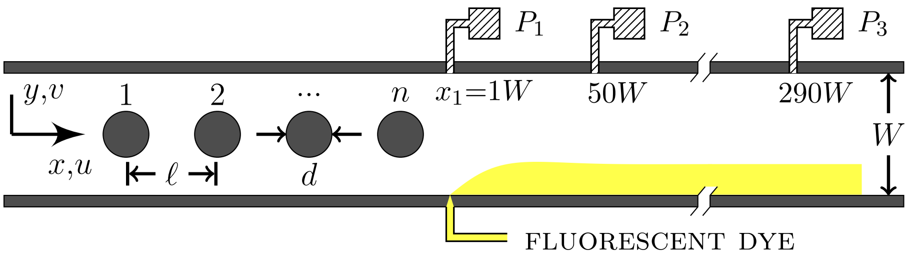

Figure 3.2: Schematic of the experimental channel geometry. A linear array of cylinders is followed by a long parallel shear region. Pressure sensors and dye injection locations are indicated.

The flow of a dilute polymeric solution is investigated using a straight microchannel with a square cross-section of equal width W and depth D ($W = D = 100\,\mu$m). The microchannel is made of polydimethylsiloxane (PDMS) using standard soft-lithography methods [55]. The length of the microchannel is much larger than its width $L/W = 330$, and it is partitioned into two regions. The first region is comprised of a linear array of cylinders that extends for $30W$. A total of 15 cylinders ($n = 15$) is used in the linear array; a schematic is shown in Fig. 3.2. Each cylinder has a diameter d of $0.5W$ and is evenly spaced with a separation of $\ell = 2W$; the last cylinder is at position $x = 0$. The second region follows the initial linear array of cylinders and is a long parallel shear flow that is $300W$ in length. Fluorescent dyes are injected after the cylinders at $x = 1W$ and the patterns are monitored far downstream at $200W$.

To obtain pressure drop measurements in the microchannel, we use pressure sensors (Honeywell TBPDANS compensated/unamplified series) of different ranges (1-30psi). The time response of the sensor is 1ms and the measurement accuracy is 0.15% of the full scale. These sensors are placed in a pitot style arrangement. At specified location on the channel $x_1 = 1W, x_2 = 50W, x_3 = 290W$, we create a short side branch to the main channel that is fully sealed by the glass. At the end of the side branch, a dead-end chamber is formed by inserting the pressure taps. This ensures that no volume flow can enter this branch in steady state. Pressure signals are recorded for over 2 hours with 5 ms resolution. The pressure drop per length between sensor 1 and 2 is $p_1(t) = (P_1 - P_2)/(x_2 - x_1)$ and similarly $p_2(t) = (P_2 - P_3)/(x_3 - x_2)$ for the segment between 2 and 3 (see Fig. 3.2).

3.2.2. Working Fluid and Rheology

The polymeric solution is prepared by adding 300 ppm of polyacrylamide (PAA, 18×10^6 MW) in a viscous Newtonian solvent (90% by weight glycerol aqueous solution); the PAA polymer overlap concentration (c^*) is approximately 350 ppm [136] and c/c^*=0.86. This polymeric solution possesses a nearly constant viscosity of approximately $\eta = 0.30$ Pa·s for $\dot{\gamma} > 10\text{s}^{-1}$ as shown in Fig. 3.3(a). A Newtonian solution, 90% by weight glycerol in water, is also used for comparison. The Reynolds number is kept below 0.01, where $Re = \rho U H/\eta$, U is the mean centerline velocity, H is the channel half width, and ρ is the fluid density. The strength of the elastic stresses compared to viscous stresses is characterized by the Weissenberg number [127], here defined as $\text{Wi}(\dot{\gamma}) = N_1(\dot{\gamma})/2\dot{\gamma}\eta(\dot{\gamma})$, where $\dot{\gamma} = U/H$ is the

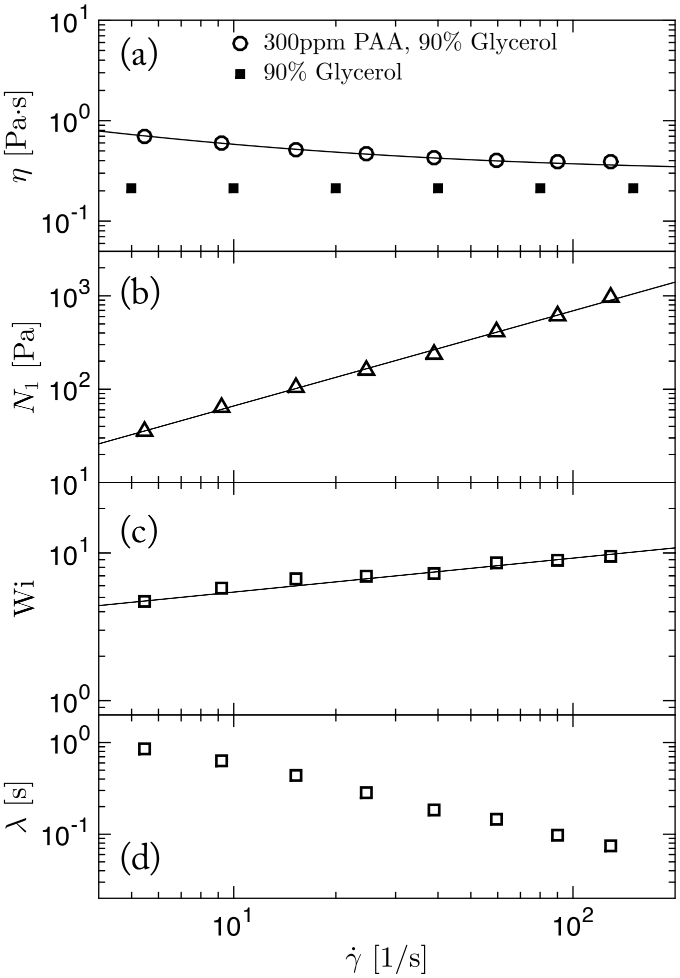

Figure 3.3: Fluid rheological measurements. (a) Shear viscosity $\eta(\dot{\gamma})$ of both Newtonian and viscoelastic fluid and (b) normal stress difference $N_1(\dot{\gamma})$ of viscoelastic fluid as a function of shear rate $(\dot{\gamma})$, measured using a strain-controlled cone-plate rheometer at an ambient temperature of 21°C. Power law fit (line) gives $N_1 = 6.31\,\dot{\gamma}^{1.02}$. (c) The Weissenberg number defined by $\mathrm{Wi}(\dot{\gamma}) = N_1(\dot{\gamma})/\left[2\dot{\gamma}\eta(\dot{\gamma})\right]$ as a function of shear rate, and a power law fit (line) given by $\mathrm{Wi}(\dot{\gamma}) = 3.2\,\dot{\gamma}^{0.23}$. (d) The fluid relaxation time defined by $\lambda(\dot{\gamma}) = N_1(\dot{\gamma})/\left[2\dot{\gamma}^2\eta(\dot{\gamma})\right]$.

shear rate and N_1 is the first normal stress difference. The fluid relaxation time is obtained from shear rheology data, defined as $\lambda(\dot{\gamma}) = N_1(\dot{\gamma})/2\dot{\gamma}^2\eta$; values of λ range from 0.1 to 1.0 seconds for the typical shear rates in the channel experiment. We note that the critical value of Wi for the onset of the subcritical instability in the parallel flow region is $Wi_c \approx 5.2$ for the type of disturbances (15 cylinders) introduced here.

3.2.3. Particle Tracking Velocimetry: Fluorescent and Holographic

The flow velocity is measured using particle tracking velocimetry as described in detail in Section 2.2. For 2-dimensional flow fields, conventional particle tracking using epifluorescent microscopy is used. Spatially-resolved velocity fields are obtained by tracking particles in a rectangular window (width=$0.9W$, length=$1.2W$, centered at $y = 0$) with a grid resolution of ~ 1 μm. The resultant time resolution is $\Delta t = 25$ ms. Time-resolved measurements with smaller window sizes produce velocity time series with high resolution ($\Delta t = 1$ ms) and relatively long sampling duration (up to 300 s).

For high accuracy Lagrangian particle tracking in 3-dimensions, we use holographic particle tracking, as described in Section 2.2. Measurement window of the trajectories is located at $x = 200W$ in the parallel shear region and extends $2.5W$ in the streamwise direction and $0.9W$ spanwise. The uncertainty of estimated particle centroid is around 30 nm for the in-plane (x, y) components and 0.6 μm for the out-of-plane z, at experimental seeding density (10^{-5} volume fraction).

3.3. Results Part A: Signatures of Elastic Turbulence

In this section, we report our results on the flow of a viscoelastic fluid in a parallel shear geometry at low Reynolds number. In particular, as the flow becomes unstable via a subcritical transition, 2-d velocimetry measurements show non-periodic fluctuations over a broad range of frequencies and wavelengths, consistent with the main features of elastic turbulence. Within the same channel system, we compare these flow features to those in the flow around cylinders, located upstream of the parallel shear region; we find significant differences in power spectra scaling, intermittency statistics, and flow structures. A simple mechanism is proposed to explain the sustained velocity fluctuations in parallel shear flows based on polymer stretching and fluctuations in velocity gradients.

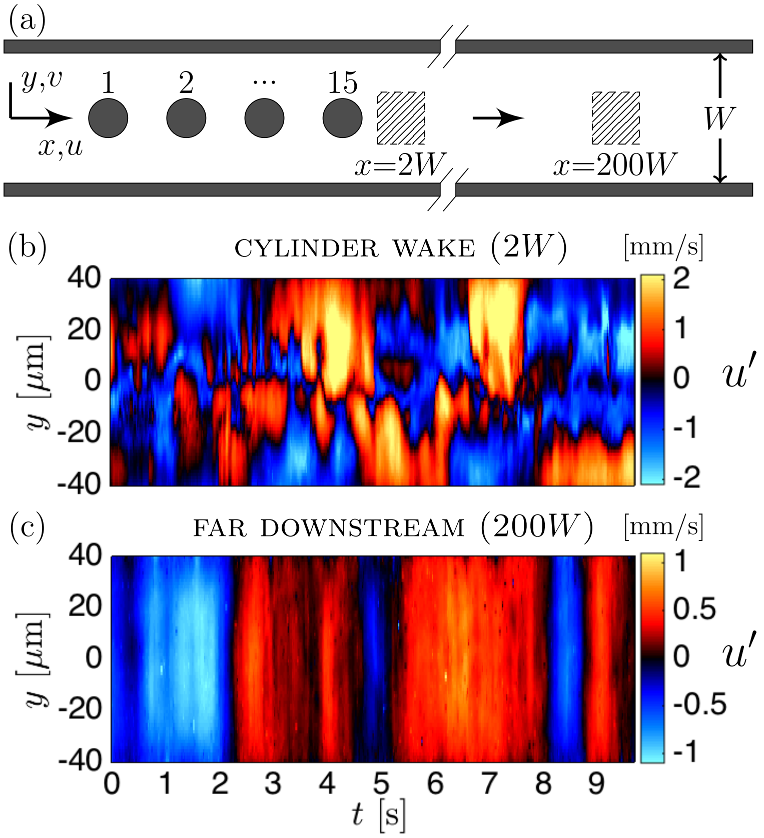

Figure 3.4: (a) Location of the measurement for the space-time plot of streamwise velocity fluctuation for viscoelastic fluids with $n = 15$. (b) Space-time plot of the streamwise velocity fluctuation u', immediately after the last cylinder, $x = 2W$ and $Wi = 10$ and (c) the fluctuation landscape far downstream at $200W$ and $Wi = 10$.

3.3.1. Irregular Flow Structures

We begin our flow analysis by measuring the space-time plot of the streamwise velocity field $u(y,t)$ in the wake of the last cylinder ($x = 2W$) as well as in the parallel shear region ($x = 200W$), as indicated in Fig. 3.4(a). To quantify the streamwise velocity fluctuation u', we subtract the ensemble average $\langle u \rangle$ from the measured signal, $u' = u - \langle u \rangle$. Figure 3.4(b) shows the space-time plot of $u'(y,t)$ along a cutline in the wall-normal direction (y-axis) at the cylinder wake region $x = 2W$ of the channel. Here the spatial coordinate used is the wall-normal y coordinate and the channel centerline is at $y = 0$. Large velocity fluctuation in the cylinder wake is observed, with the amplitude reaching approximately 2 mm/s or 28%

of the fully developed average channel centerline speed (~ 7 mm/s). Along the y direction, we find that high intensity fluctuations are gathered in the form of "spots", which are manifestations of streamwise streaks of high and low local velocity fluctuations. These streaks have a wide range of temporal durations and spatial sizes, as large as the cylinder diameter ($\sim 50\,\mu$m) and as small as the velocity grid spacing ($\sim 1\,\mu$m). Far downstream ($200W$, Fig. 3.4c), however, the flow is significantly different from that in the cylinder wake. We find that velocity fluctuations at $200W$ exist in the form of aperiodic "bursts" of various durations and appear to be spatially smoother in the wall-normal direction. We note that no appreciable fluctuations are found in the Newtonian case under similar conditions. Clearly, there's a markedly different flow structures as the fluid moves from cylinder wake (curved flows) to the parallel shear region.

3.3.2. Temporal Statistics and Velocity Spectra

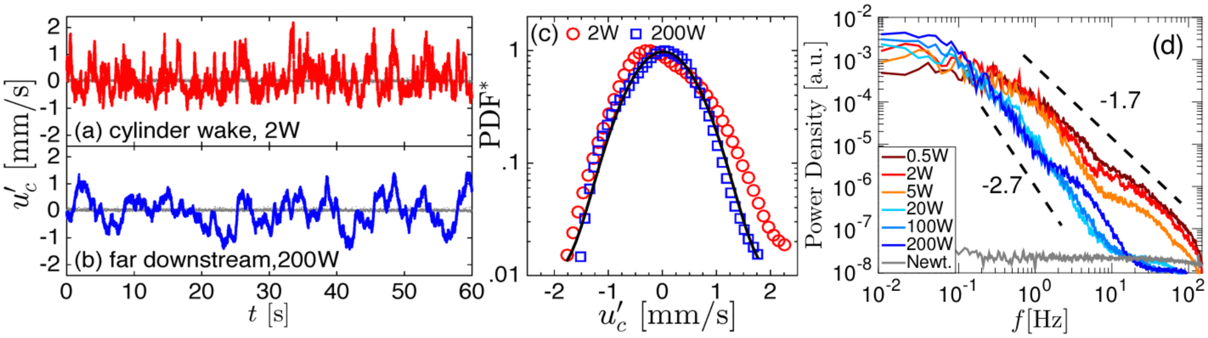

Figure 3.5: Turbulent temporal characteristics of the flow in the cylinder wake and far downstream in the parallel shear region ($Wi = 10$, $n = 15$). (a) Velocity time series measured in the cylinder wake ($x = 2W$). An interval of 60 s is shown out of the total duration of 300 s. (b) Velocity time series measured far downstream in the parallel shear flow region ($200W$) (c) Probability distribution of the associated time series, normalized by the maximum of the probability density. Each curve includes 1.3×10^6 samples. (d) Power spectra of centerline streamwise velocity at various channel positions for $Wi = 10$, $n = 15$

Next, we quantify the temporal characteristics of the unstable flow. The centerline velocity fluctuations $u'_c(t)$ for both Newtonian and polymeric solutions in the wake of the cylinder is shown in Fig. 3.5(a) and in the parallel shear region, Fig. 3.5(b). The data show significant velocity fluctuations for the viscoelastic fluid; the root mean square velocity (i.e. fluctuations) reaches above 10% of the centerline mean, in both regions of the flow. No significant fluctuations are found in the Newtonian fluid case, shown in gray, under the same conditions and flow rates. At both locations, the velocity fluctuations of the polymeric solution appear irregular without apparent periodicity, and the amplitudes of the centerline velocity variations are quite similar. There are, however, differences between the flow in the wake of the cylinder ($2W$) and in the parallel shear region ($200W$). Specifically, the mean of $u_c'(t)$ at the cylinder wake is negatively biased towards the low velocity values, with sporadic excursions to high values. Physically, this means the flow at $2W$ is characterized by intermittent jumps to high velocities amidst dwelling at lower velocities. Far downstream ($200W$), on the other hand, the flow seems to fluctuate around the mean evenly.

These contrasts in the velocity fluctuations between these two locations are further reflected in the normalized probability distribution of $u_c'(t)$, shown in Fig. 3.5(c). In the cylinder wake, we find that the mode of the distribution has a negative bias towards lower velocity, and a pronounced tail towards high velocities, consistent with Fig. 3.5(a). In the parallel shear region, on the other hand, the distribution is unskewed and is in fact well captured by a Gaussian distribution (solid line). Consequently, the skewness of the distribution is 0.41 at $2W$, compared to the much lower 0.06 at $200W$. We believe that near the cylinder ($2W$), the observed aperiodic jumps in $u_c'(t)$ are associated with the sudden release of elastic energy by polymer molecules into the flow (analogous to the intermittently injection of elastic energy in curved systems [82, 137]). Far downstream ($200W$), on the other hand, the even likelihood of velocity above and below the mean value indicates an unbiased energy transfer back and forth between the polymer and the flow.

Next, we analyze the velocity fluctuations in the frequency domain by computing the Fourier transform of $u_c'(t)$. Figure 3.5(d) shows the power spectra for $n = 15$ and $Wi = 10$. We find that the viscoelastic fluid flow is excited at a broad range of frequencies f at all measured channel locations ($2W$ to $200W$), compared to the Newtonian control at the highest flow rates. This feature is one of the main hallmarks of elastic turbulence, previously observed in curved geometries [13]. Figure 3.5(d) also shows a gradual decay law in the power spectrum in the cylinder wake, following $f^{-1.7}$. As the flow moves downstream from the array of cylinders into the parallel shear flow region, however, we observe clear developments in the frequency spectra. We find that, in a few channel widths after the last cylinder, the energy decreases in the high frequency range (10-100 Hz), which corresponds to the periodic perturbation introduced by the cylinders. At $x = 20W$, the decrease in high frequency fluctuations intensifies across two frequency decades. On the other hand, the power in the low frequency range (0.01-0.1 Hz) of the spectrum increases. The combined result is that, after $20W$, velocity fluctuations are increasingly dominated by low frequency variations and the power law decay becomes steeper, following $f^{-2.7}$. This suggests that the energy contained in the high frequency range near the cylinders seems to shift toward the low frequency range in the parallel shear region.

3.3.3. Energy Consideration and Polymer Stretching

To test this idea of energy transfer rather than simple viscous dissipation, we compute the summed power over the dominant frequency range (0.01-100 Hz). This is equivalent to the standard deviation of the time series if all valid frequencies are used. We perform this analysis for flows above and below the onset of the subcritical instability in the parallel shear region ($Wi_c = 5$ for n =15). Fig. 3.6(a) shows the evolution of the total energy down the channel for $Wi = 4 (< Wi_c)$ and $Wi = 10$ $(> Wi_c)$. Note that $n = 15$ is used for both cases. For the $Wi = 4$ case, where the flow rate is not energetic enough to trigger velocity fluctuations downstream in the parallel shear flow, we find a sharp decay of total power by two orders of magnitude. The $Wi = 10$ case sees a weak initial decay in total power within the first $20W$. However, after $x = 20W$, the trend reverses and follows a steady increase downstream into the parallel shear flow region, despite the dissipative environment ($Re \sim 10^{-3}$). A zoom-in of the unstable case is shown in the inset and clearly displays such trend. Such persistence of fluctuation energy suggests a self-sustaining mechanism that we try to elucidate below.

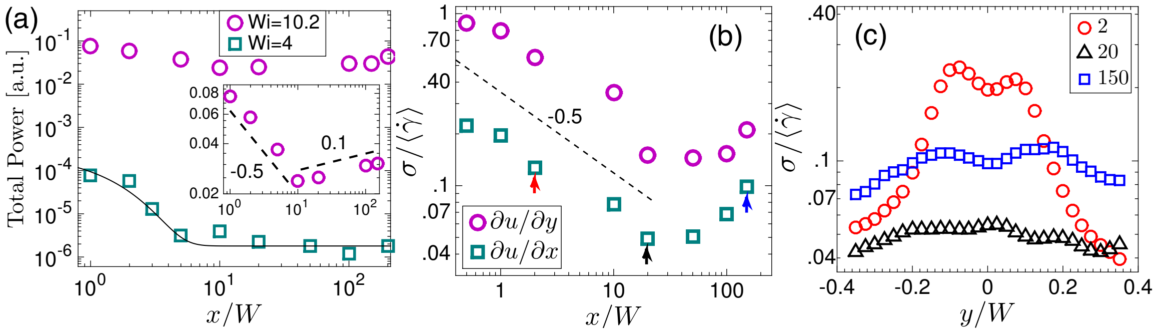

Figure 3.6: (a) Sum of total power from (0.01 Hz $\leq f \leq$ 100 Hz) versus channel position x/W. The solid line is the best fit exponential decay. Inset: zoom-in for the $Wi = 10.2$ case. (b) The rms variation σ of shear $\partial u/\partial y$ and extensional $\partial u/\partial x$ components of the velocity gradient, normalized by the spatial mean shear rate $\langle\dot{\gamma}\rangle$ in the parallel shear flow. (c) Extensional component of the rms profile across channel width y immediately in the cylinder wake ($2W$), at the end of the cylinder flow decay ($20W$), and far downstream in the parallel shear flow region ($150W$).

So far we have shown that the flow of a polymeric fluid in a parallel shear geometry can sustain relatively large velocity fluctuations in both space and time even at low Re. These velocity fluctuations, far downstream from the initial perturbation, are most likely driven by the stretching of polymer molecules in the flow. To test this hypothesis, we measure the root mean square (rms) variation of the shearing ($\partial u/\partial y$) and elongational ($\partial u/\partial x$) components of the velocity gradient; here the rms of quantity A is defined as $\sigma = \langle(A - \langle A\rangle)^2\rangle^{1/2}$, similar to [138]. These components (quantities) are known to mediate polymer stretching in random flows [138–141].

Figure 3.6(b) shows the rms variation σ of $\partial u/\partial y$ and $\partial u/\partial x$ at various positions along the channel normalized by the spatial average shear rate $\langle\dot{\gamma}\rangle$ downstream in the parallel shear flow. Near the linear array of cylinders, we find significant fluctuations of the velocity gradients relative to the mean shear rate in the parallel shear flow. Moreover, the $\partial u/\partial y$ component dominates $\partial u/\partial x$ and both components decay as the polymeric solution flows downstream. These trends persist down to approximately $20W$ in the channel. However, at $x \gtrsim 20W$, we find that both components of $\sigma/\langle\dot{\gamma}\rangle$ reverse trend and begin to increase as the fluid flows downstream. Concurrently, we observe that the fluctuation in the elongation component become increasingly comparable to that of the shear component. These trends clearly show a change in flow at or around $20W$ accompanied by an increase in velocity fluctuations and polymer stretching. This non-monotonic trend is also captured by plotting the spatial profile of $\sigma/\langle\dot{\gamma}\rangle$ for $\partial u/\partial x$ across the channel width (y-axis) for three different channel locations, shown in Fig. 3.6(c). The data suggest that polymer molecules are increasingly stretched by flow gradient in the streamwise direction beyond $20W$.

To further demonstrate the magnitude of the fluctuation in velocity gradients is large enough to generate polymer stretching, we compute a Weissenberg number based on fluctuations in the velocity gradients. Here, $\mathrm{Wi}^{s}_{rms} = \lambda(\dot{\gamma}) \cdot \sigma(\partial u/\partial y)$ where the rms fluctuation of the shear gradient is non-dimensionalized by the polymer relaxation time. Using the relaxation time corresponding to Wi=10.2, we find that $\mathrm{Wi}^{s}_{rms} \sim 5.2$ in the cylinder wake ($x = 2W$), while far downstream, it is approximately 2. Moreover, far downstream, the Weissenberg number based on the rms of elongational $\mathrm{Wi}^{e}_{rms} \sim 1$. We note that the values of both Wi^{s}_{rms} and Wi^{e}_{rms} are near or larger than 1, which suggest that the flow is able to generate sufficient polymer stretching [43, 95].

3.4. Results Part B: Law of Resistance and Coherent Structures

In this section, we continue to investigate the flow of polymeric solutions in straight channels at low Reynolds number using pressure measurements and high-resolution particle tracking. The law of flow resistance is established by measuring the flow friction factor f_η versus flow rate. Two regimes are found: a transitional regime marked by rapid increase in drag, and a turbulent-like regime characterized by a sudden decrease in drag and a weak dependence on flow rate. Lagrangian trajectories show finite transverse modulations not seen in Newtonian fluids. These curvature perturbations far downstream are found to generate sufficient hoop stresses to sustain the flow instabilities in the parallel shear flow.

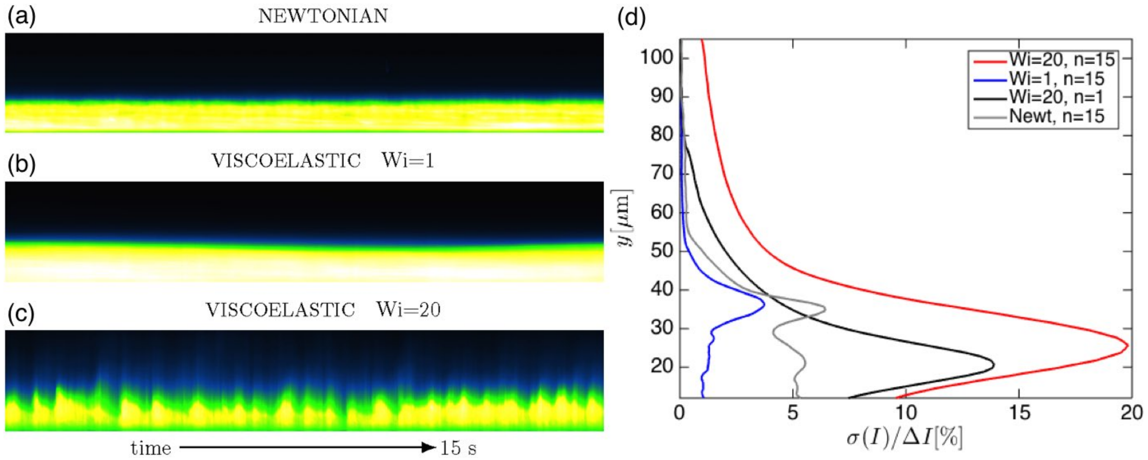

Figure 3.7: Dye injection and mixing downstream in the parallel shear region. (a-c) Space time graph of the dye stream. (d) Channel profile rms fluctuation of the dye intensity, normalized by the intensity difference of the two streams.

3.4.1. Chaotic Mixing

To further reveal the flow structure, we begin by investigating the flow patterns formed when a stream of fluorescent dye is injected one channel width $(1W)$ after the last post. The dye spreading and patterns are then visualized far downstream in the parallel shear region, 200 channel widths downstream from the last post $(x = 200W)$. Figure 3.7 show the spatio-temporal profile of the dye intensity along the device's cross section (y) for various flow rates of Newtonian and viscoelastic fluids for 15 posts $(n = 15)$. For the Newtonian case Fig. 3.7(a) and the viscoelastic flow below the onset of subcritical instability $Wi = 1$ Fig. 3.7(b), the profile shows typical laminar dye layer with minimal penetration into the undyed stream, except for diffusion. (Similar behavior is observed with viscoelastic fluids for the $n = 0$ case.) However, a different dye pattern is observed once the flow becomes unstable for the Wi=20, $n = 15$, shown in Fig. 3.7(c). We find highly irregular flow patterns with spikes of dye penetration into the undyed fluid stream. These mixing layer profiles along the channel width are quantified in Fig. 3.7(d), where root-mean-square intensity fluctuations, as normalized by the mean intensity difference between the two dye streams, are shown. The flow in the elastic turbulent regime, $Wi = 20, n = 15$ has both a high level of fluctuations and a deeper penetration into the undyed stream. The observed fluctuations in time suggest the presence of velocity modulations in space. Indeed, we will soon show that particle trajectories do exhibit wavy and coherent motions in the parallel shear region.

3.4.2. Law of Resistance in Pipe Flow of Viscoelastic fluids

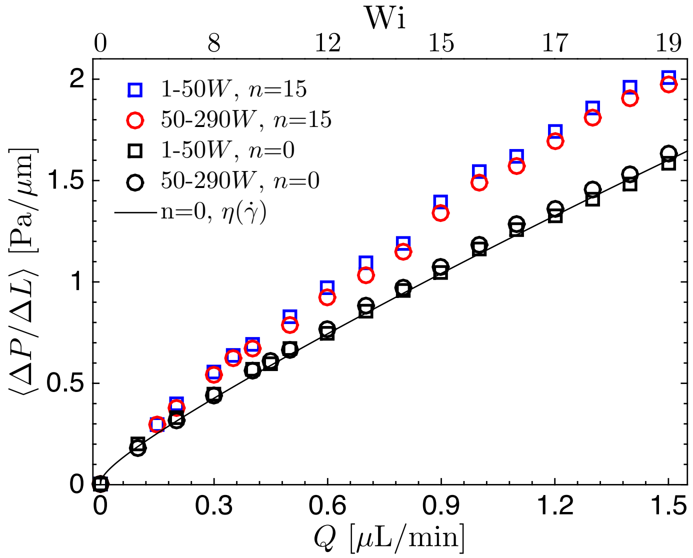

Figure 3.8: Flow resistance as measured by mean pressure drop per length, as a function of flow rate and Wi for unstable $n = 15$ case and the stable $n = 0$ case. Solid line represents estimation using wall shear rates and viscosity values from fluid rheology.

As mentioned before, little is known about elastic turbulence in channel flows. Importantly, there is no known law of resistance for such flows. Here, we propose a new law of friction for polymeric solutions in channel and pipe flows. Pressure drop is measured along the parallel shear region using sensors that are placed at three locations, $x_1 = 1W, x_2 = 50W, x_3 = 290W$. The pressure drop per length signals p_1, p_2 are recorded for approximately 10^4 seconds (with 5 ms resolution). Figure 3.8 shows the mean pressure drop values for viscoelastic fluids for $n = 0$ and $n = 15$ cases as a function of flow rate Q and Wi. We note that the statistical mean of the reported signals measure the aggregate flow resistance encountered to sustain a constant mass flow rate. As expected, the pressure drop or flow resistance increases with flow rate and Wi. The pressure drop for the $n = 0$ case slightly deviates from the Newtonian case (i.e. $\triangle P \propto Q$) due to mild shear-thinning in fluid viscosity. These effects can be accounted for by estimating the pressure drop using wall shear rate and corresponding viscosity $\eta(\dot{\gamma})$ measured using a cone-and-plate rheometer, as shown by the solid line in Fig. 3.8. No significant difference is found between p_1 and p_2 for $n = 0$ case as expected, since entrance effect is carefully minimized using tapered inlet and generates minor disturbance relative to that of the cylinder array. For $n = 15$, we find a clear increase in pressure drop relative to the $n = 0$ case; the two pressure segments p_1 and p_2 show little to no difference. This increase in flow resistance cannot be explained by solely shear-thinning effects and is related to the development of additional elastic stresses in the flow as the Wi is increased. It also indicates that more energy is necessary to keep the same flow rate compared to a stable viscoelastic channel.

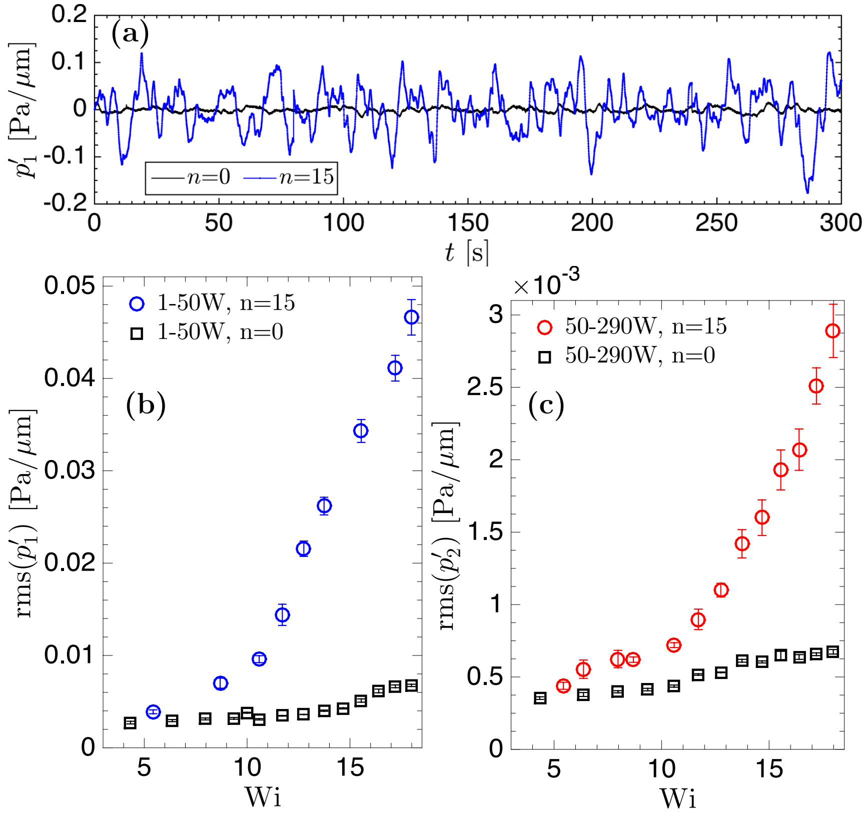

Figure 3.9: Pressure fluctuations in the parallel shear region. (a) Pressure gradient fluctuations for $p_1'(t)$ between $x = 1W$ and $50W$ for n=15 case, compared with the unperturbed n=0 case, $Wi = 18$. (b,c) Root-mean-square (rms) of the pressure gradient fluctuations as a function of Wi for $n = 0$ versus $n = 15$, (b) p_1' and (c) p_2'.

The increase in flow resistance is closely associated with the onset pressure fluctuations. Figure 3.9(a) shows sample time records of pressure fluctuations $p_1'(t)$ for viscoelastic fluids at $Wi = 18$ in devices with $n = 0$ (black line) and $n = 15$ (blue line). We clearly observe an increase in the pressure fluctuations once cylinders are introduced in the flow. Figure 3.9(a) and 3.9(b) show root-mean-square (rms) values of the pressure fluctuations of the p_1' and p_2' segments, respectively, as a function of Wi for the $n = 15$ and $n = 0$ cases. For the $n = 0$ case, pressure fluctuations remain relatively small and steady, nearly independent of Wi; the small increase in pressure fluctuation at the higher values of Wi may be due to entrance effects. We find that for both segments, p_1' and p_2', the rms values show significant departure from the stable $n = 0$ case and a marked increased with increasing Wi. The values of the rms(p_1') and rms(p_2') start to depart from the $n = 0$ trend at $Wi \approx 5$ and grows weakly until $Wi \approx 9$. This is followed by a much steeper growth for $Wi \gtrsim 9$. This trend in pressure fluctuation measurements agrees relatively well with measurements of velocity fluctuations which established that the linear instability associated with the flow around the upstream cylinders occurs at $Wi \approx 4$ and the onset of subcritical instability occurs at $Wi \approx 9$ [17,61].

Since pressure data is now available, one can investigate the law of (flow) resistance for viscoelastic channel flows as a function of Wi. This is analogous to measuring the Darcy friction factor for Newtonian pipe flows as a function of Re [11]. Traditionally, the friction factor f is defined as $(\Delta P/\Delta L)/(\rho U^2/2W)$, where W is the channel width and U is the fluid mean velocity. As long as variations are small (e.g. smooth pipes), the friction factor f is solely a function of Re such that $f = f(Re)$. In what follows, we proposed an analogous law of resistance for viscoelastic channel flows as a function of Wi. As noted earlier, the values of Re in our experiments are quite small ($Re \lesssim 10^{-3}$). Since fluid inertia is negligible, we propose to scale the pressure drop by the fluid shear stresses across the channel and define a viscous friction factor f_η as $[(\Delta P/\Delta L)/(c\eta_w\dot{\gamma}_w/W)]$, where $\dot{\gamma}_w$ is the wall shear-rate, η_w is the corresponding viscosity and c is a geometry factor (4.06 for square duct and 4 for circular pipe).

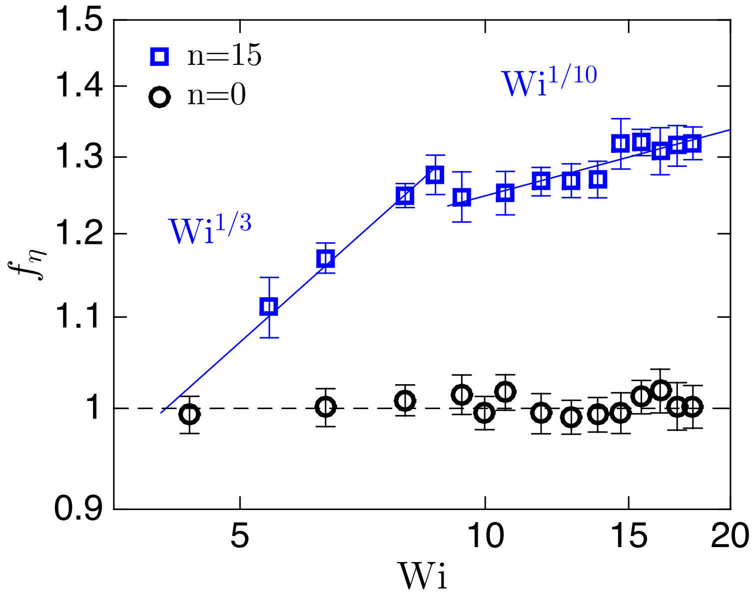

Figure 3.10: Viscous wall friction factor f_η (definition see text) as a function of Wi for $n = 0$ and $n = 15$.

Figure 3.10 shows the values of f_η as a function of Wi for polymeric solutions in channels with $n = 0$ and $n = 15$. For $n = 0$, we find that the f_η is independent of Wi indicating that flow resistance is purely governed for by viscous effects, which are well accounted for by the normalization. For $n = 15$, on the other hand, we observe an increase in flow resistance f_η as Wi is increased and find that $f_\eta \sim Wi^{1/3}$ up to $Wi \approx 9$. Surprisingly, we find a second regime for $Wi \gtrsim 9$ in which a sudden decrease in f_η is observed followed by a weak dependence on Wi. This relative decrease in drag or friction seems to suggest the emergence of a new flow state which has yet to be explored in detail. The data shown in Fig. 4 also suggests that the initial $f_\eta \sim Wi^{1/3}$ regime is associate with a transitional flow that is then followed by a turbulent-like state. Similar to Newtonian pipe flows, there is an initial increase in drag followed by a sudden decrease once the flow becomes turbulent.

3.4.3. Coherent States and Mechanism of Finite Amplitude Transition

Next, we investigate the structure of the viscoelastic flow for n=15 and Wi=18; this is the regime in which we expect flow instabilities but quantifying the presence of flow structures has been difficult due to the weak spanwise velocity component relative to the mean shear

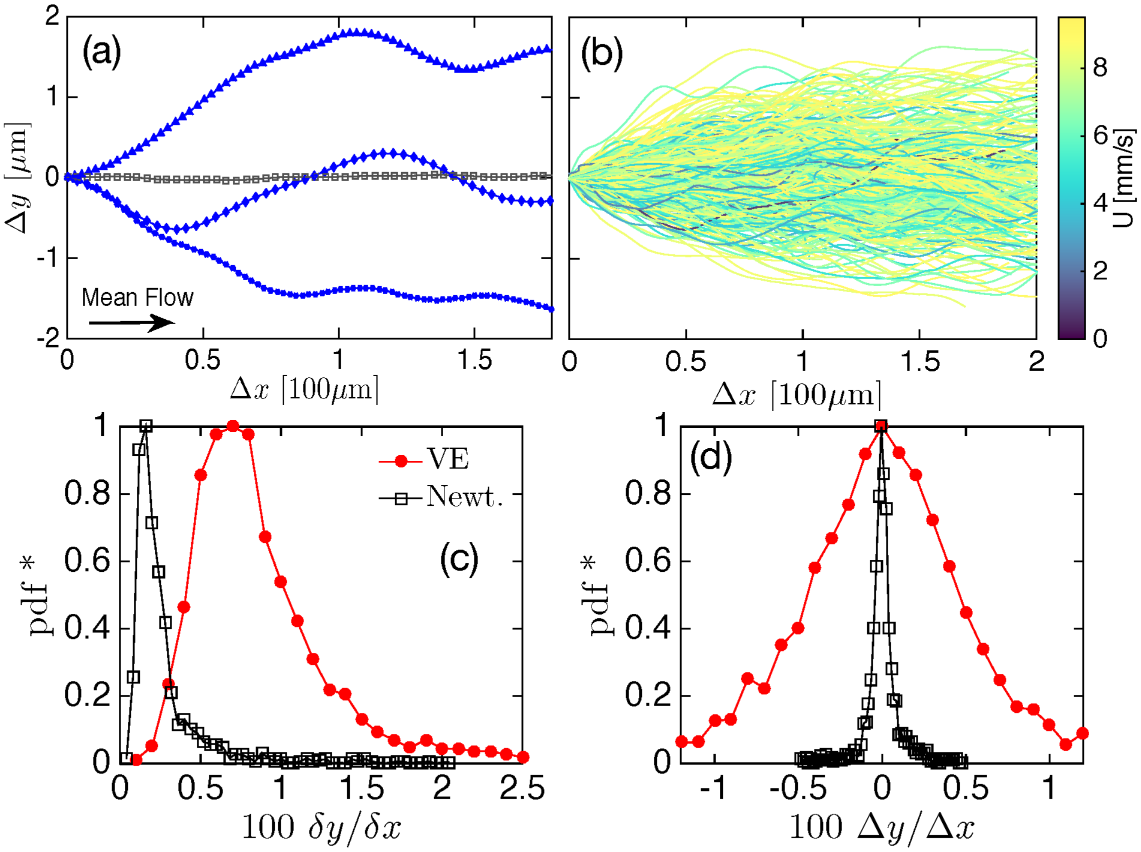

Figure 3.11: Lagrangian trajectories and statistics. (a) Trajectories in the x (streamwise) and y (spanwise) direction; blue curves represent the n=15 viscoelastic case at $Wi = 18$ and the gray curve represents Newtonian case at identical flow rate. (b) Collection of 2000 trajectories colored by streamwise speed. (c,d) Normalized probability distribution of the trajectory averaged ratio of the transverse versus streamwise components for (c) cumulative and (d) end-to-end displacement.

[61]. Here, we use a 3-dimensional holographic particle tracking method. As described by Section 2.2, the resolution of our method is 30 nm in the x, y imaging plane and 0.6 μm out of the plane in z. The measurement window of the trajectories is located at $x = 200W$ in the parallel shear region and extends $2.5W$ in the streamwise direction and $0.9W$ spanwise.

Figure 3.11(a) shows sample particle trajectories for the Newtonian (grey symbols) and viscoelastic (blue symbols) fluids for the $n = 15$ case at $Wi = 18$. While the particle trajectory in the Newtonian case is fairly rectilinear (following the mean flow direction) with little to no lateral movement, particle trajectories in the viscoelastic fluid case display a relatively pronounced waviness and lateral movement. This is not isolated to a few particles and Fig. 3.11(b) shows the full extent of the spanwise spread of the Lagrangian trajectories for approximately 2000 trajectories. Such wavy structures underlies the irregular dye transport patterns seen in Fig. 3.7(c). We quantify these deviations from the base-flow by plotting the probability distribution functions (pdf) of the ratio between the transverse and streamwise components of the particles cumulative displacement (Fig. 3.11c) and end-to-end displacement (Fig. 3.11d) for Newtonian and viscoelastic fluids. We define the ratio of cummulative displacement for each observed trajectory by $\delta y/\delta x = \sum |dy_i|/\sum |dx_i|$ over the duration of observation for that trajectory; the ratio of end-to-end displacement is $\Delta y/\Delta x = \sum dy_i/\sum dx_i$. Here dy_i and dx_i are the x, y displacements of a single trajectory between consecutive frames.

The Newtonian data (black symbols) represent mostly the measurement noise level. Results show that particles in the viscoelastic fluid exhibit small but finite values of transverse (spanwise) velocity and a broader distribution of individual particle end-to-end displacement. These results indicate the presence of subtle flow structures in viscoelastic fluids in parallel shear flows. Specifically, the mean of the ratio of cumulative displacements is 1.3% and the rms of the ratio of end-to-end displacements is 3.8% for the viscoelastic case. These modulations are significantly higher than the 0.3% and 0.6% for Newtonian fluids at identical flow rates. These deviations from the base-flow are small in absolute terms (1-2% of the streamwise component), but in viscoelastic flows even small deviations in the velocity fields can represent large increase in elastic stresses in the flow due to the nonlinear relationship between stress and velocity [142, 143].

Are these curved particle trajectories enough to drive flow instabilities far downstream ($200W$)? A key measure is the streamline curvature of the particle pathlines. In Fig. 3.12, we show the distribution of trajectory curvatures obtained from particle trajectory data shown in Fig. 3.7 ($Wi = 18$, $n = 15$). We see that the viscoelastic flow generated significantly higher curvature than the Newtonian case. The mean curvature is 0.024 rad/μm, which is

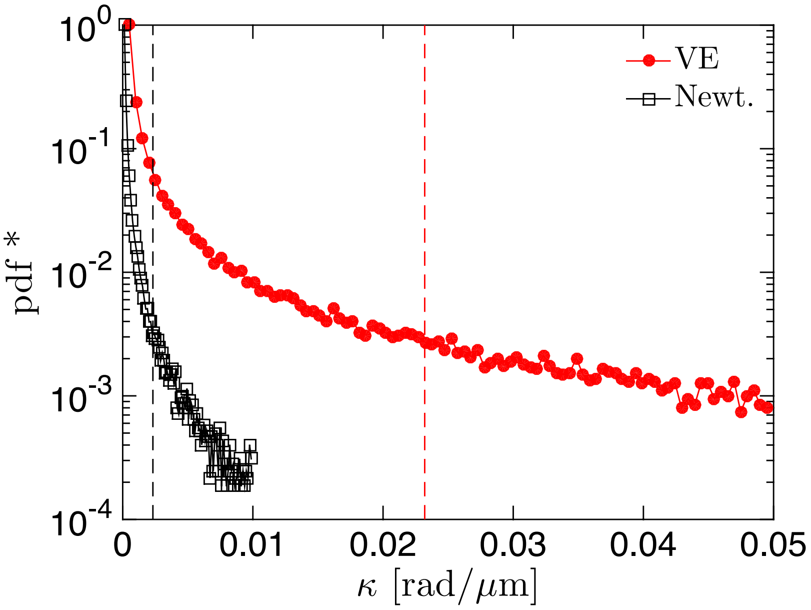

Figure 3.12: Sampled curvature distribution of trajectories at $Wi = 18$ for viscoelastic fluid at $n = 15$ and the Newtonian fluid at comparable flow rate. The dashed colored lines are the population mean.

an order of magnitude larger than the Newtonian and gives a mean radius of curvature of $\mathcal{R} = 43$ μm for the particle pathlines. Using N_1 data (see Fig. 3.3 b), we can compute the Pakdel-McKinley condition defined as $[(\lambda U/\mathcal{R})(N_1/\tau_{p,s})]^{1/2}$ [96] and described in Sec. 2.5.2. We find a value of approximately 7, which is sufficiently large to trigger flow instabilities. Similarly, we find that hoop stresses $N_1/\mathcal{R} = 8$ Pa/μm can be of the same order (or higher) than pressure drop $\Delta P/\Delta L = 2$ Pa/μm. These particle trajectories have enough curvature and speed to generate hoop stresses that can sustain flow instabilities. Our results provide strong evidence for the "instability upon an instability" mechanism proposed for the finite amplitude transition of viscoelastic fluids in parallel flows [15, 16].

3.5. Summary

First, using high speed velocimetry, we have found evidence for turbulent-like flow behavior in a parallel shear geometry of a viscoelastic fluid, namely the presence of irregular flow structures activated at many times scales and a decay law in the flow power spectra. Further, these features, including power spectra scaling, intermittency statistics, and flow space-time structures are distinct from with those near the curved cylinders in the same system. Specifically, we find that the flow near cylinders is organized by streamwise streaks that manifest as "spots" that is highly intermittent in time, while temporal burst that manifest as spanwise bands are found in the parallel shear region. Moreover, the energy contained in the high frequency range near the cylinders seems to shift toward the low frequency range in the parallel shear region. These results suggest the emergence of a new type of elastic turbulent state in parallel shear flows. The details of this investigation are published in [61].

Second, we establish the law of resistance and the coherent structures organizing the elastic turbulence in channel flows. Pressure measurements are used to establish flow resistance. We find two regimes: (i) a transitional regime ($5 \lesssim Wi \lesssim 9$) in which the (viscous) friction factor $f_\eta \sim Wi^{1/3}$, and (ii) a turbulent-like regime ($Wi \lesssim 9$) in which a sudden reduction of f_η is observed followed by a weaker dependence on flow rate that leads to $f_\eta \sim Wi^{1/10}$. This behavior is analogous to Newtonian pipe flows in which a sudden increase in drag is followed by a weaker dependence on Re. Dye and particle tracking data show the presence of weak flow structures far downstream in the parallel shear region ($200W$). In particular, we find small but finite particle lateral (spanwise) movement and transverse modulations relative to the Newtonian case (Fig. 5). These particle trajectories have enough curvature and speed to generate hoop stresses that can sustain flow instabilities. Our results provide strong evidence for the "instability upon an instability" mechanism proposed for the finite amplitude transition of viscoelastic fluids in parallel flows [15, 16] and provide new insights into the flow of polymeric solutions in channels and pipes. Even small perturbations in the velocity field can lead to significant changes in pressure drop and drag.

CHAPTER 4 : Upstream Vortex and Instability of the Viscoelastic Flow around a Confined Cylinder

4.1. Introduction: Flow Around Cylinders and Elastic Waves

The creeping flow of complex fluids, in particular polymeric solutions, in porous media is important to an array of technologies, such as polymer processing, filtration, flow in soil, and oil extraction [144]. Natural porous media often consist of sand grains, clays, and shales that, under the forces of nature, forms intricate microscale geometries and complex flow patterns, such as converging-diverging flows with strong shear and extension [145].

The flow around confined cylinders, however, is a much simpler geometry that has long been used as a benchmark system for non-Newtonian flows. The basic geometric elements of flow around cylinder represent a fundamental example of flow past obstacles and blockages such as those encountered in porous flow. The flow here is characterized by strong extension from the stagnation points both upstream and downstream of the cylinder and strong shear around the cylinder generated under the confinement of the channel walls. Indeed, the study of elastic flow instability around cylinder arrays has been used extensively as a model for the viscoelastic flow in porous media [146, 147].

More recently, microfluidic channels with multiple posts have been used in a number of studies of viscoelastic instabilities at low Reynolds number [148–151]. The microposts provide a perturbation to the fluid streamlines that can initiate viscoelastic instabilities above a critical condition [96]. Most experimental and numerical investigations have observed a wake region form downstream of the cylinder [87, 127]. The wake instability forms at a critical Deborah number at which point normal stresses along curved streamlines distort the flow.

Existing literatures on upstream instability, on the other hand, focus on contraction type geometry. The vortex development in the classic contraction geometry has been well studied by many authors where the lip and corner vortices emerge, grow and become unstable [45,46,152–155] for a range of contraction ratios and polymeric solutions including long chain polymers, DNA, and surfactant systems. The onset of upstream vortex in the viscoelastic flow through a 90-degree bend has been studied by Muller et al [156–158].

However, the development and characteristics of elastic instabilities upstream of an obstacle such as a cylinder are not well understood. The micropost differs from the planar constriction because the centerline of the upstream flow, where the velocity is maximum, reaches a stagnation point in the front of the micropost. The velocity field has strong extensional components in both the axis of the cylinder and the cross stream direction. Existing experimental results have shown a possible upstream instability [149]. The coupling of upstream instabilities and downstream wakes has been hypothesized to drive this complex flow [149, 159]. The flow can also be highly three dimensional, as shown by numerical studies [160]. Yet the dynamical transition and three-dimensional structure of the vortex is not fully resolved experimentally. Here, we report three main discoveries of the elastic instability upstream of a single cylinder in confined channel flow. First, we report the onset of upstream instability in the form of corner vortices in front of the cylinders whose size grows with increasing flow rate. Second, beyond a critical flow rate, the vortex becomes unsteady and switches between two bi-stable configurations that leads to symmetry breaking perpendicular to the cylinder axis and is highly 3-dimensional in nature. Lastly, we show that the disturbance of the elastic instability propagates far upstream in the form of an elastic wave, yet remains relatively isolated from the flow in the cylinder wake. The elastic wave speed is found to increases with Weissenberg number.

4.2. Experimental Methods

The flow of a dilute polymeric solution is investigated using a straight microchannel made from PDMS with a rectangular cross section with width $W = 100\,\mu$m and height $D = 60\,\mu$m. A single cylindrical post with diameter $d = 50\,\mu$m is located far ($300W$) from the inlet and is centered in the channel width direction. The device schematic is shown in Fig. 4.1 (a).

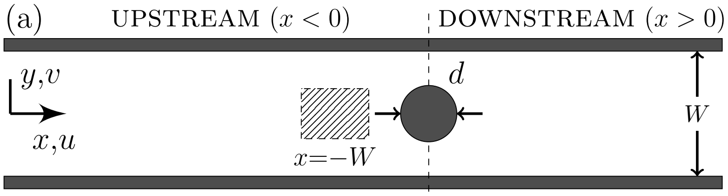

UPSTREAM UNSTEADY VORTEX

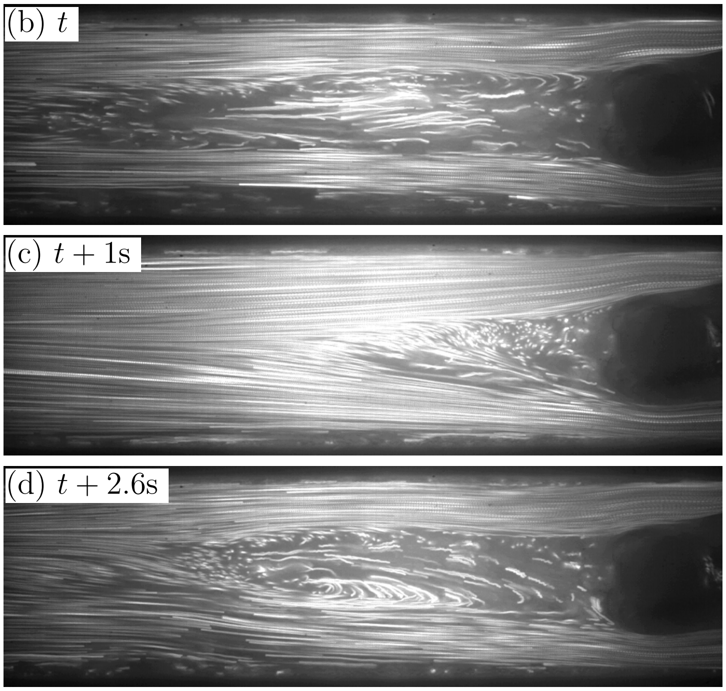

Figure 4.1: (a) Schematic of the experimental setup. (b-d) Three snapshots of the streak plots showing the unsteady vortex upstream of the cylinder.

The level of confinement can be defined as $\alpha = D/W = 0.6$ and blockage $\beta = d/W = 0.5$. Fluid flow is delivered with a constant flow rate from a syringe pump (Harvard apparatus PHD 22/2000).

The viscoelastic fluid is a polymeric solution made by mixing 300 ppm of polyacrylamide (PAA, MW 18×10^6) in a 90 wt.% glycerol aqueous mixture. The polymeric solution has a nearly constant viscosity of η =0.300 Pa.s as a function of shear rate. The Weissenberg number is defined from the strength of elastic stress to viscous stresses as $Wi(\dot{\gamma}) = N_1(\dot{\gamma})/2\dot{\gamma}\eta(\dot{\gamma})$ where U/H is the shear characteristic shear rate and N_1 is the first normal stress difference. The fluid is seeded with less than 0.01% by volume of 1 μm polystyrene microspheres.

Steady shear rheology is conducted using cone-and-plate rheometer (Bohlin Gemini) and shown in previous sections in Fig. 3.3.

We visualize the channel using both particle streak velocimetry for 2-d imaging and in-line holographic microscopy for 3-d images, as described in detail in Section 2.2.

4.3. Results and Discussion

We report three main discoveries of the elastic instability upstream of a single cylinder in confined channel flow. First, we observe the onset of upstream instability in the form of corner vortices in front of the cylinders whose size grows with increasing flow rate. Second, beyond a critical flow rate, the vortex becomes unsteady and switches between two bi-stable configurations that leads to symmetry breaking perpendicular to the cylinder axis and is highly 3-dimensional in nature. Lastly, we show that the disturbance of the elastic instability propagates far upstream in the form of an elastic wave, yet remains relatively isolated from the flow in the cylinder wake. The elastic wave speed is found to increases with Weissenberg number.

4.3.1. Upstream Vortex: Growth, Fluctuation, and Pulsing

We begin with two-dimensional streak plots showing the highly unsteady vortices immediately upstream of the cylinder. In Fig. 4.1(b,c) we show two snapshots of streaks taken at $z = 10\mu$m (from bottom plane) of the channel for $Wi = 23$. We observe the presence of a large recirculation region in front of the post which clearly separates the dominant bulk flow into two streams. To quantify the onset of the upstream vortex, we monitor its length χ normalized by the cylinder diameter d as a function of Weissenberg number at a particular height ($z = 10\mu$m). The length is defined as furthest upstream point with zero or negative to the edge of the cylinder. This stagnant vortex extends far upstream with maximum normalized vortex length of about $\chi/d \sim 6$ as in Fig. 4.1(b). The feature of the vortex is marked by flow recirculation with relatively low or negative velocity compared to the bulk flow. At Wi=23, the vortex is highly unsteady and frequently collapses (Fig. 4.1c) and regenerates in time (Fig. 4.1d).

To quantify the onset of the stagnant vortex, we track the non-dimensional vortex length as a function of Weissenberg number at a particular position ($z = 10\mu$m) along the height of the channel. The vortex length is normalized by the post diameter d and shown in Fig. 4.2(a) where black dots represent the statistical mean of the vortex length for all samples (80 snapshots for a duration of 200 s) and the shaded blue region represents 5^{th} and 95^{th} percentile to indicate the lower and upper bound of the extent of the vortex. We note that for the Newtonian solvent, no vortex or irregular flows can be observed at all experimental flow rates.

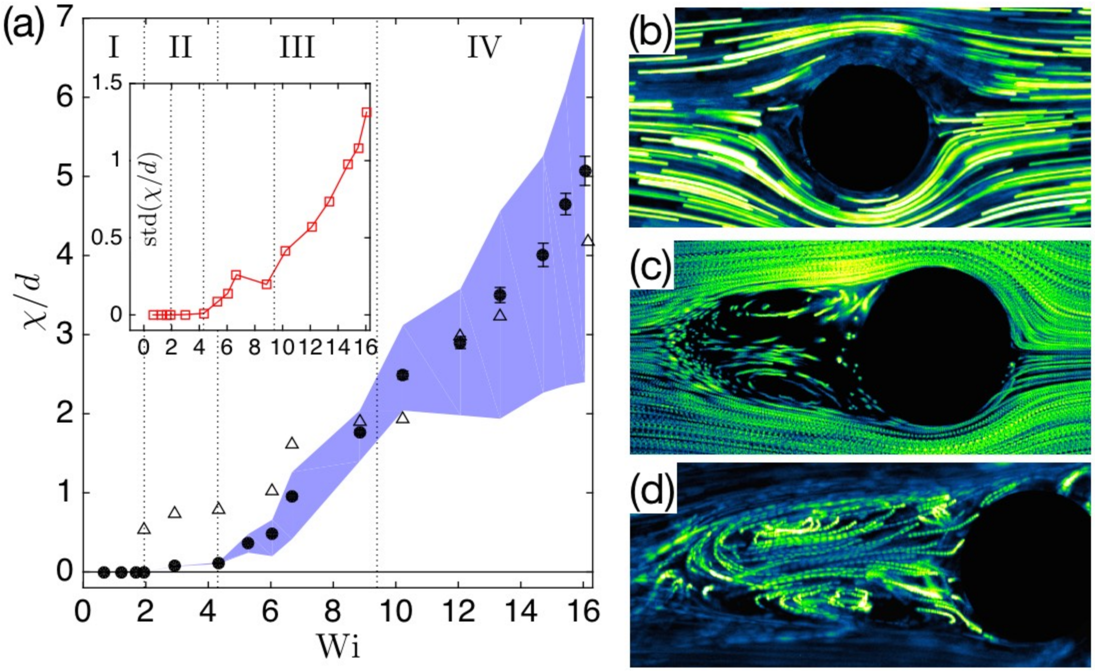

Figure 4.2: (a) Vortex length normalized by post diameter d as a function of Wi. Each black dot represents the mean of the vortex length sampled over 200s and shaded region represents 5th and 95th percentile. Four regimes of vortex dynamics can be identified. I: steady fore-aft symmetric profile with no vortex. II: emergence of steady vortex in front of the post. III: vortex becomes unsteady and grows in length. IV: pulsing vortex which collapses suddenly to a length of around 2D. Inset: rms fluctuation of normalized vortex length. (b) streak plot for regime I. (c) streak plot in regime II showing vortex that is symmetric around channel centerline at Wi$\sim$4 and (d) subsequently symmetry breaking at higher $Wi \sim 8$ in regime III.

For the viscoelastic fluid, however, we can clearly identify four regimes as the flow Weissenberg number increases. For $Wi \lesssim 2$ (regime I in Fig. 4.2a), the flow around the cylinder possesses fore-aft symmetry identical to the creeping flow shown in Fig. 4.2(b). Beyond a critical Weissenberg number $Wi \sim 2$, however, we see the emergence of a recirculation zone made up of two rotating vortex rolls that are symmetric relative to the line $y = 0$ passing the center of the cylinder, as in Fig. 4.2(c). The flow is steady and the pattern does not change over several minutes. As Wi increases, the stagnant region become highly elongated and extend further upstream along the centerline (regime II in Fig. 4.2a), before reaching another flow transition at $Wi \approx 4$. For $Wi \gtrsim 4$ (regime III in Fig. 4.2a), the size of the recirculation zone becomes unsteady and fluctuates weakly in time. This can be seen in the 5th and 95th percentile of all observed vortex lengths, shown by the shaded area in Fig. 4.2(a). These percentile curves begin to deviate from the mean in this regime, indicating variance in the sampled vortex lengths. The unsteadiness of the vortex length is also reflected in the increase of root-mean-square (rms) fluctuation of χ/d, shown in Fig. 4.2(a) inset. The rms fluctuation, however, saturates before reaching $Wi \sim 9$. In this regime (III), the vortex grows rapidly in size with Wi and the lateral symmetry of the two vortex rolls is lost, as shown in Fig. 4.2(d). Lastly, for $Wi \gtrsim 9$, the flow enters into a regime where the vortex frequently collapses suddenly to 2 post diameter and then regenerates, as shown by the constant 5th percentile curve despite increasing Wi. The vortex length frequently "pulse" in time with large rms fluctuations, as shown previously by the streak plots in Fig. 4.1(b-c). The mean vortex length continues to grow with Wi and extends far upstream, reaching 6 post diameters (3 channel width) at $Wi = 16$.

Although the observed vortex is measured in an $x - y$ plane, the structure and dynamics are far from two-dimensional. In fact, the structure of the flow switches from two bi-stable modes in the z direction, as we explore next.

4.3.2. Upstream Vortex: 3-Dimensional Structure

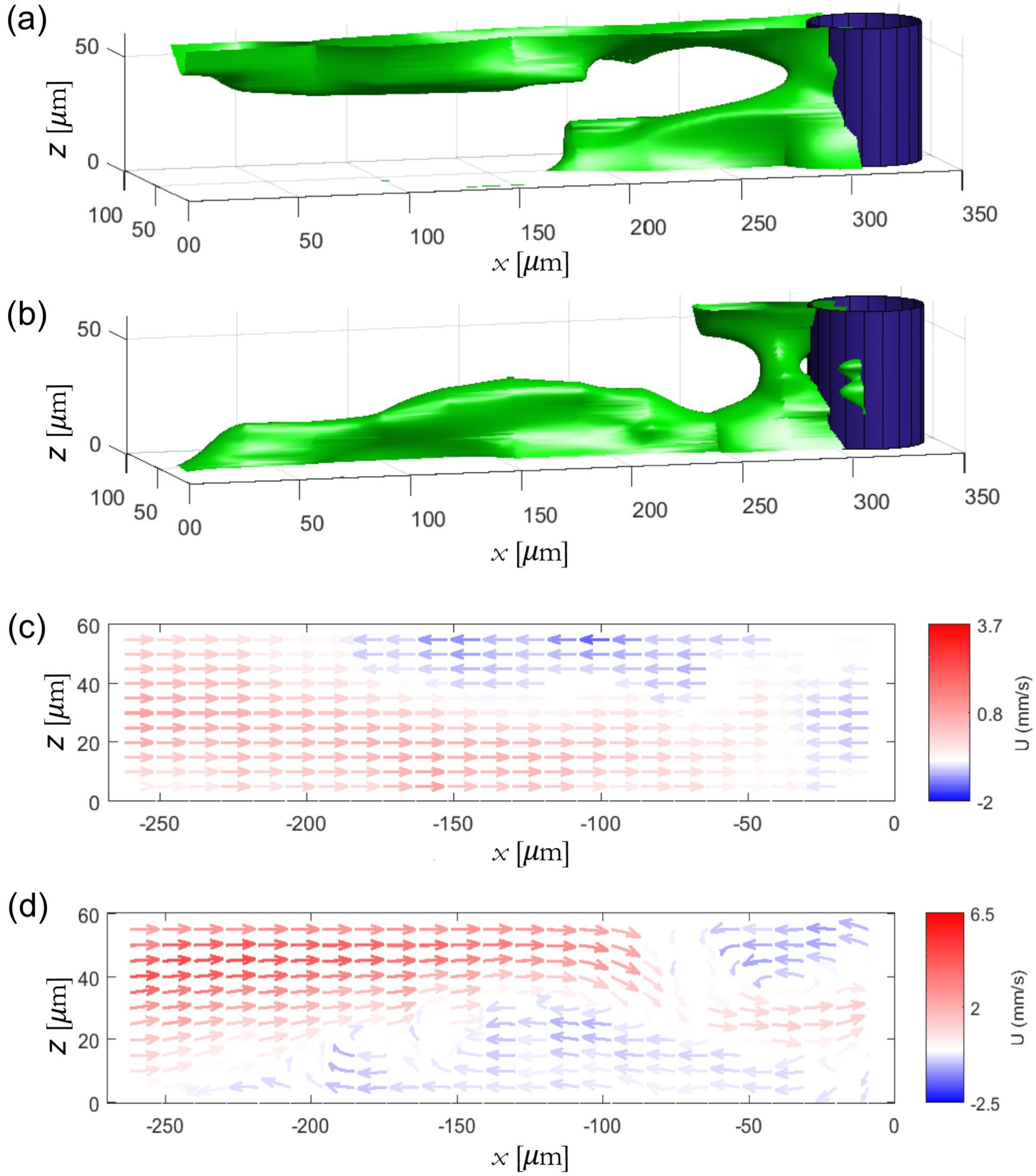

Figure 4.3: Three dimensional structure of the stagnant vortex upstream of the cylinder in the pulsing regime ($Wi = 23$). (a) Snapshot of the stagnant vortex defined by the isosurface for zero speed $U = 0$ showing the dominance of the vortex near the top wall. (b) Snapshot showing the complementary case where the vortex near the bottom wall dominates. (c,d) Velocity maps along a cross-section passing through the channel centerline for similar cases shown in (a,b) respectively.

In order to visualize the full flow structure upstream of the cylinder, we use holographic particle tracking to reconstruct the three-dimensional flow field. To identify the stagnant region, characterized by negative streamwise velocity, we plot the isosurface where the velocity magnitude is zero. Figure 4.3(a,b) show two snapshots of the spatial structure of the stagnant region at different times. It is clear that the flow is in fact made up of a pair of two separate recirculation zones originating near the corner of the cylinder with the walls. The vortex regions extend upstream along the top and bottom surfaces. Moreover, the vortex growth along one wall is accompanied by the suppression of the vortex on the other wall. The switching between the two states occurs irregularly in time: as the stagnant zone collapses on one side, the other vortex reforms. The symmetry breaking in the z-direction for the entire flow field is evident in Fig. 4.3 (c,d), where the corresponding velocity field in a $x - z$ cross-section along the channel centerline is plotted. The presence of the backwards flow (blue) clearly alters the surrounding bulk flow, as shown by the streamwise flow (red) in Fig. 4.3 (c,d). The generation of backwards flow originates along the upstream sides of the cylinder that drives flow along top or bottom surface. In the pulsing regime, the vortex in an extended position can separate from the cylinder and move upstream along the top or bottom surface. Meanwhile, the other vortex expands in the z-direction and fills the space directly in front of the post.

The origin of the vortex regions may be the minimization of the flow extension due to high fluid extensional viscosity [161], similar to contraction type geometries cite. The flow field develops recirculating vortices in order to produce an effectively longer entrance region for the flow to increase in velocity gradually and reduce the extension rate $\dot{\epsilon} \sim \partial U/\partial x$ around the post. This connection of the vortex regions to the bulk flow provides insight into perturbation produced by the cylinder and will be explored next.

In Fig. 4.4 (a,b), we distinguish the bulk flow from the vortex region by comparing the high-velocity isosurface $U = 6.9$ mm/s with the low-velocity ones $U = 0$, measured simultaneously. We find that the stagnant vortices constrict the flow and cause an increase in

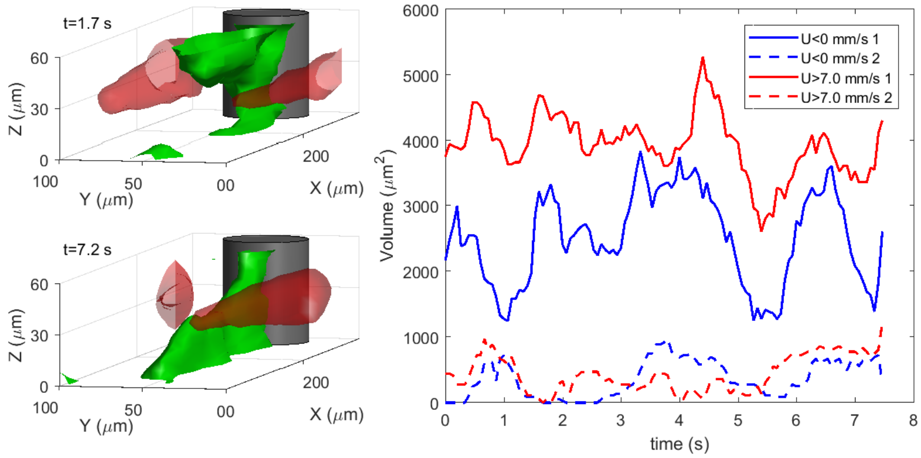

Figure 4.4: (a,b) Surfaces of equal velocity from holographic velocimetry in front of the cylinder at two different time instances. Regions of zero velocity, $U = 0$ form in front of the post along the top or bottom walls. High velocity regions $U = 6.9$ mm/s separate into two regions along the left and right sides of the channel. (c) The volume of flow above a critical flow rate $U \geq 6.9$ mm/s compared to the volume of the back flow $U \leq 0$ over a length of $1W$ upstream of the post. The strong correlation indicates that vortex region acts to constrict the bulk flow into a smaller region.

bulk flow speed. As the bulk flow separates into two high velocity regions surrounding the stagnant region, the stagnant zone takes up cross-sectional area upstream of the post, which then constricts the streamwise flow. This constriction causes an increase in the bulk flow velocity on one side of the channel. In Fig. 4.4 (c), we compare the volume of the stagnant vortex (low velocity region) and the bulk flow (high-velocity region) within $1W$ upstream of the micropost. Indeed, the two signals are highly correlated. The growth of the upstream vortex corresponds to an increase in the bulk velocity magnitude. Similarly, periods of reduced vortex size correspond to transitional states where the bulk flow occupies larger cross section.

The flow symmetry also breaks down in the spanwise y-direction, resulting in a shift of the primary flow to either the left or right of the channel. For instance, Fig. 4.4(a) shows the region has shifted the predominant flow towards the left side and Fig. 4.4(b) shows the dominant flow on the right. This results in a greater flow along the right side of the post. In fact, the flow rate around either side of the post are found to be anti-correlated due to constant volume flow rate, but can vary by approximately 20% from the mean, suggesting flow switching and symmetry-breaking in the spanwise y direction. Lastly, while the vortex formation increases the local velocity upstream of the post, we show in the subsequent section these fluctuations are not communicated downstream, although the variation in flow to either side of the cylinder may produce further disturbances downstream. Instead, we find that the same instability actually propagates upstream.

4.3.3. Disturbance Propagation and Elastic Waves

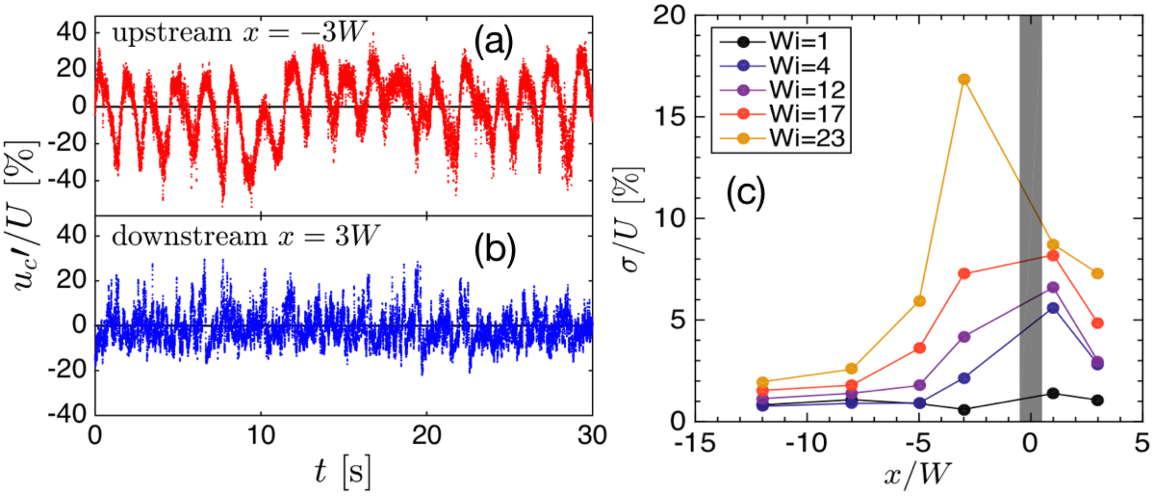

Figure 4.5: (a) Fluctuation of the centerline velocity u_c' normalized by the mean far from the cylinder at an upstream location $x = -3W$ for $Wi = 23$ and (b) downstream at $x = 3W$. The gray line represents the flow of the Newtonian fluid at similar flow rates in each of these plots. (c) The normalized root mean square of the centerline velocity fluctuation at various channel locations and Weissenberg number.

The unsteady vortex is accompanied by bulk flow instabilities. To quantify the fluctuation in the unstable flow, we conduct flow velocimetry focused on a small window in the channel centerline and monitor the instantaneous streamwise velocity u_c at various channel x locations. The fluctuation is then obtained by subtracting the mean $u_c' = u_c - \overline{u}_c$ from the instantaneous velocity. To facilitate comparison between various flow rates, we normalize the velocity fluctuation with the mean centerline velocity U far from the cylinder. In Fig. 4.5(a), we plot the time series of the normalized velocity fluctuations at $3W$ upstream of the cylinder. We observe large fluctuations (20% of the mean flow) for the viscoelastic flow compared to the Newtonian solvent (gray line). The flow downstream of the cylinder at comparable location, however, sees a different type of fluctuation. The amplitude of the fluctuation is much smaller and the signal shows frequent jumps to the high velocity amidst dwelling at low velocities.

The impact of the vortex instability is not confined to the vicinity of the cylinder but propagates far upstream. In Fig. 4.5(c), we plot the root mean square velocity fluctuation σ normalized by U at various x locations. For low Wi ($\lesssim 1$), we see very little velocity fluctuations at all channel locations. As Weissenberg number increases, we see the flow becomes weakly unstable upstream of the cylinder, similar to the observation of the vortex length shown in Fig. 4.2(a). However, the flow downstream of the cylinder also becomes unstable and the level of fluctuations is in fact higher than that upstream. As Wi further increases, the upstream velocity fluctuation rapidly grows in strength and propagates increasingly further upstream. At $Wi = 23$, it can be felt over $10W$ upstream of the cylinder. The increase in flow fluctuation upstream must be due to the presence of cylinders, since very far upstream ($20W$ above), the flow is found to be steady with fluctuations close to the instrument noise.

The propagation of the disturbance upstream suggests a mechanism by which the flow downstream can communicate with the flow upstream even in the presence of strong advection by mean flow. Specifically, we investigate the relay of disturbance by computing the two-point cross-correlation. In Fig. 4.6(a), we compute the cross-correlation coefficient for the two streamwise velocity measured simultaneously at $-3W$ and $-2W$ upstream (dashed black curve). First of all, we see that the two signal are highly correlated, with $\rho(\tau)$ reaching almost 0.8. Note that a perfect correlation has $\rho = 1$, anti-correlation has $\rho = -1$, while uncorrelated signal has $\rho = 0$. However, the peak shift time τ_p occurs at a non-zero location, around -0.14 s. This means that the velocity signal at $-3W$ leads $-2W$ by 0.14 s. This lead time turns out to be much longer than if only advection by mean flow exist, which is around 0.018 s. This time increases if there is an elastic wave traveling upstream

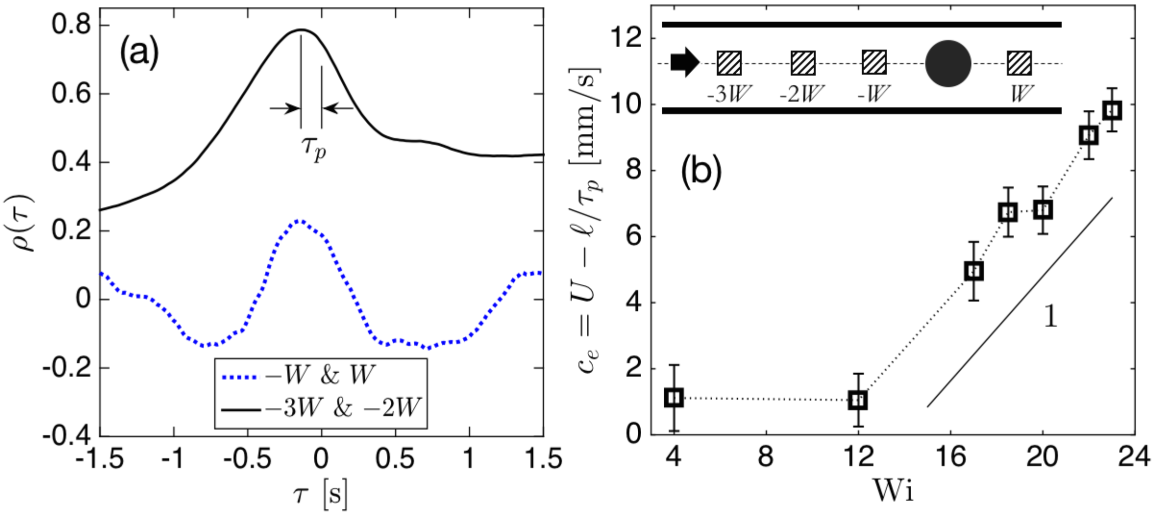

Figure 4.6: (a) Cross-correlation coefficient between velocity signals measured simultaneously but between different locations at $Wi = 23$. The cross correlation between the flow upstream and downstream or $-W$ and W is shown by the dashed blue curve while that between two upstream locations is shown by the solid black curve. (b) The elastic wave speed computed via the peak shift time as a function of Wi.

with wave speed, c_e that goes *against* the bulk advection. The net result is a reduction in speed and increase in the time needed to travel:

$$\tau_p = \frac{\ell}{U - c_e}, \tag{4.1}$$

where τ_p is the peak shift (lead/lag) time, ℓ is the separation distance between the two observation points, U is the mean advection speed, and c_e is the elastic wave speed. We note that the minus sign implies the wave is going in the direction opposite to the bulk flow and the shift time reflects the competition between the wave speed going upstream and the advection of fluid downstream.

Since all quantities other than c_e can be directly measured, we can then compute c_e. We can measure the peak shift time and extract the corresponding wave speed for two pairs of locations $-3W, -2W$ and $-2W, -W$. The average of the two pairs is then report in Fig. 4.6 (b) for various Weissenberg number. Since flow is steady without fluctuation below $Wi = 4$, we only report results for $Wi \gtrsim 4$. However, since accuracy of the methods relies on a large velocity fluctuation from which a shift time can be measured, we note that only flows in the pulsing regime ($Wi \gtrsim 9$) demonstrate a clear wave speed. As shown in the figure, the elastic wave increases with Weissenberg number almost linearly for $Wi \gtrsim 9$. This implies that as Wi increases, the disturbance increases in strength and propagates upstream faster.

The propagation of the disturbance upstream due to the elastic wave seem to follow very different dynamics compared to the flow in the cylinder wake. When we compare the velocity signals measured simultaneously $1W$ upstream and downstream of the cylinder, we find that the signals are weakly correlated, as in Fig. 4.6(a). This is expected from the very different velocity time series shown in Fig. 4.5 (a,b), where the characteristics of the fluctuation are clearly uncorrelated. Hence we conclude that the upstream instability and the wake instability follows markedly different mechanisms.

4.4. Summary

Using conventional and holographic particle tracking methods, we study the three-dimensional structure and dynamics of the flow of viscoelastic fluids around a confined cylinder. In contrast to most studies of viscoelastic flow around cylinders, we observe a region of stagnant flow forming in front of the cylinder. We attribute the difference to the vertical confinement of the microchannel, which produces a flow similar to a planar constriction where entrance vortices are observed. The flow differs from a planar contraction because the post separates the flow into two streams. The stagnant votices form along the top and bottom of the channel at a critical Wi number. As flow rate increases, the streamwise length of the vortex increase linearly with Wi, similar to theory for entrance flows of high Trouton ratio fluids.

The velocity fluctuations in front of the post are 3-dimensional in nature, notably shifting upward and downward (in the axial direction of the post) around the stagnant regions which extend along the top and bottom walls. At sufficiently high Wi, the flow switches between two dominant states characterized by strong symmetry breaking in the channel height direction with violent pulsing behavior.

Strikingly, the disturbance propagates far upstream, rather than confined to the extend of the vortex. Although the flow downstream of the cylinder becomes unstable, the strength of the instability upstream is comparable at high Wi. Further the two instabilities, although separated only by a cylinder 50 μm in diameter, appears to be isolated from each other and possess very distinct temporal and spatial features. Finally, we identified an elastic wave speed with which disturbance can travel upstream. This wave speed is found to increase linearly with Wi. Our results provide insight into the source of this perturbation and build towards understanding the more complex flows such as flow in porous media.

CHAPTER 5 : 3-D Elastic Instabilities in Cross-slot Channels

5.1. Introduction: Polymer Dynamics and Flow Instabilities in Elongational Flows

The dynamics of long chained polymers in elongational flow is of fundamental importance in polymer physics. The complex behaviors of these polymers in elongational flows, such as strain-dependent elastic stresses, nonlinear spring constants, and conformational changes often lead to flow instabilities that plague industrial processes such as fiber spinning, extrusion, and molding. At the microscopic level, polymers can undergo a phase transition from a coiled state to an elongated state, known as "coil-stretch" transition in extensional flows [43]. On the other hand, the reverse process from stretched to coiled state is found to be strongly hysteretic [94] and can lead to the so-called "buckling instability" of the long-chain macromolecules, which has been reported for actin filaments [49] and birefringent strands [162]. At the macroscopic flow level, the bulk flow behavior is often studied in extensional systems such as the cross-slot channel which resembles the classic four rolling mill geometry. Arratia et al experimentally found two flow transitions in the purely elastic regime, a steady symmetry breaking instability followed by an unsteady flow switching instability in the elongational plane [47]. Subsequent 2-d simulations found qualitative agreement [85] and 3-d simulations investigated the role of channel aspect ratio on the flow transitions and argued that the flow is redirected via a path of least resistance [163]. Recently, Sousa *et al* quantified the flow characteristics in the elastic turbulence regime [48], while Burshtein *et al* found additional instabilities in the elasto-inertial regime [164] and detailed a phase diagram from the inertia-dominated to the elasticity-dominated regime. However, the 3-dimensional structure of the flow as well as the presence of any tertiary flow instabilities in the purely elastic regime remains unexplored.

Using holographic particle-tracking and pressure measurements, we report a new symmetry-breaking instability *normal* to the extension plane, marked by bi-stable flow switching in that direction and "buckling" of the separatrix between the impinging streams. The disturbances propagate upstream with periods of synchronization and desynchronization. These complex flow structures may be present in other extensional geometries.

5.2. Experimental Setup and Methods

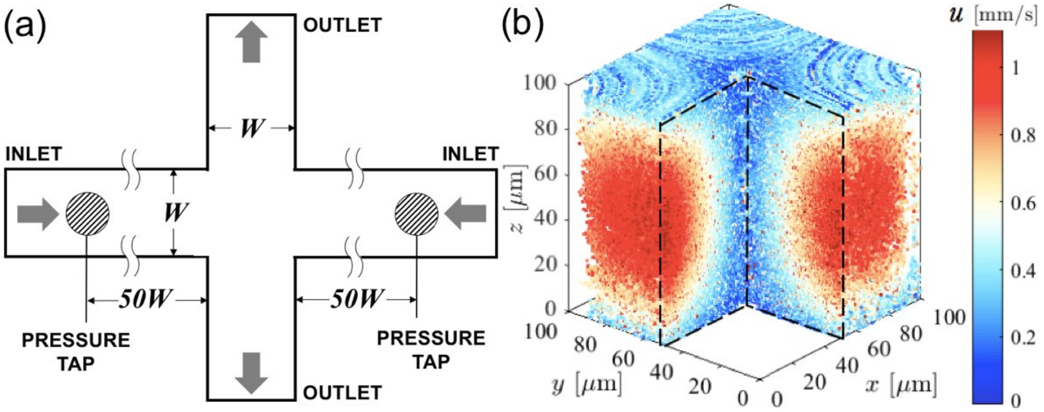

Figure 5.1: (a) Cross-slot channel apparatus, with width $W = 100\,\mu$m and height $D = 90\,\mu$m. The pressure sensors are placed at $50W$ towards the inlets. (b) Cutaway view of the ensemble of three-dimensional particle trajectories and velocity fields obtained from the holographic particle tracking velocimetry.

The cross-slot channel used in the experiments is shown in Fig. 5.1(a). The channel width is $W = 100\mu$m and depth is $D = 90\mu$m. The confinement ratio is $\alpha = D/W = 0.9$ and the extensional strain rate near the stagnant point is estimated by $\dot{\epsilon} = 2Q/DW^2$ where Q is the volumetric flow rate prescribed externally with a syringe pump (Harvard Apparatus PHD2000). Two fluids are used in the experiments, a polymeric fluid consisting of 300 ppm PAA in 90% by weight glycerol aqueous solution and a Newtonian fluid 90% glycerol aqueous solution. The extensional Weissenberg number is $Wi = \lambda\dot{\epsilon}$ where λ is the longest relaxation time measured by stress relaxation.

We measure the 3-dimensional flow field in a volume centered around the central hyperbolic point within the cross-slot using holographic particle tracking technique described in section 2.2. The size of the volume is approximately a cube that is 100μm in span and shown in Fig. 5.1(b), where the Lagrangian particle trajectories are shown in 3-d and colored by speed. Further, we measure the pressure signal upstream of the cross-slot using two pressure taps

(Honeywell TBPDANS series), installed at about $50W$ upstream of the cross-slot center. The two sensors record the pressure signals simultaneously with a time resolution of 5 ms and a pressure accuracy of 0.02 psi.

5.3. Results and Discussion

We begin with flow characterization in the extensional x, y plane, in which the flow enters along the y-axis and the leaves along the x axis. Snapshots of the flow streamlines colored by the velocity magnitude u normalized by the mean channel velocity, $U = Q/WD$ are shown in Fig. 5.2(a,b) for Newtonian and viscoelastic fluids at comparable extensional rates. For Newtonian fluid (90% glycerol), the flow within the extensional plane remains steady and symmetric around the hyperbolic point for all flow rates, as shown in Fig. 5.2(a). The flow for the viscoelastic fluid, on the other hand, becomes highly asymmetric and the inflow streams choose randomly between two outflow directions via a path of minimal resistance. Such symmetry breaking instability and time-dependent instability *within* the elongational plane have been well documented experimentally [47] and numerically [85, 163]. We note that for our system, the asymmetric flow becomes unsteady and switches between the two bi-stable modes for extensional rates larger than $\dot{\epsilon} \gtrsim 4$ s^{-1}.

The flow structures *normal* to the extension plane, however, have not been previously investigated in detail. In the following section, we document the presence of (i) tertiary flow structures that occur in the plane normal to the planar extension and (ii) an unsteady "buckling" instability of the separatrix between the inlet streams.

5.3.1. Symmetry Breaking in Three Dimensions

The break down of symmetry, however, is not limited to the extensional plane. In fact, the symmetry breaking occurs also normal to the extensional plane. Using three-dimensional holographic particle trajectories such as those shown in Fig. 5.1(b), we can probe the entire flow structure in 3-d, particularly the velocity profiles along z direction. First, we show the flow field within a $y-z$ cut-plane that passes through the hyperbolic point and extends along

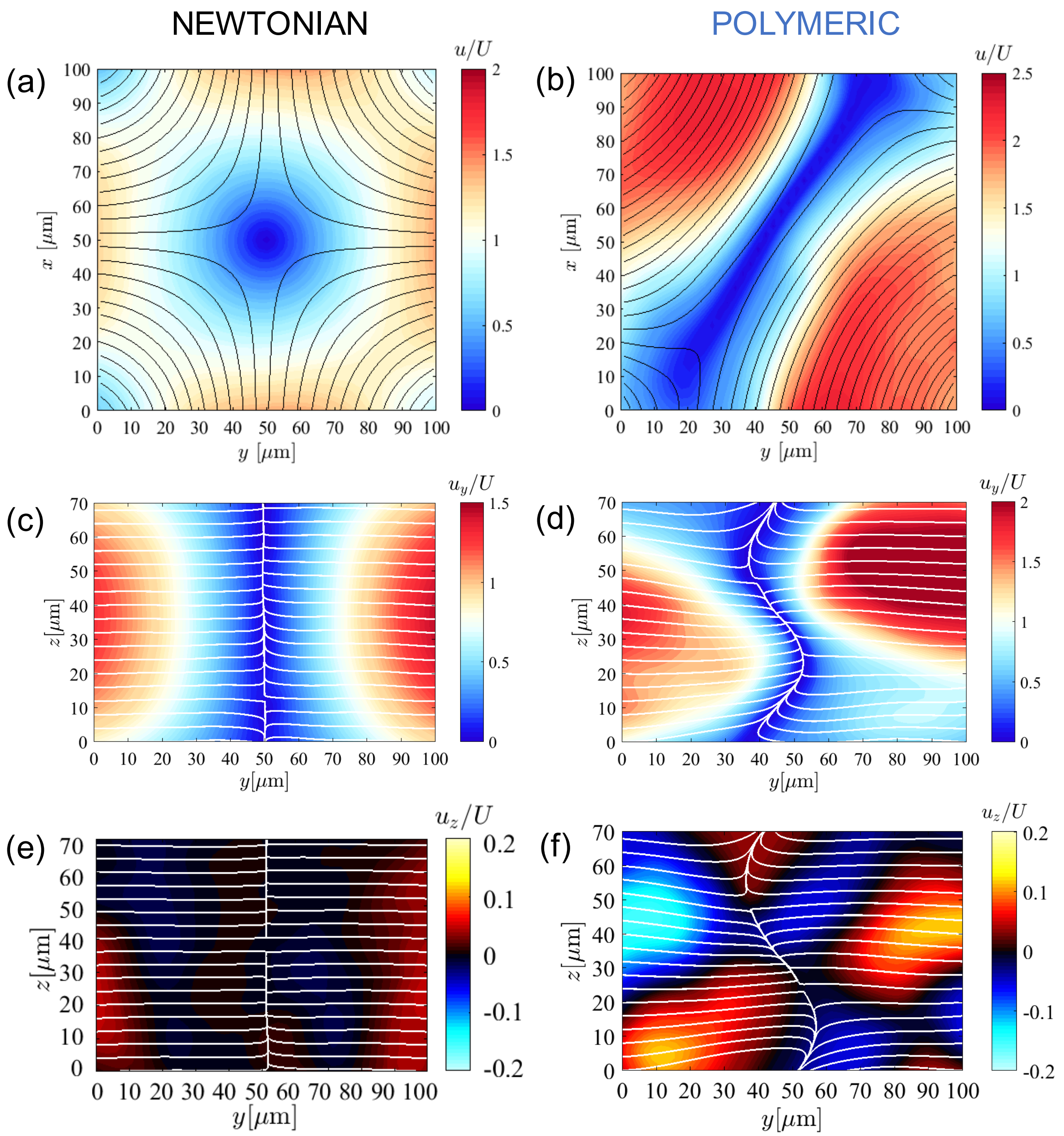

Figure 5.2: Secondary and tertiary instability in the cross-slot flow of viscoelastic fluids. Left column is Newtonian fluid and right column is viscoelastic fluid at comparable extensional strain rates $\dot{\epsilon} = 11$ s^{-1}. (a,b) Streamlines and normalized velocity magnitude map in the extensional $x - y$ plane for (a) Newtonian and (b) viscoelastic fluid, showing the well-known secondary asymmetric flow instability. (c,d) Streamlines and normalized u_y component map in a cut-plane normal to the extensional plane and along the inflow direction ($x = 50$ μm) for (c) Newtonian and (d) viscoelastic fluid. Note that the flow enters along y direction and exits along x. (e,f) Streamlines and map of normalized tertiary velocity u_z in the same cut-plane for (e) Newtonian and (f) viscoelastic fluid.

the inlet (y) direction. In Fig. 5.2(c,d), we plot the u_y velocity component normalized by mean flow speed U and flow streamlines. For Newtonian fluids (Fig. 5.2 c), the streamlines are parallel and the two inflow streams are symmetric both in y and in z, resembling typical parabolic profiles. The flow of the viscoelastic fluid, however, is very different. We find a clear breaking of symmetry that occurs in z, where the inflow streams appear to misalign in z and preferentially choose between the upper or lower streams. Moreover, the streamlines are curved with a clear velocity component in z. In Fig. 5.2 (e,f) we explore the z velocity component u_z and indeed, we find the presence of converging and diverging flows in the viscoelastic case. We see that compared with the Newtonian case, the streamlines for the viscoelastic are significantly curved and the z velocity map showed that, as the flow approaches the stagnation regions, it diverges and converges in z.

A closer inspection of Fig. 5.2(f) shows that, an additional symmetry breaking can be found in z where the separatrix between the two streams appears to be "buckling", i.e., the boundary of the two impinging streams displays a curved mode, which we describe in detail below.

5.3.2. Buckling of the Inflow Separatrix

To visualize the separatrix between the two impinging streams, we normalize the streamwise u_y by the local speed u along the $y - z$ cut-plane that passes through the geometric center of the cross-slot, shown in Fig. 5.3. This component is chosen since it clearly distinguishes the two streams. We denote the stagnant region as the curve where the two incoming inlet streams meet and where the u_y velocity is zero. For Newtonian flows and viscoelastic flow at low strain rates, the stagnant region remains vertical and the two streams are symmetric. For $\dot{\epsilon} > \dot{\epsilon}_c \approx 4\,\mathrm{s}^{-1}$, however, we find that this stagnant region becomes irregular and switches between various curved forms resembling that of the Euler mode in beam buckling. For example, snapshot resembling the 2nd modes are shown in Fig. 5.3 (a,b). As the flow rate further increases, higher order modes are excited more often in addition to the low order modes, see Fig. 5.3 (c,d).

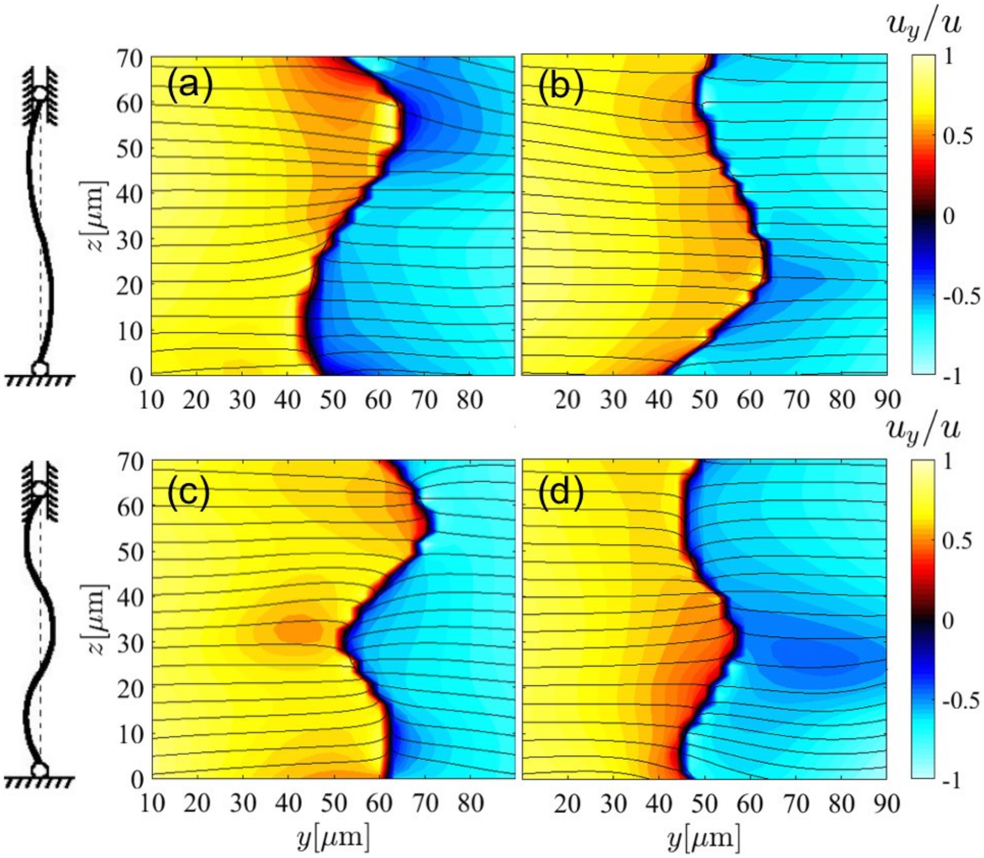

Figure 5.3: "Buckling" modes of the separatrix between the two impinging inlet streams. This boundary undergoes irregular transitions between various shape modes: (a,b) show a second order mode while (c,d) show a third order mode. We find that these transitions accompany the symmetry breaking events in the extensional $x - y$ plane.

We can quantify the onset of symmetry breaking in the z direction by measuring the relative strength of separatrix buckling modes. We define the amplitude of the n^{th} mode as the integral dot product with the sinusoidal modes:

$$A(n) = \left| \int y^* \cdot \sin\left(n\pi y^*/L\right) dz \right|, \tag{5.1}$$

where $y^*(z)$ is the profile for the separatrix. This amplitude can be averaged over all observed samples and the first five modes are shown in Fig. 5.4 (a). We see that for Newtonian flow even at high extensional rate, all mode amplitudes are close to zero on par with system noise level, since the flow is steady and Stokesian. The viscoelastic fluid at low exten-

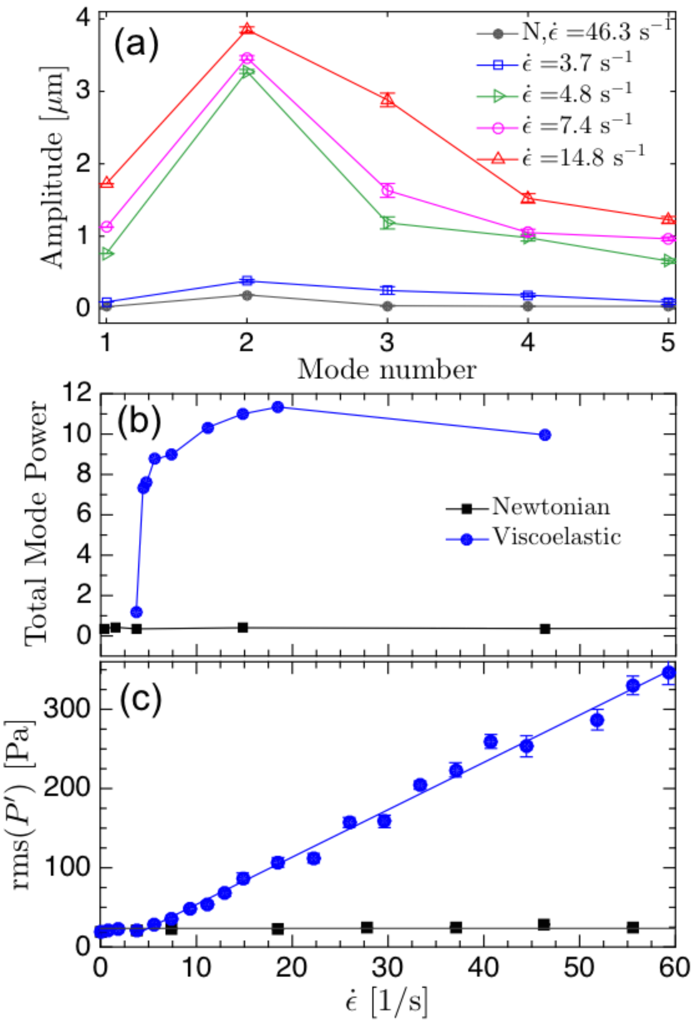

Figure 5.4: (a) Statistical mean amplitudes of the "buckling" modes. (b) The sum of mean amplitudes of all modes as a function of strain rate. A clear transition from flat to curved separatrix between the two streams occurs at around a critical strain rate of $\dot{\epsilon}_c \approx 4$ s^{-1}. This coincides with the strain rate at which the flow becomes unsteady. (c) Onset of flow fluctuation occurs at strain rate of 4 s^{-1}, as measured by root mean square pressure fluctuations upstream of the cross-slot.

sional rate is similar to the Newtonian case, without strong excitation of modes. Once the extensional rate exceeds $\dot{\epsilon} \gtrsim \dot{\epsilon}_c$, however, a sudden onset of buckling modes occurs. The amplitudes increase significantly for all modes and are dominated by the second mode. As extensional rate further increases, we see that the strength of the higher order modes, particularly the third mode, increases drastically.

The onset of the transition can be seen clearly by the total amplitude summed across all modes in Fig. 5.4 (b). As extensional rate increases, the Newtonian total amplitude remains close to zero as expected. For the viscoelastic fluid, however, we see a transition to a branch with high level of mode amplitudes which saturates for $\dot{\epsilon} > 15$ s^{-1}.

Interestingly, this transition occurs at a critical extensional rate $\dot{\epsilon}_c$ that coincides with the onset of flow unsteadiness as measured by pressure fluctuations. In Fig. 5.4 (c) the root mean square (rms) of pressure fluctuations $P' = P - \langle P \rangle$ is shown as a function of extensional rate for both Newtonian and viscoelastic fluids. First we note that the rms fluctuation for the Newtonian fluid remains close to 20 Pa for all $\dot{\epsilon}$. The viscoelastic case, on the other hand, sees significant increase in pressure fluctuations for $\dot{\epsilon}_c \approx 4$ s^{-1}, the onset of unsteady flow in our system.

5.3.3. Pressure Fluctuations and Correlation

Next, we report evidence that the flow dynamics within the cross-slot can influence the flow upstream. We find that even though the pressure is measured $50W$ upstream of the cross-slot, the disturbance can still be felt. Indeed Fig. 5.5(a) shows large irregular fluctuations in the pressure time signals measured upstream of the cross-slot for viscoelastic fluids. The signals measured simultaneously at the two inlets are shown at $\dot{\epsilon} = 74$ s^{-1}.

Upon closer inspection of the pressure time series taken at both inlets, however, we observe segments of strongly correlated behavior followed by anti-correlated behavior. The two types of behavior alternates in time. We hypothesize that this pressure behavior can be related to the flow switching found within the cross-slot.

To further quantify this temporal dynamics of the pressure signals at the two inlets, we divide the signals into segments of 5s and compute the correlation factor between the segments taken at the two inlets. The instantaneous correlation factor $\rho(t)$ can thus be obtained to characterize whether the flow is correlated or anti-correlated at a particular instant. In Fig. 5.5 (b), we shown the time trace of $\rho(t)$. Intervals where $\rho \geq 1/3$ are labelled red while those satisfying $\rho \leq -1/3$ are labelled blue. We can see clear switching events from

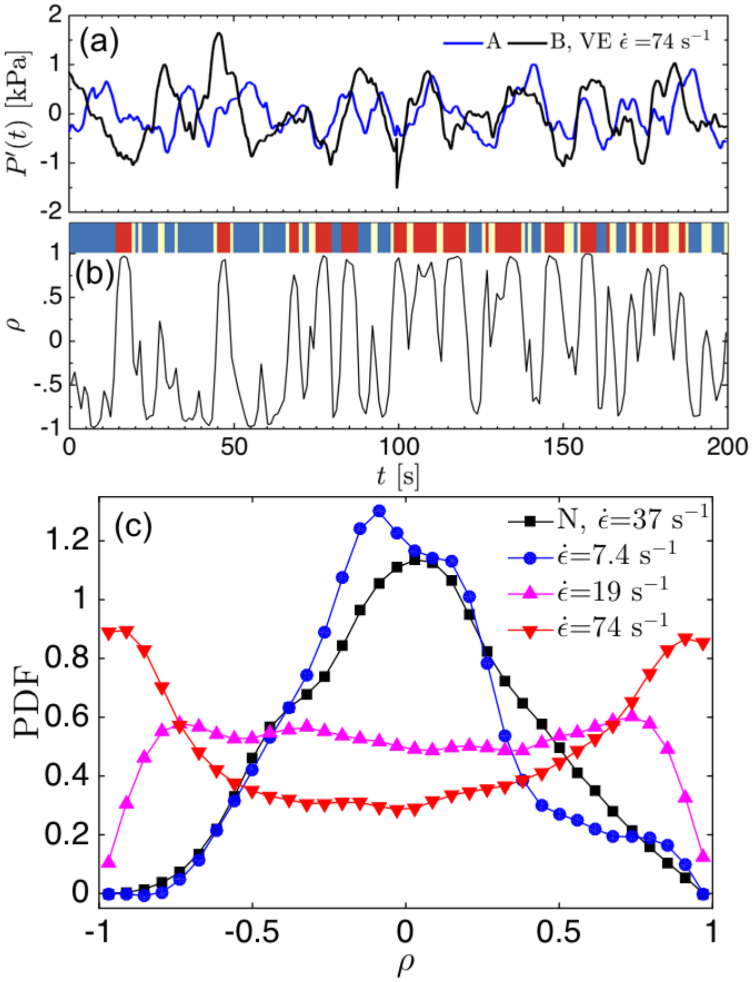

Figure 5.5: (a) Pressure signals measured upstream of the cross-slot. Alternating intervals of strong correlation and strong anti-correlation are observed for viscoelastic fluids at high strain rates. (b) Cross correlation coefficient between the two signals computed for sequential intervals that are 5 seconds in duration. Intervals of strong correlation ($\rho > 1/3$) are labelled by red bands, while intervals with strong anti-correlation (ρ <1/3) are labelled blue. They are found to be interspersed by brief periods of uncorrelated signal (white). (c) The probability distribution of the cross correlation coefficients for viscoelastic fluids at increasingly high extensional strain rates and Newtonian fluids. As strain rate increases, the two streams become more likely to either vary together or against each other.

correlated motion to anti-correlated motion.

The onset of such behavior can be quantified by varying the extensional rate. We can compute the probability distribution of all sampled correlation factors, shown in Fig. 5.5 (c). First, we note that for the Newtonian fluid at high strain rates $\dot{\epsilon} = 37$ s^{-1} the distribution follows a Gaussian distribution centered around 0, since the two signals are mostly steady and randomly correlated. A similar distribution is also found for the viscoelastic fluids at low strain rates $\dot{\epsilon} = 7.4\ \mathrm{s}^{-1}$ (blue) where the flow is mostly steady. As we further increase $\dot{\epsilon}$, however, the distribution for viscoelastic fluid changes drastically. The distribution becomes increasingly bimodal and is heavily distributed near 1 and -1, indicating the two signals are either correlated or anti-correlated, at $\dot{\epsilon} = 75\ \mathrm{s}^{-1}$. This behavior suggests that the two input streams are competing and interacting with each other, similar to the switching in separatrix buckling modes.

5.4. Summary

In summary, using novel holographic particle tracking, we showed the presence of three-dimensional structure in the classic cross-slot flow instability of a viscoelastic fluid. We identified a tertiary flow instability and a "buckling" instability of the stagnation region in the direction perpendicular to the plane of extension. The onset of these tertiary structures, however, does not seem to coincide with the symmetry breaking in the extensional plane. Rather, it occurs when the flow becomes unsteady. Further, the disturbances generated by the cross slot flow instability propagate far upstream. The inlet stream pressure signals alternate between periods of correlation and anti-correlation.

Part II

Biological Systems: Transport in Complex Fluids & Flows

CHAPTER 6 : Flagellar Kinematics and Algal Swimming in Viscoelastic Fluids

6.1. Introduction: Swimming in Viscoelastic Fluids

The motility of microorganisms and organelles through micro-structured fluids plays an important role in many biological processes such as fertilization [165–168], respiratory health [117, 169], development of disease [170] and bio-degradation in soil [171]. Disruption of normal motility can occur due to unexpected changes in the nature of the surrounding fluids. For instance, the beating of filamentous cilia that pump mucus in the respiratory tract [168,172,173] and the flagella driven swimming of spermatozoa through cervical mucus [174, 175] are both affected by the properties of the mucus such as water content and viscoelasticity. At larger scales, the undulatory motion of *C. elegans* in wet soil [176] or through polymer networks [177] is influenced by the rheology of the mud as it moves.

Many microorganisms move in the realm of low Reynolds number $\mathrm{Re} \equiv \rho \ell U/\mu \ll 1$ because of either small length scales ℓ, low swimming speeds U or both. In a Newtonian fluid with constant density ρ and viscosity μ, the lack of inertia implies linear fluid kinematics that is fully reversible in the swimmer configurations. To swim, therefore, organisms must execute non-reversible, asymmetric strokes to break free of the curse set by the so-called "scallop theorem" [105]. In many instances, however the ambient fluid environment is far from Newtonian due to the presence of macromolecules such as biopolymers and proteins, which impart complex rheological characteristics such as shear rate dependent viscosity and viscoelasticity. In a viscoelastic fluid, elastic stresses are strain and time dependent. Consequently, kinematic reversibility can break down.

The consequences of fluid elasticity on the details of swimming while clearly important, are not well understood, and have recently received growing attention [120, 121, 123–126, 168, 178–180]. Most recent work has been theoretical in nature relying on detailed simulations [122, 124, 125] or asymptotic solutions to idealized models [121, 178, 179]. Taken together, current studies paint a complicated and sometimes contradictory picture. For instance, theories on the small amplitude swimming of infinitely long wave-like sheets suggest that elasticity can reduce swimming speed [121, 178] and these predictions are consistent with experimental observations of undulatory swimming in *C. elegans.* [123]. Similar trends were found recently [122] on studies of the motility of both idealized "pullers" (such as *C. reinhardtii*) and "pushers" (such as *E. coli*). On the other hand, simulations of finite-sized moving [124] filaments or large amplitude undulations [125] suggest that fluid elasticity can increase the propulsion speed - consistent this time with experiments on propulsion due to rotating rigid mechanical helices. [126] The emerging viewpoint is that fluid microstructure and swimming kinematics *together* impact motility in a non-linear manner [125].

Here, by systematically modifying the elasticity of the fluid, we studied the variation of the flagellar beat pattern, beat frequency, and swimming velocity for the bi-flagellated swimmer *Chlamydomonas reinhardtii.* We find that fluid elasticity can modify the beating pattern (i.e. shape) and enhance the alga's beating frequency and wave speed. Despite this enhancement, the alga's swimming speed is overall hindered (as much as 50%) by fluid elasticity due to the elastic stresses in the fluid. Numerical simulations using swimming strokes gathered in the experiments reveal that the minimization of elastic stresses may be at the root of the change in swimming gait and effect of fluid elasticity is asymmetric between the power stroke and recovery stroke.

6.2. Experimental and Numerical Methods

6.2.1. Active Swimmer: Bi-flagellated Algae

We experimentally investigate the effects of fluid elasticity on the swimming behavior of the bi-flagellated green alga, *Chlamydomonas reinhardtii.* With an ellipsoidal cell body roughly 10 μm in size and two anterior flagella each of length $\ell \sim 10$ μm, the alga *C. reinhardtii* is a model system in biology and has been widely used in studies of motility and phototaxis [181]. The two flagella possess the same conserved "9+2" microtubule arrangement seen in other eukaryotic axoneme [181] such as those seen in sperm tails and airway cilia. As a pair, these flagella execute cyclical beating patterns resembling breast-stroke with asymmetric recovery and power strokes. Figure 6.1(b,c) show two snapshots of *C. reinhardtii* swimming at Re $\sim 10^{-3}$ in a water-like M1 buffer solution.

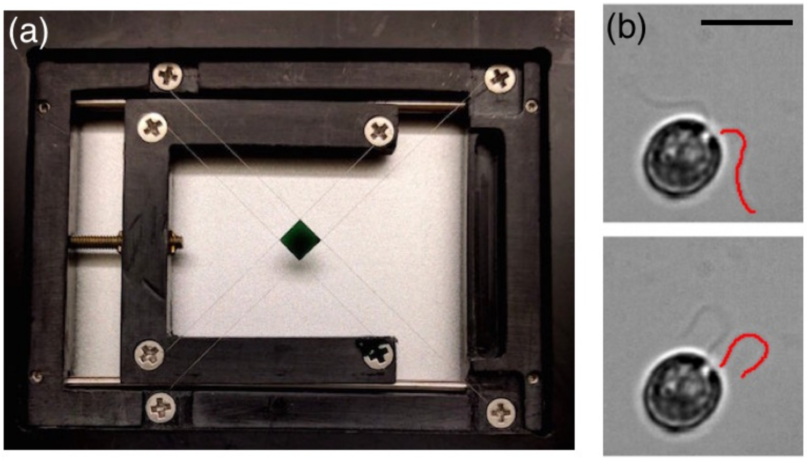

Figure 6.1: (a) thin fluid film ($20\,\mu$m thickness) stretched across custom made wire-frame device. (b) swimming of *C. reinhardtii* at the start of recovery stroke (top) and power stroke (bottom). Scale bar is 10μm.

6.2.2. Working Fluid and Experimental Apparatus

Two types of fluids are used in the experiments – Newtonian and viscoelastic. Newtonian fluids are prepared by dissolving low molecular weight Ficoll (Sigma-Aldrich) in M1 buffer solution with viscosities ranging from 1 cP to 10 cP. Viscoelastic fluids are prepared by adding flexible polyacrylamide polymers (PAA, MW=18×10^6, Polysciences) to water. The polymer concentration ranges from 5 to 80 ppm resulting in fluid relaxation times λ that range from 6 ms to 0.12 s. This solution is considered dilute since the overlap concentration is approximately 350 ppm. An effective viscosity $\mu = [\eta(\dot{\gamma}_{\text{body}}) + \eta(\dot{\gamma}_{\text{flag}})]/2$ is used to facilitate comparison at similar viscosity but different elasticity. Here $\dot{\gamma}_{\text{body}}$ and $\dot{\gamma}_{\text{flag}}$ is the shear rate at the body and the flagella, respectively.

Dilute *C. reinhardtii* suspensions are made by suspending motile algae in either Newtonian or viscoelastic fluids. A small volume of this suspension is then stretched to form a thin film

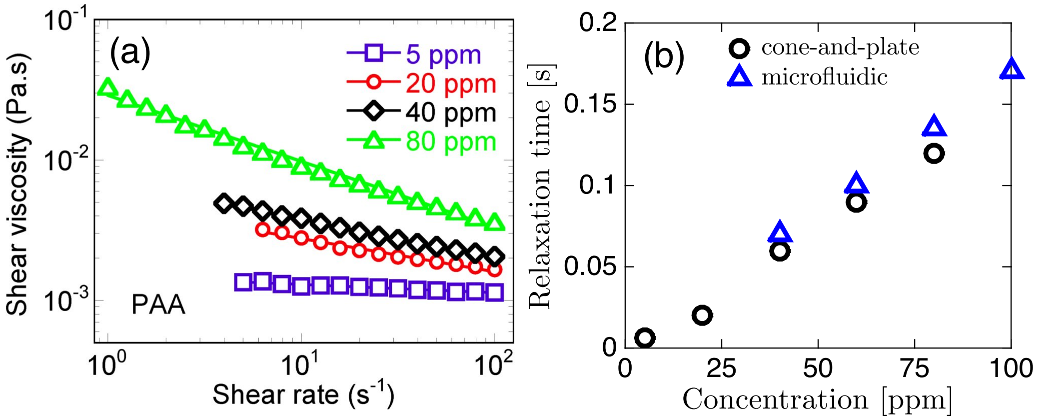

Figure 6.2: (a) Steady shear viscosity of the polymeric fluids used in the experiments. (b) Fluid relaxation time versus polymer concentration, as measured using stress relaxation test on a cone-and-plate rheometer and microfluidic rheometer.

(thickness $\approx 20\ \mu$m) using custom wire-frame device, shown in Fig. 6.1(a). The cell motion in the thin film, along with the flagellar contours are then imaged using bright field and phase contrast microscopy and then recorded using high speed camera. The shapes of the flagella, shown by the red curves in Fig. 6.1(b), as well as the centroids of the cell body are tracked simultaneously for cells that exhibit periodic symmetric strokes only. Motile modes such as synchronous waving of the two flagella and "wobbling" where the two flagella are de-synchronized, are not included in the kinematics statistics.

The shapes of the flagella as well as the trajectory of the cell centroid are tracked simultaneously. Instantaneous swimming speeds are then calculated by differentiating the centroid position and the sign determined from the cell orientation. The speed of the swimmer measured in the thin liquid film set-up are consistent with that in the bulk fluid reported by other researchers [182]. We note that the swimming gait generates far-field flows similar to that of a negative force dipole for idealized "puller" [19, 122].

6.2.3. Numerical Techniques

Numerical simulations of the experimental flagellar kinematics are conducted in full three-dimensions using the Oldroyd-B model where the polymer stress tensor is related to the conformation tensor as:

$$\boldsymbol{\tau}_p = \frac{\eta_p}{\lambda}(\boldsymbol{\sigma} - \boldsymbol{I}) \tag{6.1}$$

where $\boldsymbol{I}$ is the identity tensor. The conformation tensor reflects the orientation and stretching of the polymer molecules and evolves with:

$$\frac{\partial \boldsymbol{\sigma}}{\partial t} + \boldsymbol{u} \cdot \nabla \boldsymbol{\sigma} - \left(\boldsymbol{\sigma} \cdot \nabla \boldsymbol{u} + \nabla \boldsymbol{u}^{\mathrm{T}} \cdot \boldsymbol{\sigma} \right) = -\frac{1}{\lambda}(\boldsymbol{\sigma} - \boldsymbol{I}) + \varepsilon \Delta \boldsymbol{\sigma}, \tag{6.2}$$

note here that an artificial stress diffusion term $\varepsilon \Delta \boldsymbol{\sigma}$ is added for numerical regularization [143]. Since $\varepsilon \propto (\Delta x)^2$, we note that in the limit $\Delta x \to 0$, this regularized model converges to the Oldroyd-B model. The elastic strain energy density is defined by the trace of the stress tensor $\mathrm{Tr}(\boldsymbol{\tau}_p)$.

Immersed boundary method is used to couple the flagellar motion to the surrounding fluid. In this method, Lagrangian coordinates are used to describe the swimmers position, velocity and forces, and Eulerian coordinates to describe the fluid velocity, stress and pressure. We use ideas from the immersed boundary method to couple the Eulerian and Lagrangian variables. The flagellar contour locations obtained from the experiments are discretized and the Lagrangian points on the flagella boundary are mapped to the Eulerian flow field. Specifically, the force density on the swimmer is related to the force applied to the fluid via spreading function.

In each time step of the simulation, we alternately advance the conformation tensor, update the fluid velocity and pressure, and then the translational velocity and fluid forces on the swimmer. We require that the swimmer moves with the local fluid velocity (i.e. there is no slip on the body surface), and that the swimmer is force free. Lastly, the fluid domain is taken as a periodic cube with side lengths 40 μm (about 4 body diameters), which is discretized with 128 points in each direction. Each flagellum is discretized with 27 grid points along its centerline.

6.3. Results Part A: Experiments

6.3.1. Beating Frequency and Net Swimming Speed

We begin by investigating the effects of fluid viscosity on the beat frequency (Fig. 6.3a) and on the cycle averaged net swimming speed (Fig. 6.3b). In Newtonian fluids, for viscosities $\mu \sim 2$ cP and lower, the frequency is roughly around 56 Hz. Increasing the viscosity further ($\mu > 2$ cP) results in a monotonically decreasing frequency. Here, the decay is well captured by $\omega \sim 1/\sqrt{\mu}$ consistent with models suggesting that emergent frequencies are selected based on a balance of internal active processes, the elastic properties of the flagellum and external viscosity [183]. For polymeric fluids with low viscosities (low PAA concentration), the frequencies are consistent with the Newtonian values. At higher concentrations of polymer, however, significant deviation from the Newtonian trend is observed, even though the fluid has comparable viscosity. Surprisingly, the beating frequency increases with increasing fluid viscosity (elasticity) and then seems to saturate.

The observed increase in beating frequency, however, does not translate into an increase in overall swimming speed. Figure 6.3(b) shows that the average net swimming speed U of the *C. reinhardtii* cell body decreases as the fluid viscosity increases for both Newtonian and polymeric solutions. For low viscosity values ($\mu < 2$ cP), the swimming speeds are very similar for the algae cells in Newtonian and polymeric liquids. As polymer concentration increases, however, we find that fluid elasticity consistently hinders self-propulsion compared to Newtonian fluid at comparable viscosity. For both Newtonian and polymeric fluids, we find the data consistent with the relationship $U \sim \mu^{-1}$, which suggests that the algae are operating at nearly constant thrust. Such a relationship has also been observed for free swimming *C. reinhardtii* in low viscosity Newtonian fluids ($1 < \mu < 2$ cP) [184].

The data shown in Fig.6.3(a,b) suggests the increasing importance of elasticity at higher polymer concentrations. To quantify the level of elasticity experienced by the swimmer, we introduce the Deborah number, defined here as $De \equiv \omega\lambda$ where ω is the mean frequency of a

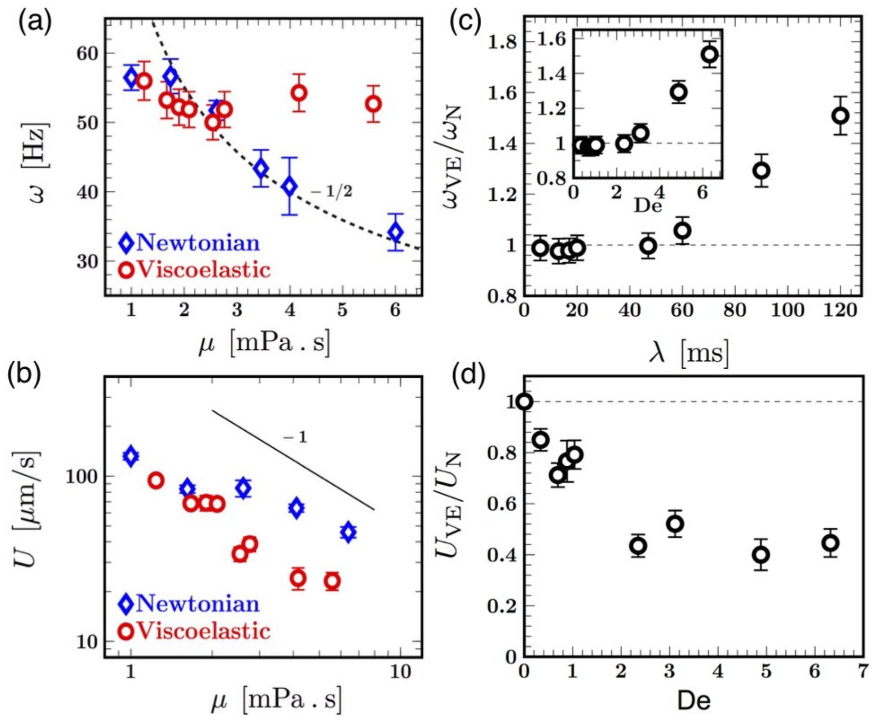

Figure 6.3: Effect of viscosity and elasticity on swimming kinematics: elasticity increases frequency but hinders motility. (a) The beating frequency ω for Newtonian and viscoelastic fluids. Dashed line represents power law, $\omega \sim 1/\sqrt{\mu}$. (b) The net swimming speed U averaged over many oscillations is shown as a function of μ. (c,d) Experimental data replotted to emphasize the role of elasticity encapsulated by the Deborah number (c) Frequency contrast $\omega_{\mathrm{VE}}/\omega_{\mathrm{N}}$ as a function of the the relaxation time λ. The Newtonian value is based on the mean beating frequency in a fluid with the same viscosity. (Inset) The frequency contrast replotted as a function of the Deborah number. (d) The speed ratio $U_{\mathrm{VE}}/U_{\mathrm{N}}$ as a function of De - here, U_{VE} is the speed in viscoelastic fluids and U_N is the swimming speed in the Newtonian counterpart.

representative sample of cells and λ is the fluid relaxation time from rheometry; we note that $De = 0$ for Newtonian fluids. The normalized beating frequency and net algal swimming speed as a function of De are shown in Fig. 6.3(c) and Fig. 6.3(d), respectively. For ease of presentation, we normalize the measured frequency and net swimming speed with the Newtonian value at comparable viscosity. Figure Fig. 6.3(c) shows the monotonic increase in the frequency as the relaxation time of the fluid increases from around 20 to 120 ms. The transition from a Newtonian-like response ($De \lesssim 1$) to a clear viscoelastic regime occurs at around $De \sim 2.5$, where the frequency is on the order of the fluid relaxation time, suggesting that elastic fluid stresses are modifying kinematics. The ratio of swimming speeds plotted in Fig. 6.3(d) is consistently less than unity demonstrating that fluid elasticity hinders net locomotion. The decrease is quite substantial even for relatively low values of De. For example, fluid elasticity hinders the cell swimming speed, relative to Newtonian fluids, by as much as 50% for $De \approx 2$. We also observe that the ratio plateaus to approximately 0.4 for $De > 2$. This asymptotic behavior has been previously observed in theoretical studies [121, 178] and also in experiments with worms. [123] The reduction in motility is also consistent with recent simulations [122] of steady flow of weakly elastic fluid around idealized pullers. This plateau may indicate an upper bound on the generated elastic stress around the organism.

6.3.2. Elasticity Impacts Power and Recovery Stroke Asymmetrically

The net frequency and swimming speed while central to the alga's overall motility, do not distinguish between the highly asymmetric power and recovery strokes. Therefore, we next calculate the mean speed during the power stroke U^+ and the mean speed during the recovery stroke U^- for Newtonian and viscoelastic fluids. Figures 4(a) and 4(b) summarize our observations. For Newtonian fluids, both the power U^+ and recovery U^- stroke speeds decrease as μ increases, following the trend observed earlier for the Newtonian net swimming speed in Fig. 3(b). For viscoelastic fluids, however, we observe a sharp difference between power and recovery strokes. While the dependence of U^+ is similar to the Newtonian case, the recovery speed U^- in viscoelastic fluids remains relatively unchanged, and in fact modestly increases with viscosity. This raises the possibility that fluid elasticity affects power and recovery strokes very differently - a view supported by plots of the normalized power and recovery stroke speeds shown in Fig 4(c) and 4(d). We observe a minimum in the values of $U^+_{\mathrm{VE}}/U^+_{\mathrm{N}}$ and $U^-_{\mathrm{VE}}/U^-_{\mathrm{N}}$ at very low values of De. For larger values of De (> 2), the speed ratio during power stroke, $U^+_{\mathrm{VE}}/U^+_{\mathrm{N}}$ starts from values less than unity, but then increases and in fact exceeds unity at $De = 6.4$. On the other hand, the speed ratio during the recovery stroke, $U^-_{\mathrm{VE}}/U^-_{\mathrm{N}}$ is consistently greater than unity and increases with De. The

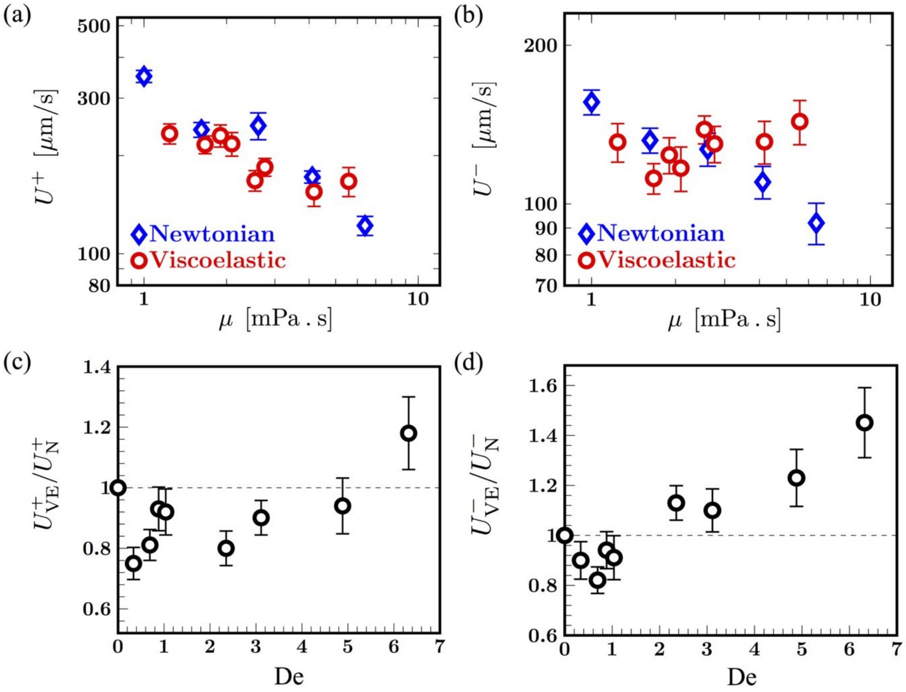

Figure 6.4: Effect of viscosity and elasticity power and recovery strokes within a cycle. (a) The average speed U^+ during the execution of a power stroke. (b) The average speed U^- during the recovery stroke. As before, the error bars denote standard error from 10-20 sample individuals. As viscosity increases, the Newtonian swimming speed decreases monotonically during both the power and recovery strokes. This contrasts significantly with two opposing trends seen in viscoelastic case. While U^+ during the power stroke reduces with increasing viscosity similar to the Newtonian case, the speed during the recovery stroke, U^-, is nearly constant and in fact increases for large viscosities. (c) Viscoelastic power stroke swimming speed normalized by the Newtonian counterpart of comparable viscosity, as a function of Deborah number. (d) The corresponding normalized speed for the recovery stroke.

bias of fluid elasticity in power and recovery strokes, as explored later using the numerical simulations, originates from the elastic stresses near the distill end.

We hypothesize that the proximal elastic stress concentration has opposing effects for the power and the recovery stroke. During the power phase, signed speed data show that the cell body is pulled forward by the flagella. This forward motion is resisted by the proximally located elastic stresses in the fluid, hence the motion will be impeded compared to the Newtonian case - i.e, $U^+_{\mathrm{VE}}/U^+_{\mathrm{N}} < 1$ as seen for $2 < De < 6$ in Figure 4(c). Added to this, fluid stretching at the hyperbolic flow points [182] in the anterior of the cell body results in enhanced extensional viscosity that hinders this forward motion. On the other hand, when the cell body recoils during the recovery phase, the relaxing polymer stress amplifies the backward motion, augmenting the speed - and thus $U^+_{\mathrm{VE}}/U^+_{\mathrm{N}} > 1$. The increase and build up of elastic stresses at the distal end may also separately enhance the power and recovery strokes by preventing the swimmer from slipping backwards as observed in simulations [124]. Consistent with this picture, we observe in Fig. 6.4(d) that as De increases, the backward speed during the recovery stroke increases. For the forward stroke, however, we do not see a monotonic drop in $U^+_{\mathrm{VE}}/U^+_{\mathrm{N}}$ with Deborah number, as one would expect by considering elastic stress alone. Rather, the ratio increases for $De \geq 2$ and eventually attains values greater than unity.

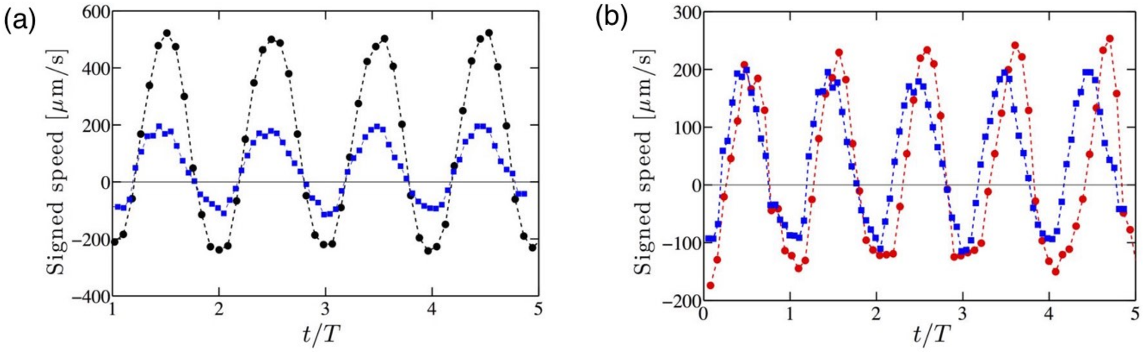

Figure 6.5: Instantaneous velocity tracer and Newtonian and viscoelastic fluids. (a) Instantaneous speed as a function of time scaled with the period, t/T for swimming in two Newtonian fluids - moderate viscosity 2.6 cP (black, circles) and high viscosity 6 cP (blue, squares). (b) Instantaneous speed in a viscoelastic fluid corresponding to $De = 6.5$ and $\mu = 5.7$ cP (red, circles) and a Newtonian fluid of comparable viscosity $\mu = 6$ cP (blue, squares).

A closer examination of the time scales of the beat cycle provides clues to a possible explanation. We note that the increase in $\omega_{\mathrm{VE}}/\omega_{\mathrm{N}}$ at $De \approx 2$ coincides with the increase in the power stroke speed. For beating at constant stroke pattern - thus constant amplitude - the speed may be expected to increase with the frequency in a manner similar that for idealized swimming sheets [106, 179]. Together, these have striking effects on the temporal composition of the beat cycle and resultant cell body displacements. In Fig. 6.5(a), we show instantaneous speeds in Newtonian fluids with two different viscosities plotted as a function of t/T, where T is the respective beating period. We observe the expected self-similarity where the instantaneous speed profiles collapse up to an amplitude scaling. Peak speeds of the recovery stroke occur at integer values of t/T; zero speed points coincide indicating equal proportion of power phase and recovery phase for beat patterns. Comparison of the Newtonian case with its viscoelastic analogue reveals a richer picture, c.f. Fig. 6.5(b). The viscoelastic case has slightly higher amplitudes for both power and recovery stroke. This is possibly due to polymer stretching "overshoot" that occurs at the switch between the power and recovery stroke, as observed in the transient extensional flows in dilute polymers [185]. Furthermore, the zero speed points coincide only at the start of the recovery stroke and the consistent delay in the start of the power stroke shows that the alga is experiencing a more extended recovery and a shortened power phase.

6.3.3. Elasticity Modified Swimming Gait

Seeking signatures and origin of this complex coupling between cell motion and flagellar strokes, we investigate the flagellar beat patterns, as illustrated in Fig. 6.6. The beating pattern of *C. reinhardtii* over one cycle in Newtonian and polymeric solutions of similar viscosity $\mu \approx 6$ cP are presented in Fig. 6.6 (a,c). The difference in shapes is striking and illustrates the effects of fluid elasticity on swimming. In the Newtonian case (a), the flagellum seems more mobile and significant changes in curvatures are attained over the whole cycle. In the viscoelastic case (c), lateral displacements of almost a third of the flagellum close to the cell body (green) appear to be severely restricted (less mobile) or bundled together with most of the bending occurring over the remainder of the length. Furthermore, we observe localized bending at the distal tip in the initial stages of the power stroke. The differences in the shapes can be quantified by plotting the spatio-temporal evolution of the scaled flagellum curvature $\kappa(s,t) = \tilde{\kappa}(s,t) \cdot \ell$ along the flagellar arc length s and over many cycles (Fig. 6.6 b,d). These kymographs show that regions of high curvature are found to distribute diagonally and periodically, characteristic of propagating bending waves. In the elastic fluid, (Fig. 6.6 d) flagella attain larger curvatures (dark blue regions)

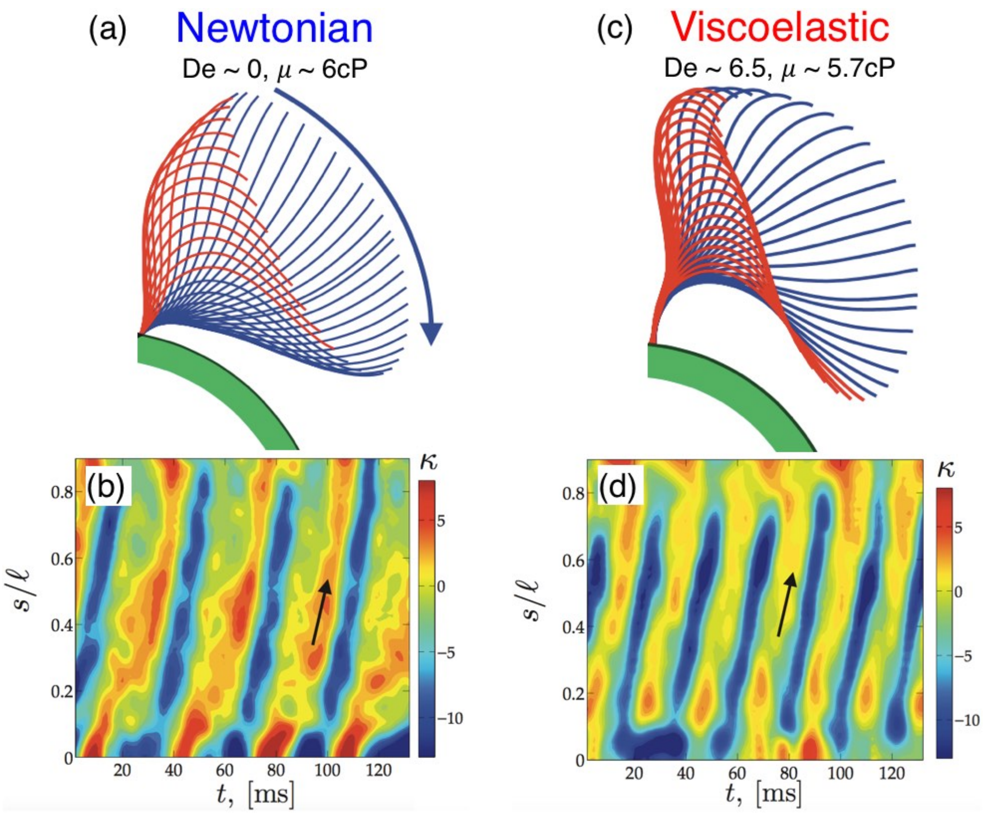

Figure 6.6: Fluid elasticity modifies swimming strokes. (a) Typical contours for one complete cycle illustrating the shapes during power (blue) and recovery strokes (red) for Newtonian fluid ($De = 0$, $\mu = 6.0$ cP) and (b) viscoelastic fluid ($De = 6.5$, $\mu = 5.7$ cP). (c,d) The corresponding kymographs of the spatio-temporal normalized curvature, $\kappa(s,t)$ along a flagellum. We see that increasing the elasticity results in larger curvature magnitudes (darker blue regions), significant differences in curvatures at the proximal end $s \approx 0$, and an increase in the frequency of bending waves (diagonally oriented lines - direction shown by arrow).

and an increase in the frequency of bending waves (diagonally oriented lines - direction shown by arrow). We also observed that for very low viscosities ($1 < \mu < 2.6$ cP), the distal tip gets closer to the cell body than for higher viscosity fluids. We can quantify this difference in curvature by computing the normalized curvature averaged over time t (≈ 6 cycles) and dimensionless arc length s/ℓ, here denoted by $\langle\kappa\rangle$. We find that at $\mu \approx 6$ cP, the value of $\langle\kappa\rangle$ is -1.44 and -2.72 for the Newtonian and viscoelastic fluids, respectively.

To further understand the asymmetric influence of elasticity on power and recovery strokes separately, we inspect the curvature profiles at particular phases within the cycle. Figure

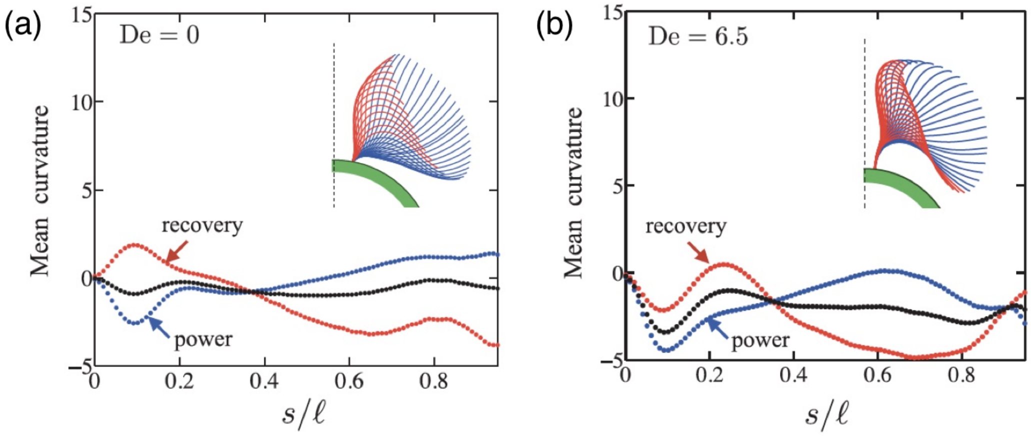

Figure 6.7: Fluid elasticity modifies power and recovery strokes separately. (a,b) Mean curvature profiles averaged over the power (blue) stroke, recovery (red) stroke and full beat cycle (black) for (a) Newtonian fluid, and (b) Polymeric fluid at comparable viscosity.

6.7(a,c) compares the normalized curvature averaged over the recovery stroke and the power stroke respective for (a) Newtonian and (c) viscoelastic fluids at compared viscosity. The most striking distinction for the viscoelastic fluid is the drastic change in curvature during the recovery phase near the proximal end. For the viscoelastic case (Fig. 6.7 c), the curvature is relatively fixed at $s \approx 0$ throughout the cycle (same sign as power stroke), while for the Newtonian case (Fig. 6.7 a), the curvatures vary significantly and in fact flip signs over a beat cycle. This agrees well with the apparent "bundling" near the proximal end shown in the flagellar contours in the insets.

Overall, our experiments show that during the recovery stroke, the changes in flagellar gait, the increase in beating frequency and the increase in the proportion of recovery stroke work in concert to enhance the speed during recovery stroke. In contrast, during the power stroke, the three effects compete with each other. The net result ultimately yields a reduction in speed of the alga. However, the origin of the change in the swimming gait as well as the role of elastic stresses remain unknown. In the next section, we will attempt to answer these questions using numerical simulations.

6.4. Results Part B: Simulation

6.4.1. Elastic Stress and Velocity for Viscoelastic Stroke

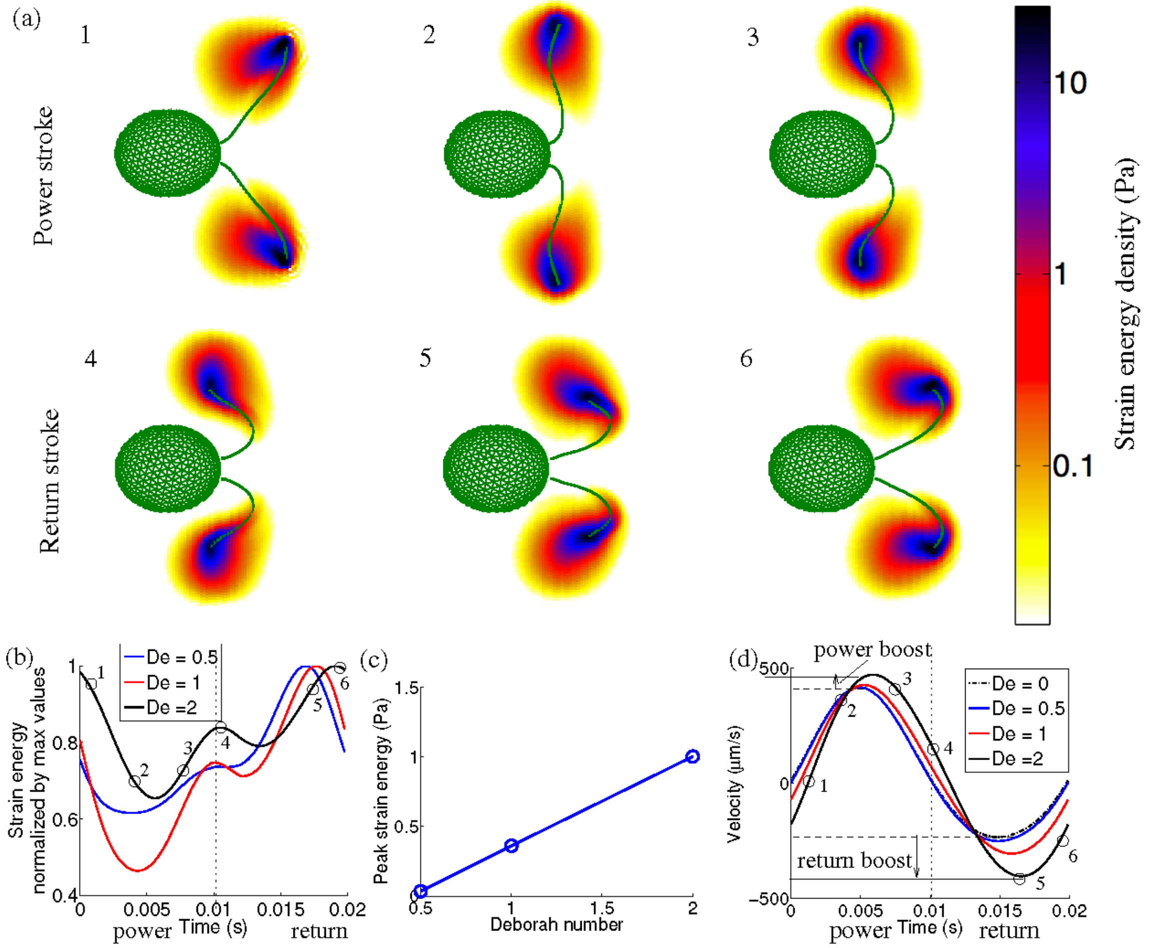

Figure 6.8: (a) Snapshots of strain energy density in the central plane for $De = 2$ using the viscoelastic stroke; the time points for these images are marked in (b) and (d) with the labels 1-6. (b) Root mean square of the strain energy density in the mid-plane as a function of time for different De normalized by maximum values. (c) Maximum values of root mean square of the strain energy density in the mid-plane, used to normalize (b). (d) Velocity over one stroke for different De. The power and return boosts are marked for $De = 2$.

Polymeric stresses are an important quantity that is difficult to obtain in experiments, but can be resolved in simulations. In this section we use the viscoelastic stroke obtained from experiments ($\mu = 2.5$ cP, $De = 2$) and vary the fluid relaxation time λ and consequently De in simulations. In Fig. 6.8 (a) we show snapshots of the fluid strain energy density in the central swimming plane at $De = 2$ (the Deborah number of the experiment from which this stroke was extracted). The strain energy density– the trace of the elastic stress tensor– gives a measure of the size of the elastic stress. It is notable that high stress is concentrated only near the distal tips of flagella, contrary to our previous conjecture that high stress regions develop near both ends of the flagella as well as near the body.

In Fig. 6.8 (b) we show the time trace of the spatially averaged strain energy density, normalized by the cycle maximum, throughout the entire stroke for different De. The elastic stress is generally lower during the power stroke than during the return stroke for all Deborah numbers. The lowest stresses occur near the middle of the power stroke, and the highest stresses occur towards the end of the return stroke. Moreover, the magnitude of the stress increases monotonically with Deborah number, as shown in Fig. 6.8 (c).

Next, we investigate the effects of accumulated stresses on the cell propulsion speed. The instantaneous velocity of the swimmer in a complete beating cycle is shown in Fig. 6.8 (d) for different De. We see that fluid elasticity boosts the speed of both the power and return strokes and produces a phase shift in which the peak velocities occur later in time. The size of the boosts and the extent of the phase shifts both increase with De. However, the speed of return stroke where the cell moves backwards is enhanced by a greater extent than the speed of the power stroke where the cell is moving forwards. This confirms the previous conjecture that the elastic stress increases both power and return strokes, as seen in the experiments, but the elastic slow-down in the net swimming speed results from the fact that the return stroke experiences a stronger speed boost (going backwards) than the power stroke (Fig. 6.8 d). As De increases, the net slow-down intensifies.

6.4.2. Comparing Performance of Newtonian and Viscoelastic Strokes

To further isolate the effect of fluid elasticity on swimming and provide a mechanism for the observed changes in flagellar gait, we conduct numerical simulation for two separate strokes observed in the experiment: (i) viscoelastic stroke at $De_0 \sim 2$, $\mu = 2.5$ cP versus

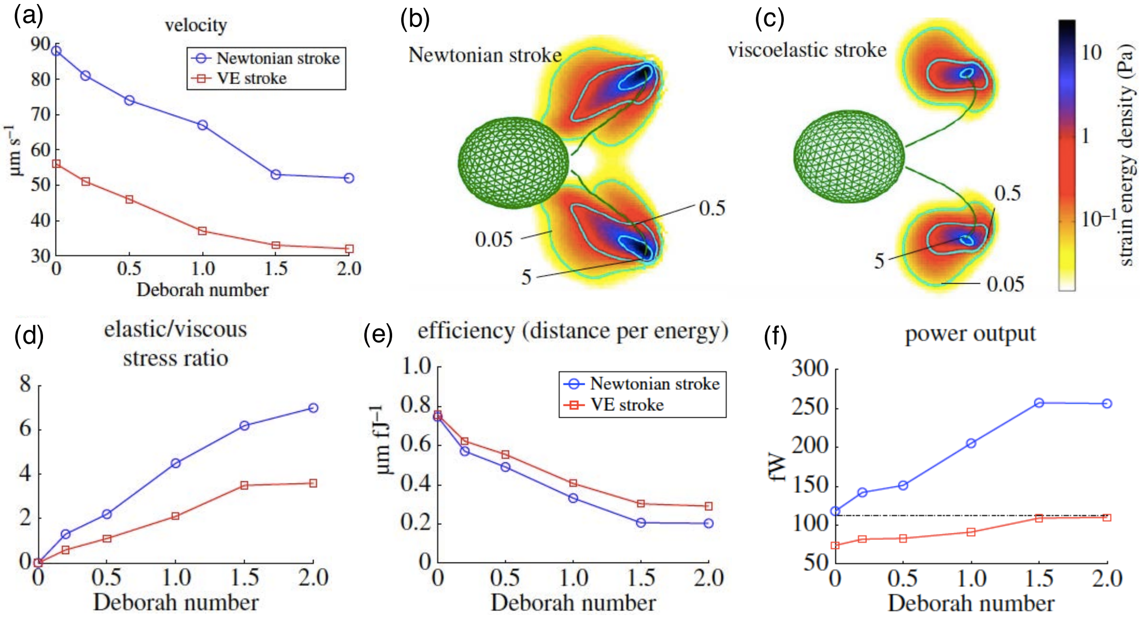

Figure 6.9: Simulation results showing the comparison of Newtonian stroke versus viscoelastic stroke, see text for methods of comparison. (a) Net swimming speed comparison shows Newtonian stroke produces much larger net speed for all De. (b,c) elastic strain energy around the flagella for the (b) Newtonian and (c) viscoelastic strokes at the same simulation De. The phase for both is the beginning of the power stroke. (d) Newtonian stroke (blue) generates significantly higher elastic stress compared to the viscoelastic stroke (red), as expected from the strain energy in (b,c). (e) Swimming efficiency comparison for the two strokes. (f) Power output comparison for the two strokes.

(ii) Newtonian stroke at $De_0 = 0$, $\mu = 2.6$ cP. These two strokes are then executed in the exact same viscoelastic fluid at varying relaxation times and hence De. Various cycle averaged quantities are computed to assess the swimming performance of the two strokes.

First, we find that the Newtonian stroke yields swimming speeds 60% faster than those of the viscoelastic stroke (Fig. 6.9 a), with both speeds decreasing with increasing Deborah number at about the same rate. The tradeoff of the faster swimming speed, however, is that the Newtonian stroke generates significantly higher polymer strains and expends more energy compared to its elastic stroke counterpart. Fig. 6.9 (b,c) shows the distribution of elastic strain energy around the swimmer. We see that the regions of high elastic strain energy are gathered near the distal tip and are much more extended in space for the Newtonian stroke than for the viscoelastic stroke. In fact, the zones of high elastic stresses extend to the cell body in the Newtonian case. When averaged over the swimming cycle, the viscoelastic stroke, on the other hand, sees consistently less field-averaged elastic stress than the Newtonian stroke, as shown in Fig. 6.9 (d).

This increased expenditure of energy into straining the polymers has severe consequences in swimming efficiency and power. In Fig. 6.9 (e), we compute the swimming efficiency, defined as the ratio of average speed to average power (distance travelled per energy dissipated). In a Newtonian fluid (De=0), the two strokes have comparable efficiencies. As we increase fluid elasticity, however, the viscoelastic stroke consistently yields higher displacements per unit energy input than the Newtonian stroke. Moreover, the power required to execute the viscoelastic stroke, as shown in Fig. 6.9 (f), increases only mildly with De. This is in stark contrast to the Newtonian stroke, where power need increased significantly. Note that the highest power output of the viscoelastic stroke is still below the lowest power output of the Newtonian stroke. The low energy requirement is particularly advantageous if micro-swimmer is power limited.

Hence, we find that in viscoelastic fluids, cells employing the viscoelastic gait swim slower but generates less stresses and use less power, and as a result the viscoelastic gait is more efficient.

6.4.3. Speed Enhancements by Fluid Memory

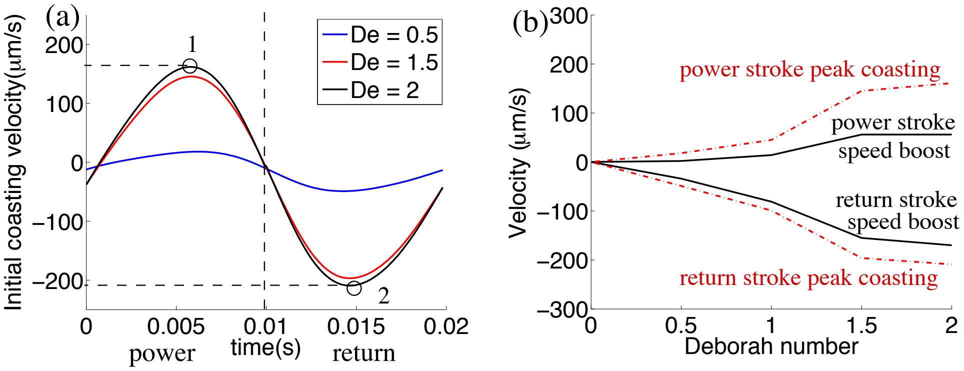

Figure 6.10: (a) Initial coasting velocity when the stroke is suddenly stopped, for various stroke phases. (b) Peak initial coasting velocity and “speed boost” for increasing De.

Both the experimental and simulation results reveal that the power and recovery speeds are enhanced for elastic fluids. But how are the speed enhancements related to accumulated elastic stresses? We address this question by conducting coasting numerical experiments where we fix the flagellar stroke and monitor the subsequent coasting velocity of the cell body.

In a Newtonian fluid (at zero Reynolds number), cell body stops instantly once the stroke is frozen since all forces are equilibrated instantaneously. In a viscoelastic fluid, however, once the flagella's shape is suddenly fixed, the swimmer continues to translate with a coasting velocity that is driven by the accumulated elastic stresses which is slowly relaxing. Hence, we can quantify the effect of fluid memory and elastic stress on the swimming speed by recording the initial coasting velocity (the initial velocity of the swimmer after the stroke is frozen) as a function of the stroke phase as shown in Fig. 6.10 (a). We find that indeed, the coasting velocity is significantly higher during return stroke compared to power stroke. At $De = 2$, for example, the peak coasting speed during the return stroke is $30 - 35\%$ higher than that during the power stroke.

Also, increasing fluid elasticity (larger De) leads to larger initial coasting velocities. In Fig. 6.10 (b), we plot the peak values of coasting velocity (dashed red) as a function of De, as well as the so-called "speed boost" (solid black line, defined by the difference between Newtonian and viscoelastic peak power or return velocities, seen in Fig. 6.8 d). These two quantities show a similar dependency on De that strongly suggests that the accumulated stress is a significant factor in the speed boost. Further, from Fig. 6.8 (d), we see that the peak power and return enhancements occur with a time lag (phase shift) from the peak velocities in the Newtonian fluid, indicating that as the stroke is beginning to slow down, fluid elasticity continues to accelerate the swimmer. Hence, the increased velocity and the tendency of the swimmer to continue to move when the flagellar motion is suddenly stopped, are the result of the accumulated elastic stress which provides a memory effect.

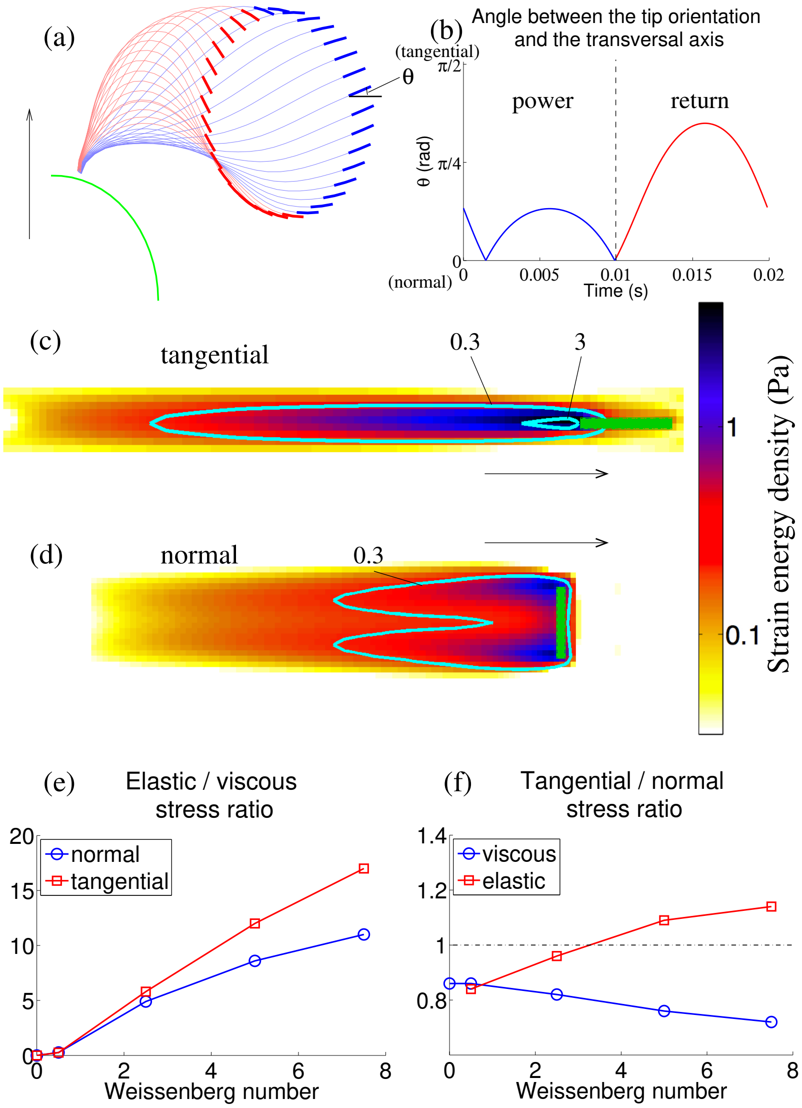

Figure 6.11: (a) The viscoelastic stroke ($De = 2$) with the tip of the flagellum highlighted. (b) Angle between the tangential direction of the flagellar tip and the axis perpendicular to the swimming direction for the same viscoelastic stroke. (c,d) Fluid strain energy density induced by a rod traveling (c) tangential and (d) normal to its long axis with $Wi = 7.5$; (e) Ratio of elastic stress to viscous stress induced by traveling rods with different orientations; (f) ratio of stresses of the tangentially moving rod to the normally moving rod.

6.4.4. Mechanism of Asymmetric Speed Enhancements

Yet the question still remains: why does the return stroke saw a larger speed enhancement by fluid memory? In Fig. 6.11 (a) we plot the flagellum contours for the viscoelastic stroke with the distal tip orientation highlighted. We find that the tip orientation is less aligned with the direction of motion during the power stroke than during the return stroke. This is clearly seen when the tip orientation angle with the transversal axis θ in plotted in Fig. 6.11(b), where θ is significantly larger than the power stroke.

Hence, can the higher elastic stress accumulated during the return stroke be attributed to this tip orientation asymmetry? In order to gain insight into the effects of flagellar tip orientation in a viscoelastic fluid on swimming, we simulate a thin cylindrical rod traveling at a constant velocity both tangential and normal to its long axis and measure the elastic stress as a function of fluid elasticity. We use a rod length of 8 μm, and drag it at a constant velocity of 100 μm/s (characteristic lengths and speeds of a free swimming alga) until the elastic stress is equilibrated. To characterize the strength of elasticity, we define a dimensionless Weissenberg number for this problem as $Wi = \lambda U_\infty / L$, where λ is the polymer relaxation time, U_∞ is the velocity of the rod, and L is the length of the rod.

The elastic strain energy density for a rod that is tangential and normal to a viscoelastic flow at $Wi = 7.5$ is shown in Fig. 6.11(c) and (d) respectively. A region of very high elastic stress is found near the trailing tip of the rod moving in the tangential direction, while lower elastic stress is found near the rod moving in the normal direction. Indeed, when we compute the ratio of elastic to viscous stress in Fig. 6.11(e), we find that the elastic stress difference between the two rod orientations separates quickly with increasing Wi (growing elasticity). Moreover, viscous stress and elastic stress have significantly different trends as the Weissenberg number increases, as shown in Fig. 6.11(f). The *viscous* stress ratio (tangential to normal) is always less than one which agrees qualitatively with what we expect from viscous fluid theory. The elastic stress ratio, however, is strikingly different. As Wi increases, this ratio increases and for sufficiently large Wi this ratio exceed unity.

Hence, we now have a possible mechanism for the asymmetric speed boost for the return stroke versus power stroke, observed both in experiment and in simulation. During the return stroke, the flagellum is more tangentially aligned with the flow and hence generates much larger elastic stresses, which strongly affect the swimming speed via the coasting effect by fluid memory. Although such stresses are not instantaneously equilibrated, the difference in orientation of the tips of the flagella on power and return strokes contributes substantially to the higher elastic stress observed during the return stroke.

6.5. Summary

In this work, we focus on the swimming of green algae *C. reinhardtii* in viscoelastic fluids, yet the feedback we observe between fluid elasticity and such swimming strokes can be a more general principle. Our experimental results show that fluid elasticity enhanced the beating frequency and the wave speed characterizing the cyclical bending. Despite these enhancements, the net swimming speed of the alga is hindered for fluids that are sufficiently elastic and the flagellar stroke pattern is observed to be modified by fluid elasticity. The details of this investigation are published in [186].

Simulations using experimental data attempt to isolate the effect of elastic stresses and provide a possible explanation for the changes in stroke pattern based on the energy spend to overcome elastic stresses. We identified an elastic memory effect by measuring the coasting speed driven by elastic stresses. A possible mechanism of the asymmetric speed enhancement between the power and recovery strokes is proposed. The origin of the complex swimming speed behavior lies in the asymmetric drag experienced by thin rods with different orientation to the flow in viscoelastic fluids. The drag forces contrast strongly with that expected from viscous fluid theory. Furthermore, we show that fundamental principles of swimming in viscoelastic fluids are not captured by viscous fluid theory: larger elastic stress accumulates around flagella moving tangent to the swimming direction, rather than normal. The details of this investigation are published in [187].

CHAPTER 7 : Concluding Remarks

7.1. Summary

Understanding how complex fluids flow and the consequence of non-linear rheology on microscale swimmers has broad significance in technology and human health. From plastic melts extruded though pipes to mucociliary clearance in airways, the complex rheological behaviors, in particular viscoelasticity, can give rise to flow anomalies and intriguing transport dynamics not found in simple Newtonian fluids.

In this thesis, we have investigated the flow instability and micro-swimmer motility in viscoelastic fluids. We examined two broad questions regarding complex fluids: namely how does viscoelastic fluid flow and how to operate in such fluid. These two questions are examined using both physical systems such as micro-channel and biological systems with active micro-swimmers.

In the first part, I studied the flow anomaly of viscoelastic fluids in three flow geometries that reveal three distinct aspects of elastic instability, including (i) the turbulent characteristics and mechanism of the subcritical transition in parallel channel flow, (ii) the characteristics and mechanism of disturbance propagation upstream in elastic instability, and (iii) three-dimensional symmetry breaking in the cross-slot flow.

In **Chapter 3**, we have investigated the flow of viscoelastic fluid in a straight channel flow. The flow is perturbed by an array of cylinders far upstream the parallel shear region. First, using high speed velocimetry, we have found evidence for turbulent-like flow behavior in a parallel shear geometry of a viscoelastic fluid at low Re, namely the presence of irregular flow structures activated at many times scales and a decay law in the velocity power spectra. Further, these features, including power spectra scaling, intermittency statistics, and flow space-time structures are distinct from with those near the curved cylinders in the same system. These results suggest the emergence of a new type of elastic turbulent state in parallel shear flows. Second, we establish the law of resistance and the coherent structures organizing the elastic turbulence in channel flows. We find two regimes: (i) a transitional regime ($5 \lesssim Wi \lesssim 9$) in which the (viscous) friction factor $f_\eta \sim Wi^{1/3}$, and (ii) a turbulent-like regime ($Wi \lesssim 9$) in which a sudden reduction of f_η is observed followed by a weaker dependence on flow rate that leads to $f_\eta \sim Wi^{1/10}$. This behavior is analogous to Newtonian pipe flows in which a sudden increase in drag is followed by a weaker dependence on Re. Dye injections and particle tracking data show the presence of weak flow structures far downstream in the parallel shear region ($200W$). In particular, we find small but finite particle lateral (spanwise) movement and modulations not found in the Newtonian case. These particle trajectories have enough curvature and speed to generate hoop stresses that can sustain flow instabilities. Our results provide strong evidence for the "instability upon an instability" mechanism proposed for the finite amplitude transition of viscoelastic fluids in parallel flows [15, 16] and provide new insights into the flow of polymeric solutions in channels and pipes.

In **Chapter 4**, we have shown that the elastic instability due to the cylinder can propagate upstream. In particular, we report three main discoveries of the elastic instability upstream of a single cylinder in confined channel flow. First, we report the onset of upstream instability in the form of corner vortices in front of the cylinder, whose size grows with increasing flow rate. Second, beyond a critical flow rate, the vortex becomes unsteady and switches between two bi-stable configurations that lead to symmetry breaking perpendicular to the cylinder axis. The flow is highly 3-dimensional in nature. Lastly, we show that the disturbance of the elastic instability propagates far upstream in the form of an elastic wave, yet remains relatively isolated from the flow in the cylinder wake. The elastic wave speed is found to increases with Weissenberg number. Our results suggest that the downstream flow of a viscoelastic fluid may play a huge role far upstream in the long pipes in industries like oil extraction where fluid containing polymers is flown through geometries with obstruction.

In **Chapter 5**, we have investigated the flow of viscoelastic fluid in cross-slot geometry.

Using novel holographic particle tracking, we showed evidence for three-dimensional structures in the classic cross-slot flow instability of a viscoelastic fluid. We identified a tertiary flow instability and a "buckling" instability of the stagnation region in the direction perpendicular to the plane of extension. The onset of the tertiary structures, however, does not seem to coincide with the symmetry breaking in the extensional plane, but rather with the initiation of the flow unsteadiness. Further, the disturbances generated by the cross slot flow instability propagate far upstream. The inlet stream pressure signals alternate between periods of correlation and anti-correlation. These results provide insight into the mechanism of the elastic instability in strongly elongational flows, which are commonly found in industry and technology.

In **Part II** of the thesis, I have studied the motility and transport of active swimmers in viscoelastic fluids that is relevant to biological systems and human health. The system under study is the swimming of green algae in a viscoelastic fluid film.

In **Chapter 6**, we have studied the swimming of bi-flagellated algae *C. reinhardtii* in viscoelastic fluids. Our experimental results show that fluid elasticity enhanced the beating frequency and the wave speed characterizing the cyclical bending. Despite these enhancements, the net swimming speed of the alga is hindered for fluids that are sufficiently elastic and the flagellar stroke pattern is observed to be modified by fluid elasticity. Simulations using experimental data attempt to isolate the effect of elastic stresses and provide a possible explanation for the changes in stroke pattern based on the energy spend to overcome elastic stresses. We identified an elastic memory effect by measuring the coasting speed driven by elastic stresses. A possible mechanism of the asymmetric speed enhancement between the power and recovery strokes is proposed. The origin of the complex swimming speed behavior lies in the asymmetric drag experienced by thin rods with different orientations to the flow in viscoelastic fluids. Furthermore, we show the fundamental principles of swimming in viscoelastic fluids are not captured by traditional viscous fluid theory: larger elastic stress accumulates around flagella moving tangent to the swimming direction, rather than normal. Although we focused on the swimming of bi-flagellated algae *C. reinhardtii* in polymeric solution, the feedback we observe between fluid elasticity and the flagellar strokes can be a more general principle.

7.2. Future Perspectives

In this section we briefly discuss two future projects that continue our investigation of the flow behavior and instabilities in viscoelastic fluids. We propose two research directions in the physical system and the biological system.

7.2.1. Drag on a Sphere in the Elastic Turbulence Regime

The drag on geometries as simple as the sphere in viscoelastic fluid is not fully understood, despite considerable efforts. Experimental measurements of drag coefficient of sphere in Boger fluids are often at odds even on qualitative questions such as whether elasticity increases or decreases drag [66]. Reports of drag coefficients range from monotonic decreasing with Weissenberg number Wi [188], monotonic increasing [189], and trends in-between [190]. Additionally, just like the laminar to turbulent transition of the Newtonian flow around a sphere at high Reynolds number, does there exist a similar transition to the so-called elastic turbulent state? Our previous experiments reported highly irregular flow structures in the flow of viscoelastic fluids around an array of cylinders, see Fig. 3.4(b,c). How would these irregular flow structures, typically observed in elastic turbulence, affect the drag on blunt objects like a sphere or cylinder? A new approach that measures the coupling between irregular flow kinematics and the force dynamics will provide insights.

Using custom viscoelastic “wind tunnel”, load cells, and holographic particle velocimetry, we measure the drag coefficient on blunt objects such as spheres, ellipsoids, and cylinders in both the elastic turbulent regime and the elasto-inertial turbulent regime. Using a glass tube as the test section, we measure the drag force, dye mixing, and flow field associated with blunt objects in the two turbulent regimes. This is achieved using two separate fluids, namely a Boger type polyacrylamide polymer solution in viscous solvent and a dilute polymer solution with water-like viscosity. The forces experienced by the object can be measured using load cells fixed far upstream of the test section. The flow is pressure-driven and the volume flow rate is measured via weight balance. By varying the flow rate and fluid elasticity, we determine the drag coefficient scaling versus Weissenberg number in the elastic regime and versus the Reynolds number in the drag reduction regime. In addition, the transition via elastic instabilities will be quantified using holographic particle tracking. Various confinement levels (glass tube to specimen diameter ratio) will be used. The experimental study will provide additional insights on classical problems like turbulence modification by polymers and purely elastic turbulence.

7.2.2. Collective Swimming of Algae in Viscoelastic Fluids

The effect of fluid viscoelasticity on the collective dynamics of active swimming has been rarely studied despite its ubiquity in biological systems. Using a thin fluid-film device, we seek to understand the dynamics of densely spaced cilia in complex fluids. In particular, we will measure the collective ciliary beating dynamics (frequency, amplitude, waveform) of densely packed algae C. reinhardtii and the induced transport of passive particles to gain insight into mucociliary clearance. The collective ciliary dynamics in complex viscoelastic fluids, while key to biological processes like mucociliary clearance, has not been previously investigated. The proposed experimental setup consists of a thin film of viscoelastic fluid, in which a dense population of algal cells is immersed and brought close to each other via phototaxis, the biased swimming towards light [191].

We expect several phenomena that can be used to induce flow and transport, namely the emergence of patterns of aggregation (circles and bi-layers), enhanced beating synchronization, and a ciliary waveform different from that of a lone cilium or simple viscous fluids. This is because (i) mechanical stress can develop on the cilia due to the “memory of the viscoelastic fluid as well as the proximity with their neighboring cilia, and (ii) cilia are capable of mechanosensation, namely the sensing of mechanical stress and fluid flow. In order to gain insight into the associated transport such as that in mucus clearance, we conduct flow velocimetry using in-house tracking methods. The experimental results will shed light on many biological process produced by collective cilia behavior and directly facilitate the control of material transport and mucociliary clearance.

BIBLIOGRAPHY

[1] G.H. McKinley. A hitchhikers guide to complex fluids. *Rheol. Bull.*, 84:14, 2015.

[2] T. M. Squires and S. R. Quake. Microfluidics: Fluid physics at the nanoliter scale. *Rev. Mod. Phys*, 77(3):977, 2005.

[3] A. D. Stroock *et al.* Chaotic mixer for microchannels. *Science*, 295(5555):647–651, 2002.

[4] G. A. Cooksey, C. G. Sip, and A. Folch. A multi-purpose microfluidic perfusion system with combinatorial choice of inputs, mixtures, gradient patterns, and flow rates. *Lab Chip*, 9(3):417–426, 2009.

[5] C. W. Macosko. *Rheology, principles, measurements and applications.* Wiley press New York, 1994.

[6] O. Reynolds. An experimental investigation of the circumstances which determine whether the motion of water shall be direct or sinuous, and of the law of resistance in parallel channels. *Philos. Trans. R. Soc. Lond.*, 35(224-226):84–99, 1883.

[7] B. Hof *et al.* Experimental observation of nonlinear traveling waves in turbulent pipe flow. *Science*, 305(5690):1594–1598, 2004.

[8] F. Waleffe. On a self-sustaining process in shear flows. *Phys. Fluids*, 9(4):883–900, 1997.

[9] B. Hof *et al.* Turbulence regeneration in pipe flow at moderate reynolds numbers. *Phys. Rev. Lett.*, 95(21):214502, 2005.

[10] M. Guala, S.E. Hommema, and R.J. Adrian. Large-scale and very-large-scale motions in turbulent pipe flow. *J. Fluid Mech.*, 554:521–542, 2006.

[11] L. F. Moody. Friction factors for pipe flow. *Trans. Asme*, 66:671–684, 1944.

[12] S. J. Muller, R. G. Larson, and E. S. G. Shaqfeh. A purely elastic transition in taylor-couette flow. *Rheol. Acta.*, 28(6):499–503, 1989.

[13] A. Groisman and V. Steinberg. Elastic turbulence in a polymer solution flow. *Nature*, 405(6782):53–55, 2000.

[14] M. M. Denn. Fifty years of non-newtonian fluid dynamics. *AIChE J.*, 50(10):2335–2345, 2004.

[15] A. N. Morozov and W. van Saarloos. Subcritical finite-amplitude solutions for plane couette flow of viscoelastic fluids. *Phys. Rev. Lett.*, 95:024501, 2005.

[16] A. N. Morozov and W. van Saarloos. An introductory essay on subcritical instabilities and the transition to turbulence in visco-elastic parallel shear flows. *Phys. Rep.*, 447(3-6):112–143, 2007.

[17] L. Pan, A. Morozov, C. Wagner, and P. E. Arratia. Nonlinear elastic instability in channel flows at low reynolds numbers. *Phys. Rev. Lett.*, 110:174502, 2013.

[18] R. E. Goldstein. Green algae as model organisms for biological fluid dynamics. *Annu. Rev. Fluid Mech.*, 47, 2015.

[19] K. Drescher *et al.* Direct measurement of the flow field around swimming microorganisms. *Phys. Rev. Lett.*, 105(16):168101, 2010.

[20] J. Sznitman, X. Shen, R. Sznitman, and P. E Arratia. Propulsive force measurements and flow behavior of undulatory swimmers at low reynolds number. *Physics Fluids*, 22(12):121901, 2010.

[21] D. A. Gagnon, N.C. Keim, and P.E. Arratia. Undulatory swimming in shear-thinning fluids: experiments with caenorhabditis elegans. *J. Fluid Mech.*, 758:R3, 2014.

[22] A. Groisman and V. Steinberg. Efficient mixing at low reynolds numbers using polymer additives. *Nature*, 410(6831):905–908, 2001.

[23] P. Yager *et al.* Microfluidic diagnostic technologies for global public health. *Nature*, 442(7101):412, 2006.

[24] C. D. Chin *et al.* Microfluidics-based diagnostics of infectious diseases in the developing world. *Nature Med.*, 17(8):1015, 2011.

[25] K. T. Kotz *et al.* Clinical microfluidics for neutrophil genomics and proteomics. *Nature Med.*, 16(9):1042, 2010.

[26] M. K. Kim *et al.* Local and global consequences of flow on bacterial quorum sensing. *Nat. Microbiol.*, 1(1):15005, 2016.

[27] J. El-Ali, P. K. Sorger, and K. F. Jensen. Cells on chips. *Nature*, 442(7101):403, 2006.

[28] T. M. Pearce *et al.* Integrated microelectrode array and microfluidics for temperature clamp of sensory neurons in culture. *Lab Chip*, 5(1):97–101, 2005.

[29] A. J. Muinonen-Martin *et al.* An improved chamber for direct visualisation of chemotaxis. *PloS one*, 5(12):e15309, 2010.

[30] T. Ahmed, T. S. Shimizu, and R. Stocker. Microfluidics for bacterial chemotaxis. *Integr. Biol.*, 2(11-12):604–629, 2010.

[31] Macros *et al.* Bacterial rheotaxis. *Proc. Natl. Acad. Sci.*, 109(13):4780–4785, 2012.

[32] K. Drescher *et al.* Biofilm streamers cause catastrophic disruption of flow with consequences for environmental and medical systems. *Proc. Natl. Acad. Sci.*, 110(11):4345–4350, 2013.

[33] R. Stocker R. Rusconi, J.S. Guasto. Bacterial transport suppressed by fluid shear. *Nature Phys.*, 10(3):212, 2014.

[34] D. Huh *et al.* Reconstituting organ-level lung functions on a chip. *Science*, 328(5986):1662–1668, 2010.

[35] M. Tsai *et al.* In vitro modeling of the microvascular occlusion and thrombosis that occur in hematologic diseases using microfluidic technology. *J. Clin. Invest.*, 122(1), 2011.

[36] I. Wagner *et al.* A dynamic multi-organ-chip for long-term cultivation and substance testing proven by 3d human liver and skin tissue co-culture. *Lab Chip*, 13(18):3538–3547, 2013.

[37] B. Sebastian and P. S. Dittrich. Microfluidics to mimic blood flow in health and disease. *Annu. Rev. Fluid Mech.*, 50:483–504, 2018.

[38] C. J. Pipe and G. H. McKinley. Microfluidic rheometry. *Mech. Res. Commun.*, 36(1):110–120, 2009.

[39] K. N. Nordstrom *et al.* Microfluidic rheology of soft colloids above and below jamming. *Phys. Rev. Lett.*, 105(17):175701, 2010.

[40] F. J. Galindo-Rosales *et al.* Microdevices for extensional rheometry of low viscosity elastic liquids: a review. *Microfluidics Nanofluidics*, 14(1-2):1–19, 2013.

[41] T. J. Ober *et al.* Microfluidic extensional rheometry using a hyperbolic contraction geometry. *Rheol. Acta*, 52(6):529–546, 2013.

[42] S. D. Hudson *et al.* A microliter capillary rheometer for characterization of protein solutions. *J. Pharm. Sci.*, 104(2):678–685, 2015.

[43] T. T. Perkins, D. E. Smith, and S. Chu. Single polymer dynamics in an elongational flow. *Science*, 276(5321):2016–2021, 1997.

[44] G. Juarez and P. E. Arratia. Extensional rheology of dna suspensions in microfluidic devices. *Soft Matter*, 7(19):9444–9452, 2011.

[45] L. E. Rodd *et al.* The inertio-elastic planar entry flow of low-viscosity elastic fluids in micro-fabricated geometries. *J.Non-Newtonian Fluid Mech.*, 129(1):1–22, 2005.

[46] L. E. Rodd *et al.* Role of the elasticity number in the entry flow of dilute polymer solutions in micro-fabricated contraction geometries. *J.Non-Newtonian Fluid Mech.*, 143(2-3):170–191, 2007.

[47] P. E. Arratia, C. C. Thomas, J. Diorio, and J. P. Gollub. Elastic instabilities of polymer solutions in cross-channel flow. *Phys. Rev. Lett.*, 96:144502, 2006.

[48] P. C. Sousa, F. T. Pinho, and M. A. Alves. Purely-elastic flow instabilities and elastic turbulence in microfluidic cross-slot devices. *Soft matter*, 2017.

[49] V. Kantsler and R. E Goldstein. Fluctuations, dynamics, and the stretch-coil transition of single actin filaments in extensional flows. *Phys. Rev. Lett.*, 108(3):038103, 2012.

[50] H. Bodiguel *et al.* Flow enhancement due to elastic turbulence in channel flows of shear thinning fluids. *Phys. Rev. Lett.*, 114(2):028302, 2015.

[51] S. De *et al.* Lane change in flows through pillared microchannels. *Phys. Fluids*, 29(11):113102, 2017.

[52] S. De *et al.* Viscoelastic flow past mono-and bidisperse random arrays of cylinders: flow resistance, topology and normal stress distribution. *Soft matter*, 13(48):9138–9146, 2017.

[53] D. Kawale *et al.* Elastic instabilities during the flow of hydrolyzed polyacrylamide solution in porous media: effect of pore-shape and salt. *Soft matter*, 13(4):765–775, 2017.

[54] D. Kawale *et al.* Polymer conformation during flow in porous media. *Soft matter*, 13(46):8745–8755, 2017.

[55] J. Cooper McDonald and George M. Whitesides. Poly(dimethylsiloxane) as a material for fabricating microfluidic devices. *Acc. Chem. Res.*, 35(7):491–499, 2002.

[56] R. J. Adrian. Particle-imaging techniques for experimental fluid mechanics. *Annu. Rev. Fluid Mech.*, 23(1):261–304, 1991.

[57] J. Westerweel, G. E. Elsinga, and R. J. Adrian. Particle image velocimetry for complex and turbulent flows. *Annu. Rev. Fluid Mech.*, 45:409–436, 2013.

[58] S. T. Wereley and C. D. Meinhart. Recent advances in micro-particle image velocimetry. *Annu. Rev. Fluid Mech.*, 42:557–576, 2010.

[59] J. G. Santiago *et al.* A particle image velocimetry system for microfluidics. *Exp. Fluids*, 25(4):316–319, 1998.

[60] J. C. Crocker and D. G. Grier. Methods of digital video microscopy for colloidal studies. *J. Colloid Interface Sci.*, 179(1):298–310, 1996.

[61] B. Qin and P. E. Arratia. Characterizing elastic turbulence in channel flows at low reynolds number. *Phys. Rev. Fluids*, 2(8):083302, 2017.

[62] F. C. Cheong, B. J. Krishnatreya, and D. G. Grier. Strategies for three-dimensional particle tracking with holographic video microscopy. *Opt. Express*, 18(13):13563–13573, 2010.

[63] P. F. Salipante, C. A.E. Little, and S. D. Hudson. Jetting of a shear banding fluid in rectangular ducts. *Phys. Rev. Fluids*, 2(3):033302, 2017.

[64] C. E. Brennen and C. E. Brennen. *Fundamentals of multiphase flow.* Cambridge university press, 2005.

[65] J. G. Oldroyd. On the formulation of rheological equations of state. *Proc. R. Soc. Lond. A*, 200(1063):523–541, 1950.

[66] D. F. James. Boger fluids. *Annu. Rev. Fluid Mech.*, 41:129–142, 2009.

[67] G. Prilutski *et al.* Model viscoelastic liquids. *J. Non-Newtonian Fluid Mech.*, 12(2):233–241, 1983.

[68] B. Thomases and M. Shelley. Emergence of singular structures in oldroyd-b fluids. *Phys. Fluid*, 19(10):103103, 2007.

[69] M. Herrchen and H. C. Öttinger. A detailed comparison of various fene dumbbell models. *J. Non-Newtonian Fluid Mech.*, 68(1):17–42, 1997.

[70] B. Purnode and M.J. Crochet. Polymer solution characterization with the fene-p model. *J. Non-Newtonian Fluid Mech.*, 77(1-2):1–20, 1998.

[71] A. Lindner, J. Vermant, and D. Bonn. How to obtain the elongational viscosity of dilute polymer solutions? *Physica A*, 319:125–133, 2003.

[72] R. B. Bird *et al. Dynamics of Polymeric Liquids, Vol. 2, Kinetic Theory.* Wiley, New York, 1987.

[73] R. G. Larson. *The structure and rheology of complex fluids*, volume 33. Oxford university press New York, 1999.

[74] V. M. Entov and E. J. Hinch. Effect of a spectrum of relaxation times on the capillary thinning of a filament of elastic liquid. *J. Non-Newtonian Fluid Mech.*, 72(1):31–53, 1997.

[75] I. J. Wygnanski and F. H. Champagne. On transition in a pipe. part 1. the origin of puffs and slugs and the flow in a turbulent slug. *J. Fluid Mech.*, 59(2):281–335, 1973.

[76] H. Faisst and B. Eckhardt. Traveling waves in pipe flow. *Phys. Rev. Lett.*, 91:224502, Nov 2003.

[77] H. Faisst and B. Eckhardt. Sensitive dependence on initial conditions in transition to turbulence in pipe flow. *J. Fluid Mech.*, 504:343–352, 2004.

[78] H. Wedin and R.R. Kerswell. Exact coherent structures in pipe flow: traveling wave solutions. *J. Fluid Mech.*, 508:333–371, 6 2004.

[79] F. Waleffe. Exact coherent structures in channel flow. *J. Fluid Mech.*, 435:93–102, 2001.

[80] M. A. Fardin *et al.* Elastic turbulence in shear banding wormlike micelles. *Phys. Rev. Lett.*, 104:178303, Apr 2010.

[81] T. Burghelea, E. Segre, and V. Steinberg. Elastic turbulence in von karman swirling flow between two disks. *Phys. Fluids*, 19, 2007.

[82] Y. Jun and V. Steinberg. Power and pressure fluctuations in elastic turbulence over a wide range of polymer concentrations. *Phys. Rev. Lett.*, 102:124503, Mar 2009.

[83] R. G. Larson, E. S. G. Shaqfeh, and S. J. Muller. A purely elastic instability in taylor-couette flow. *J. Fluid Mech.*, 218:573–600, 9 1990.

[84] A. Groisman and V. Steinberg. Mechanism of elastic instability in couette flow of polymer solutions: Experiment. *Phys. Fluids*, 10(10):2451–2463, 1998.

[85] R. J. Poole, M. A. Alves, and P. J. Oliveira. Purely elastic flow asymmetries. *Phys. Rev. Lett.*, 99:164503, 2007.

[86] K. Arora, R. Sureshkumar, and B. Khomami. Experimental investigation of purely elastic instabilities in periodic flows. *J. Non-Newtonian Fluid Mech.*, 108(1-3):209 – 226, 2002.

[87] M. Grilli, A. Vázquez-Quesada, and M. Ellero. Transition to turbulence and mixing in a viscoelastic fluid flowing inside a channel with a periodic array of cylindrical obstacles. *Phys. Rev. Lett.*, 110:174501, 2013.

[88] D.V. Boger. A highly elastic constant-viscosity fluid. *J. Non-Newtonian Fluid Mech.*, 3(1):87–91, 1977.

[89] A. Groisman and V. Steinberg. Elastic turbulence in curvilinear flows of polymer solutions. *New J. Phys.*, 6(1):29, 2004.

[90] R. G. Larson. Fluid dynamics: Turbulence without inertia. *Nature*, 405(6782):27–28, 2000.

[91] R. G. Larson and J. J. Magda. Coil-stretch transitions in mixed shear and extensional flows of dilute polymer solutions. *Macromolecules*, 22(7):3004–3010, 1989.

[92] P. G. De Gennes. Coil-stretch transition of dilute flexible polymers under ultrahigh velocity gradients. *J. Chem. Phys.*, 60(12):5030–5042, 1974.

[93] D. E. Smith and S. Chu. Response of flexible polymers to a sudden elongational flow. *Science*, 281(5381):1335–1340, 1998.

[94] C. M. Schroeder *et al.* Observation of polymer conformation hysteresis in extensional flow. *Science*, 301(5639):1515–1519, 2003.

[95] D. E. Smith, H. P. Babcock, and S. Chu. Single-polymer dynamics in steady shear flow. *Science*, 283(5408):1724–1727, 1999.

[96] P. Pakdel and G. H. McKinley. Elastic instability and curved streamlines. *Phys. Rev. Lett.*, 77:2459–2462, Sep 1996.

[97] G. H. McKinley, P. Pakdel, and A. Aztekin. Rheological and geometric scaling of purely elastic flow instabilities. *J. Non-Newtonian Fluid Mech.*, 67:19 – 47, 1996.

[98] T. C. Ho and M. M. Denn. Stability of plane poiseuille flow of a highly elastic liquid. *J. Non-Newtonian Fluid Mech.*, 3(2):179 – 195, 1977.

[99] B. Meulenbroek, C. Storm, A.N. Morozov, and Wim van Saarloos. Weakly nonlinear subcritical instability of visco-elastic poiseuille flow. *J. Non-Newtonian Fluid Mech.*, 116:235 – 268, 2004.

[100] B. Meulenbroek *et al.* Intrinsic route to melt fracture in polymer extrusion: A weakly nonlinear subcritical instability of viscoelastic poiseuille flow. *Phys. Rev. Lett.*, 90:024502, 2003.

[101] D. Bonn, F. Ingremeau, Y. Amarouchene, and H. Kellay. Large velocity fluctuations in small-reynolds-number pipe flow of polymer solutions. *Phys. Rev. E*, 84:045301, Oct 2011.

[102] M. R. Jovanovic and S. Kumar. Transient growth without inertia. *Phys. Fluids*, 22(2):023101, 2010.

[103] M. R. Jovanovic and S. Kumar. Nonmodal amplification of stochastic disturbances in strongly elastic channel flows. *J. Non-Newtonian Fluid Mech.*, 166(14-15):755 – 778, 2011.

[104] K. Avila, D. Moxey, A. de Lozar, M. Avila, D. Barkley, and B. Hof. The onset of turbulence in pipe flow. *Science*, 333(6039):192–196, 2011.

[105] E. M. Purcell. Lift at low reynolds number. *Am. J. Phys.*, 45:3–11, 1977.

[106] E. Lauga and T. Powers. The hydrodynamics of swimming microorganisms. *Rep. Prog. Phys.*, 72:096601, 2009.

[107] R. Stocker. Reverse and flick: Hybrid locomotion in bacteria. *Proc. Natl. Acad. Sci.*, 108(7):2635–2636, 2011.

[108] H. C. Berg and D. A. Brown. Chemotaxis in *escherichia coli* analysed by three-dimensional tracking. *Nature*, 239(5374):500–504, 1972.

[109] L. Zhang *et al.* Characterizing the swimming properties of artificial bacterial flagella. *Nano Lett.*, 9(10):3663–3667, 2009.

[110] J. Li, I. Rozen, and J. Wang. Rocket science at the nanoscale. *ACS Nano*, 10(6):5619–5634, 2016.

[111] G. I. Taylor. Analysis of the swimming of microscopic organisms. *Proc. R. Soc. Lond. A*, 209(1099):447–461, 1951.

[112] G. I. Taylor. The action of waving cylindrical tails in propelling microscopic organisms. *Proc. R. Soc. Lond. A*, 211(1105):225–239, 1952.

[113] G. J. Hancock. The self-propulsion of microscopic organisms through liquids. *Proc. R. Soc. Lond. A*, 217(1128):96–121, 1953.

[114] A.E. Patteson, A. Gopinath, M. Goulian, and P.E. Arratia. Running and tumbling with e. coli in polymeric solutions. *Sci. Rep.*, 5:15761, 2015.

[115] S. S. Suarez and A.A. Pacey. Sperm transport in the female reproductive tract. *Hum. Reprod. Update*, 12(1):23–37, 2006.

[116] M. A. Sleigh, J. R. Blake, and N. Liron. The propulsion of mucus by cilia. *Am. Rev. Respir. Dis.*, 137(3):726–741, 1988.

[117] M. R. Knowles and R. C. Boucher. Mucus clearance as a primary innate defense mechanism for mammalian airways. *J Clin. Invest.*, 109(5):571–577, 2002.

[118] C. Montecucco and R. Rappuoli. Living dangerously: how helicobacter pylori survives in the human stomach. *Nat. Rev. Mol. Cell Biol.*, 2(6):457, 2001.

[119] T. Normand and E. Lauga. Flapping motion and force generation in a viscoelastic fluid. *Phys. Rev. E*, 78(6):061907, 2008.

[120] N. C. Keim, M. Garcia, and P. E. Arratia. Fluid elasticity can enable propulsion at low reynolds number. *Phys. Fluids*, 24(8):081703, 2012.

[121] E. Lauga. Propulsion in a viscoelastic fluid. *Phys. Fluids*, 19(8):083104, 2007.

[122] L. Zhu, E. Lauga, and L. Brandt. Self-propulsion in viscoelastic fluids: Pushers vs. pullers. *Phys. Fluids*, 24(5):051902, 2012.

[123] X. N. Shen and P. E. Arratia. Undulatory swimming in viscoelastic fluids. *Phys. Rev. Lett.*, 106(20):208101, 2011.

[124] J. Teran, L. Fauci, and M. Shelley. Fluid elasticity can enable propulsion at low reynolds number. *Phys. Rev. Lett.*, 104:038101, 2010.

[125] B. Thomases and R. D. Guy. Mechanisms of elastic enhancement and hindrance for finite length undulatory swimmers in viscoelastic fluids. *Phys. Rev. Lett.*, 113(9):098102, 2014.

[126] B. Liu, T. R. Powers, and K. S. Breuer. Force-free swimming of a model helical flagellum in viscoelastic fluids. *Proc. Natl. Acad. Sci. U.S.A.*, 108:19516–19520, 2011.

[127] G. H. McKinley, R. C. Armstrong, and R. A. Brown. The wake instability in viscoelastic flow past confined circular cylinders. *Proc. R. Soc. A*, 344(1671):265–304, 1993.

[128] H. R. Rafael, K. Sinha, and M. D. Graham. Margination regimes and drainage transition in confined multicomponent suspensions. *Phys. Rev. Lett.*, 114:188101, 2015.

[129] M. Thiébaud, Z. Shen, J. Harting, and C. Misbah. Prediction of anomalous blood viscosity in confined shear flow. *Phys. Rev. Lett.*, 112:238304, 2014.

[130] M. Levant and V. Steinberg. Complex dynamics of compound vesicles in linear flow. *Phys. Rev. Lett.*, 112:138106, 2014.

[131] S. Gulati, D. Liepmann, and S. J. Muller. Elastic secondary flows of semidilute DNA solutions in abrupt 90 degrees microbends. *Phys. Rev. E*, 78(3):036314, 2008.

[132] J. Zilz, R. J. Poole, M. A. Alves, D. Bartolo, B. Levaché, and A. Lindner. Geometric scaling of a purely elastic flow instability in serpentine channels. *J. Fluid Mech.*, 712:203–218, 2012.

[133] Y. C. Lam, H. Y. Gan, N. T. Nguyen, and H. Lie. Micromixer based on viscoelastic flow instability at low reynolds number. *Biomicrofluidics*, 3(1):014106, 2009.

[134] C. Scholz, F. Wirner, J. R. Gomez-Solano, and C. Bechinger. Enhanced dispersion by elastic turbulence in porous media. *Europhys. Lett.*, 107(5):54003, 2014.

[135] E. S. G. Shaqfeh. Purely elastic instabilities in viscometric flows. *Annu. Rev. Fluid Mech.*, 28(1):129–185, 1996.

[136] E. Pelletier, C. Viebke, J. Meadows, and P.A. Williams. Dilute polyacrylamide solutions under uniaxial extensional flow. *Langmuir*, 19(3):559–565, 2003.

[137] T. Burghelea, E. Segre, and V. Steinberg. Role of elastic stress in statistical and scaling properties of elastic turbulence. *Phys. Rev. Lett.*, 96:214502, May 2006.

[138] Y. Liu and V. Steinberg. Stretching of polymer in a random flow: Effect of a shear rate. *Europhys. Lett.*, 90(4):44005, 2010.

[139] E. Balkovsky, A. Fouxon, and V. Lebedev. Turbulent dynamics of polymer solutions. *Phys. Rev. Lett.*, 84:4765–4768, 2000.

[140] M. Chertkov. Polymer stretching by turbulence. *Phys. Rev. Lett.*, 84:4761–4764, 2000.

[141] S. Gerashchenko and V. Steinberg. Critical slowing down in polymer dynamics near the coil-stretch transition in elongation flow. *Phys. Rev. E*, 78:040801, 2008.

[142] M. A. Alves, F. T. Pinho, and P. J. Oliveira. The flow of viscoelastic fluids past a cylinder: finite-volume high-resolution methods. *J. Non-Newtonian Fluid Mech.*, 97(2-3):207–232, 2001.

[143] B. Thomases, M. Shelley, and J.L. Thiffeault. A stokesian viscoelastic flow: transition to oscillations and mixing. *Physica D*, 240(20):1602–1614, 2011.

[144] R. P. Chhabra, J. Comiti, and I. Machač. Flow of non-newtonian fluids in fixed and fluidised beds. *Chem. Eng. Sci.*, 56(1):1–27, 2001.

[145] A. E. Peksa, A. A. Wolf, and P. L. J. Zitha. Bentheimer sandstone revisited for experimental purposes. *Mar. Pet. Geol.*, 67:701–719, 2015.

[146] S. De, J. van der Schaaf, N.G. Deen, J.A.M. Kuipers, E. Peters, and J.T. Padding. Lane change in flows through pillared microchannels. *Phys. Fluids*, 29(11):113102, 2017.

[147] D. Kawale, G. Bouwman, S. Sachdev, P.L.J. Zitha, M. T. Kreutzer, W. R. Rossen, and P. E. Boukany. Polymer conformation during flow in porous media. *Soft matter*, 13(46):8745–8755, 2017.

[148] S. Kenney, K. Poper, G. Chapagain, and G. F. Christopher. Large deborah number flows around confined microfluidic cylinders. *Rheol. Acta*, 52(5):485–497, 2013.

[149] X. Shi and G. F. Christopher. Growth of viscoelastic instabilities around linear cylinder arrays. *Physics Fluids*, 28(12):124102, 2016.

[150] A. Varshney and V. Steinberg. Elastic wake instabilities in a creeping flow between two obstacles. *Phys. Rev. Fluids*, 2(5):051301, 2017.

[151] S. J. Haward, K. Toda-Peters, and A.Q. Shen. Steady viscoelastic flow around high-aspect-ratio, low-blockage-ratio microfluidic cylinders. *J. Non-Newtonian Fluid Mech.*, 254:23–35, 2018.

[152] A.S. Lubansky, D.V. Boger, C. Servais, A.S. Burbidge, and J. J Cooper-White. An approximate solution to flow through a contraction for high trouton ratio fluids. *J.Non-Newtonian Fluid Mech.*, 144(2-3):87–97, 2007.

[153] S. Gulati, S.J. Muller, and D. Liepmann. Direct measurements of viscoelastic flows of dna in a 2: 1 abrupt planar micro-contraction. *J. Non-Newtonian Fluid Mech.*, 155(1-2):51–66, 2008.

[154] E. Miller and J.J. Cooper-White. The effects of chain conformation in the microfluidic entry flow of polymer–surfactant systems. *J. Non-Newtonian Fluid Mech.*, 160(1):22–30, 2009.

[155] L. E. Rodd, D. Lee, K.H. Ahn, and J. J. Cooper-White. The importance of downstream events in microfluidic viscoelastic entry flows: Consequences of increasing the constriction length. *J. Non-Newtonian Fluid Mech.*, 165(19-20):1189–1203, 2010.

[156] S. Gulati, D. Liepmann, and S.J. Muller. Elastic secondary flows of semidilute dna solutions in abrupt 90 microbends. *Phys. Rev. E*, 78(3):036314, 2008.

[157] S. Gulati, C.S. Dutcher, D. Liepmann, and S. J. Muller. Elastic secondary flows in sharp 90 degree micro-bends: A comparison of peo and dna solutions. *J. Rheol.*, 54(2):375–392, 2010.

[158] M.Y. Hwang, H. Mohammadigoushki, and S.J. Muller. Flow of viscoelastic fluids around a sharp microfluidic bend: Role of wormlike micellar structure. *Phys. Rev. Fluids*, 2(4):043303, 2017.

[159] X. Shi, S. Kenney, G. Chapagain, and G. F. Christopher. Mechanisms of onset for moderate mach number instabilities of viscoelastic flows around confined cylinders. *Rheol. Acta*, 54(9-10):805–815, 2015.

[160] S.C. Omowunmi and X. Yuan. Modelling the three-dimensional flow of a semi-dilute polymer solution in microfluidics on the effect of aspect ratio. *Rheol. Acta*, 49(6):585–595, 2010.

[161] D. V. Boger. Viscoelastic flows through contractions. *Ann. Rev. Fluid Mech.*, 19(1):157–182, 1987.

[162] S. J. Haward. Buckling instabilities in dilute polymer solution elastic strands. *Rheologica acta*, 49(11-12):1219–1225, 2010.

[163] F. A. Cruz *et al.* Influence of channel aspect ratio on the onset of purely-elastic flow instabilities in three-dimensional planar cross-slots. *J. Non-Newtonian Fluid Mech.*, 227:65–79, 2016.

[164] N. Burshtein *et al.* Inertioelastic flow instability at a stagnation point. *Phys. Rev. X*, 7:041039, 2017.

[165] K. E. Machin. Wave propagation along flagella. *J. Exp. Biol.*, 35(4):796–806, 1958.

[166] D. F. Katz, R. N. Mills, and T. R. Pritchett. The movement of human spermatozoa in cervical mucus. *J. Reprod. Fertil.*, 53:259–265, 1978.

[167] H. C. Ho and S. S. Suarez. Hyperactivation of mammalian spermatozoa: function and regulation. *Reproduction*, 122:519–526, 2001.

[168] L. Fauci and R. Dillon. Biofluidmechanics of reproduction. *Annu. Rev. Fluid Mech.*, 38:371, 2006.

[169] A. Wanner *et al.* Mucociliary clearance in the airways. *Am. J. Respir. Crit. Care Med.*, 154(6):1868–1902, 1996.

[170] J. P. Celli *et al.* *Heliobacter pylori* moves through mucus by reducing mucin viscoelasticity. *Proc. Natl. Acad. Sci. USA*, 106:14321–14326, 2009.

[171] M. Alexander. *Introduction to soil microbiology.* R.E. Krieger, Malabar, FL, 1991.

[172] E.P. Lillehoj and K.C. Kim. Airway mucus: its components and function. *Arch. Pharm. Res.*, 25(6):770–780, 2002.

[173] S. K. Lai, Y. Y. Wang, D. Wirtz, and J. Hanes. Micro-and macrorheology of mucus. *Adv. Drug Deliver. Rev.*, 61(2):86–100, 2009.

[174] S. S. Suarez and X. B. Dai. Hyperactivation enhances mouse sperm capacity for penetrating viscoelastic media. *Biol. Reprod.*, 46(4):686–691, 1992.

[175] D. S. Guzick *et al.* Sperm morphology, motility, and concentration in fertile and infertile men. *N. Engl. J. Med.*, 345:1388–1393, 2001.

[176] G. Juarez, K. Lu, J. Sznitman, and P. E. Arratia. Motility of small nematodes in wet granular media. *Europhys. Lett.*, 92:44002, 2010.

[177] D. A. Gagnon, X. N. Shen, and P. E. Arratia. Undulatory swimming in fluids with polymer networks. *Europhys. Lett.*, 104:14004, 2013.

[178] H. C. Fu, C. W. Wolgemuth, and T. R. Powers. Swimming speeds of filaments in nonlinearly viscoelastic fluids. *Phys. Fluids*, 21(3):033102, 2009.

[179] H. C. Fu, T. R. Powers, and C. W. Wolgemuth. Theory of swimming filaments in viscoelastic media. *Phys. Rev. Lett.*, 99(25):258101–1–4, 2007.

[180] O. S. Pak, L. Zhu, L. Brandt, and E. Lauga. Micropropulsion and microrheology in complex fluids via symmetry breaking. *Phys. Fluids*, 24(10):103102, 2012.

[181] E. H. Harris. *The* Chlamydomonas *Sourcebook*. Academic Press, Oxford, 1999.

[182] J. S. Guasto, K. A. Johnson, and J. P. Gollub. Oscillatory flows induced by microorganisms swimming in two dimensions. *Phys. Rev. Lett.*, 105(16):168102, 2010.

[183] S. Camalet and F. Julicher. Generic aspects of axonemal beating. *New J. Phys.*, 2:24.1–24.23, 2000.

[184] S. Rafai, L. Jibuti, and P. Peyla. Effective viscosity of microswimmer suspensions. *Phys. Rev. Lett.*, 104(4):098102, 2010.

[185] J. Feng and L. G. Leal. Transient extension and relaxation of a dilute polymer solution in a four-roll mill. *J. Non-Newtonian Fluid Mech.*, 90(1):117–123, 2000.

[186] B. Qin, A. Gopinath, J. Yang, J. P. Gollub, and P. E. Arratia. Flagellar kinematics and swimming of algal cells in viscoelastic fluids. *Sci. Rep.*, 5:9190, 2015.

[187] C. Li, B. Qin, A. Gopinath, P. E. Arratia, B. Thomases, and R. D. Guy. Flagellar swimming in viscoelastic fluids: role of fluid elastic stress revealed by simulations based on experimental data. *J. Royal Soc. Interface*, 14(135):20170289, 2017.

[188] R. P. Chhabra, P. H. T. Uhlherr, and D. V. Boger. The influence of fluid elasticity on the drag coefficient for creeping flow around a sphere. *J. Non-Newtonian Fluid Mech.*, 6(3-4):187–199, 1980.

[189] L. E. Becker, G. H. McKinley, H. K. Rasmussen, and O. Hassager. The unsteady motion of a sphere in a viscoelastic fluid. *J. Rheol.*, 38(2):377–403, 1994.

[190] V. Tirtaatmadja, P. H. T. Uhlherr, and T. Sridhar. Creeping motion of spheres in fluid m1. *J. Non-Newtonian Fluid Mech.*, 35(2-3):327–337, 1990.

[191] G. B. Witman. Chlamydomonas phototaxis. *Trends Cell Biol.*, 3(11):403 – 408, 1993.